University of Groningen

Van Swinderen Institute for Particle Physics and Gravity

The Glueball spectrum in large-N QCD

Master Thesis in Theoretical Physics

Author:
J. Bor BSc.

Supervisor:
Prof. dr. E. Pallante

Second examiner:
Prof. dr. D. Boer

12 December 2019

Abstract

The aim of this work is to employ lattice simulations to study the glueball spectrum in the large-N limit as a fundamental probe of confinement, and to verify theoretical predictions. A pure Yang-Mills lattice implementation was developed in-house, and used for computing the scalar 0^{++} glueball mass in SU(2) as a first step towards our goal. Although we have successfully observed an upper limit to the mass for the 0^{++} glueball in lattice units, we were unable to directly determine its mass. This is due to the signal of the 2-point correlation function being too noisy in the current implementation.

Acknowledgements

First of all, I would like to thank my supervisor prof. dr. Elisabetta Pallante and second examiner prof. dr. Daniël Boer. Thank you Elisabetta for helping me understand some of the complex material used in this work, for correcting my thesis, and for your overall dedication to the project. Thank you Daniël for being my second examiner.

Secondly, I would like to thank Piter Annema BSc. for a pleasant and productive cooperation during his bachelor project. Not only did we cooperate on the Metropolis Monte Carlo part of our simulations, but we also wrote the basis of the lattice implementation together. Moreover, Piter helped develop the database structure of the simulation code, and parallelized the simulation for increased computational performance.

Thirdly, I would like to thank Bradley Spronk for helping me creating many of the schematic illustrations featured in this work.

Finally, I would like to thank Anton Jansen MSc. for correcting language and spelling mistakes in my thesis.

Contents

1 Introduction

In 2012 CERN found a mass of 125 GeV in their accelerators, later confirmed to be the Higgs particle. The Higgs particle is the result of a theoretical mechanism already proposed in 1964, and gives mass to the bosons in the weak sector of the Standard Model of Elementary Particle Physics. The detection of the Higgs particle has been a celebrated event in particle physics, as it is another confirmation of the success of the Standard Model. Nevertheless, the physics community agrees on the fact that the Standard Model is currently not complete, and many questions remain unanswered. Although most unanswered questions concern the unification of Gravity Physics and Quantum Field Theory, one interesting problem that is purely field theory based concerns the observation of glueball particles. If detected, these hypothetical particles could confirm the Standard Model even more.

In this study we attempt to find the glueball spectrum in the large-N limit by means of lattice simulations to verify theoretical predictions. To perform these lattice simulations, an lattice implementation was developed in-house. In this work, the different theoretical aspects required for understanding these simulations are discussed, as well as our findings from these simulations.

In chapter 2, Quantum Chromodynamics on the lattice is discussed, as well as the mechanism for calculating the mass of a particle using the 2-point connected correlation function. From Quantum Chromodynamics, we will solely consider gluons on the lattice which form theoretical glueball states. In chapter 3, we will explain what the large-N limit is, how it affects the original theory, and why it is so interesting for studying glueballs. In chapter 4, we will find an observable on the four-dimensional hypercube lattice, which represents the 0^{++} glueball. In chapter 5, we will explain how to calculate the expectation value of an observable on the lattice by using the Monte Carlo method. The links on the lattice (which represent the gluons) will be represented with complex matrices and updated to make different lattice configurations. Such configurations are used to calculate the expectation value of an observable, such as the 2-point connected correlation function of the 0^{++} glueball, hence we can search for the mass of the corresponding glueball. In chapter 6, our simulation results will be presented. The settings of the lattice and the origin of errors will also be discussed here. We will see that a calculation of the glueball mass from the 0^{++} correlator is difficult, as noise is dominating the signal. Therefore, we will need noise reduction algorithms to obtain a better correlator, and we will explain two such algorithms that we have used: the so-called multihit and multilevel. The new results will be presented thereafter. In chapter 7, we will summarize our findings and discuss what we have found with respect to our aim. Finally, recommendations are presented that should be done with the implementation of the lattice to find the large-N glueball spectrum in the future.

2 Quantum Field Theory on the Lattice

In this chapter we discuss the most important parts of Quantum Field Theory (QFT) on a lattice. To understand what we want to measure, the Feynman path integral formalism will be introduced in section 2.1, as well as the n-point connected Green's functions. We will transform this correlation function from Minkowski to Euclidean space-time, where it becomes a correlation function of a statistical mechanics system weighted by a Boltzmann factor depending on the action. In section 2.2, we discuss Wilson's formulation, which naturally gives us an understanding of Quantum Chromodynamics, which is the underlying theory of this work. As we will see, Wilson's formulation can be discretized relatively easily, and will allow us to find the a pure Yang-Mills action on the lattice in terms of gauge invariant observables (plaquettes). In section 2.3, we will investigate the measure of the correlation function. In section 2.4, we will provide the generalized construction of gauge invariant observables on the Yang-Mills lattice. Thereafter, in section 2.5, we will discuss how we can obtain a mass of a particle using the 2-point connected correlation function. We will conclude, in section 2.6, with how the temperature of a QFT works on a lattice.

2.1 The Feynman path integral formalism

In this section the goal is to understand QFT, and to argue that the propagation and interactions of particles in Minkowski space-time can be written as a statistical correlation function with a Boltzmann weight in Euclidean space-time. To do so, we first have to understand the basis of QFT, which can be understood in two ways: using canonical quantization or through the path integral formalism. We will use the latter because the path integral is the natural way to understand QFT on a lattice. First, in subsection 2.1.1, we will investigate the quantum mechanical path formalism, based on the book [1] of A. Zee. After this, in subsection 2.1.2, we will move on to field theory and find the n-point Green's functions. These functions describe the vacuum expectation values of particles described by fields in Minkowski space-time. In subsection 2.1.3, we will rotate this correlation function to Euclidean space-time.

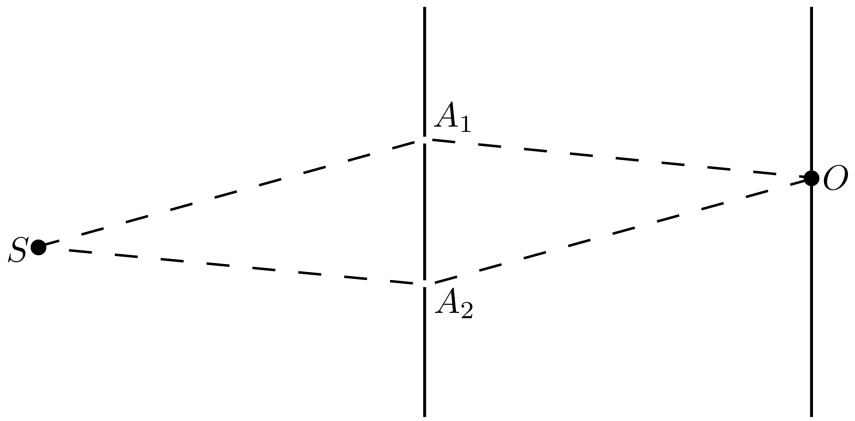

Figure 2.1: The double slit experiment: the probability amplitude for the quantum particle to go from S and to be detected at O is the sum of the probability amplitudes for the particle to travel via A_1 and A_2.

2.1.1 The path integral in Quantum Mechanics

We start by looking at a simple example of a non-relativistic quantum mechanical particle in one spatial dimension. A particle is emitted from source S at time $t = 0$. The particle passes through one of two holes (A_1 or A_2) in a screen, and is detected at time $t = T$ by detector O located at the other side of the screen. This is known as the double-slit experiment (fig 2.1). The probability amplitude for detection $P(S|O)$ is given by one of the fundamental postulates of Quantum Mechanics (QM), the superposition principle. In this experiment $P(S|O)$ is the sum of the amplitude for the particle to propagate from the source S through hole A_1 and then onward to point O, and the amplitude for the particle to pass through A_2 in similar fashion, i.e. $P(S|O) = \sum_i P(S \to A_i \to O)$. We now extend the experiment and add an infinite number of holes in the screen, as well as add an infinite number of such screens between the source S and the detector O. The probability amplitude for detection (for the particle to go from S to O in a time T) now becomes the sum of the probability amplitudes of all particular possible paths between the source and the detector. A number of such paths are shown in fig. 2.2.

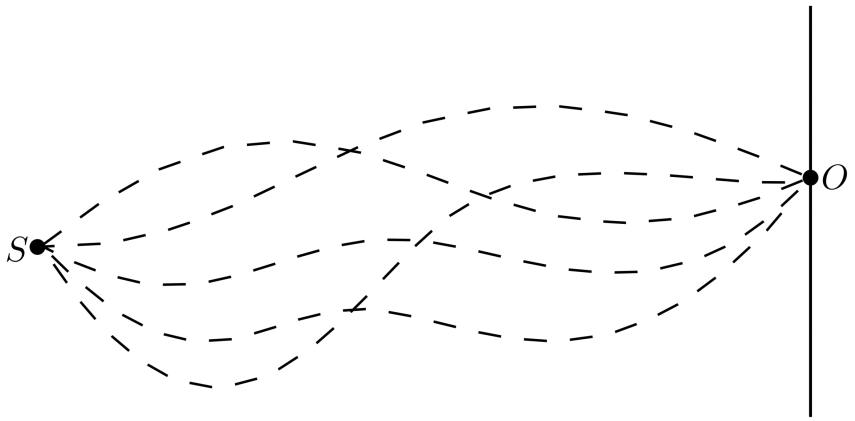

Figure 2.2: The quantum particle can take all paths between S and O.

The probability amplitude for a particle to propagate from spatial coordinate q_I to q_F in time T can be calculated using the time evolution operator e^{-iHT}, in which H is the Hamiltonian. Then, using the 'braket' notation, the amplitude in question reads $\langle q_F|e^{-iHT}|q_I\rangle$. If we divide T into N segments, i.e. $T = \sum_N \delta t$ with $\delta t = T/N$, we write:

$$\langle q_F|e^{-iHT}|q_I\rangle = \langle q_F|e^{-iH\delta t}e^{-iH\delta t}\cdots e^{-iH\delta t}|q_I\rangle \tag{2.1}$$

The states are normalized by $\langle q'|q\rangle = \delta(q' - q)$, where δ is the Dirac delta function defined by $\delta(q) = \int (dp/2\pi)e^{ipq}$ (i.e. the Fourier transform of 1, where p denotes the momentum of the state q) and $\int dq\delta(q) = 1$. Using the fact that $|q\rangle$ forms a complete set of coordinate eigenstates, i.e. $\int dq|q\rangle\langle q| = 1$, we see that the normalization is correct by multiplying on the left by $\langle q''|$ and on the right by $|q'\rangle$, resulting in $\int dq\delta(q'' - q)\delta(q - q') = \delta(q'' - q') = \langle q''|q'\rangle$. The complete set of eigenstates, also known as the completeness relation, we use to write eq. (2.1) as:

$$\langle q_F|e^{-iHT}|q_I\rangle = \prod_{j=1}^{N-1}\int dq_j\langle q_N|e^{-iH\delta t}|q_{N-1}\rangle\langle q_{N-1}|e^{-iH\delta t}|q_{N-2}\rangle\cdots\langle q_1|e^{-iH\delta t}|q_0\rangle \tag{2.2}$$

with $q_0 = q_I$ and $q_N = q_F$. We now focus on a simple factor $\langle q_{j+1}|e^{-iH\delta t}|q_j\rangle$ and consider the Hamiltonian for a nonrelativistic particle in a potential $V(q)$ to be $H = p^2/2m + V(q)$, the sum of kinetic and potential energy. Note that we are working in the Heisenberg picture, i.e. the operators p, q, and H incorporate a dependency on time, and the state vectors (such as $|q\rangle$) are time-independent. From QM we know that $\langle q|p\rangle = e^{ipq}$, which says that the momentum eigenstate is a plane wave in coordinate representation. Remember that in QM $\langle q|p\rangle^\dagger = \langle p|q\rangle$. The normalization in momentum space is such that $\int(dp/2\pi)|p\rangle\langle p| = 1$. Again, to see that this is correct, multiply on the left by $\langle q'|$ and on the right by $|q\rangle$, obtaining $\int(dp/2\pi)e^{ip(q'-q)} = \delta(q'-q)$. Inserting a complete set of momentum eigenstates, we write:

$$\begin{aligned}\langle q_{j+1}|e^{-i\delta t(p^2/2m+V(q))}|q_j\rangle &= \int \frac{dp}{2\pi} e^{-i\delta t(p^2/2m+V(q_j))}\langle q_{j+1}|p\rangle\langle p|q_j\rangle \\ &= \int \frac{dp}{2\pi} e^{-i\delta t(p^2/2m)}\ e^{ip(q_{j+1}-q_j)}\ e^{-i\delta t V(q_j)} \end{aligned} \tag{2.3}$$

The latter is a Gaussian integral, which can be easily evaluated:

$$\begin{aligned}\langle q_{j+1}|e^{-i\delta t(p^2/2m+V(q))}|q_j\rangle &= \left(\frac{-im}{2\pi\delta t}\right)^{\frac{1}{2}} e^{[im(q_{j+1}-q_j)^2]/2\delta t}\ e^{-i\delta t V(q_j)} \\ &= \left(\frac{-im}{2\pi\delta t}\right)^{\frac{1}{2}} \exp\left(i\delta t\left\{\frac{m}{2}\left[\frac{q_{j+1}-q_j}{\delta t}\right]^2 - V(q_j)\right\}\right) \end{aligned} \tag{2.4}$$

Substituting this back into eq. (2.2) we obtain:

$$\langle q_F|e^{-iHT}|q_I\rangle = \left(\frac{-im}{2\pi\delta t}\right)^{\frac{N}{2}} \left(\prod_{j=1}^{N-1}\int dq_j\right) \exp\left(i\delta t\sum_{j=0}^{N-1}\left\{\frac{m}{2}\left[\frac{q_{j+1}-q_j}{\delta t}\right]^2 - V(q_j)\right\}\right) \tag{2.5}$$

We now take the continuum limit by letting $N \to \infty$ and $\delta t \to 0$, which results in replacing $\delta t\sum_{j=0}^{N-1}$ with $\int_0^T dt$ and $[(q_{j+1}-q_j)/\delta t]^2$ with $\dot{q}^2$. We define the integral over all paths within the boundaries to be the measure

$$\int_{b.c.} Dq(t) \equiv \lim_{N\to\infty}\left(\frac{-im}{2\pi\delta t}\right)^{\frac{N}{2}}\left(\prod_{j=1}^{N-1}\int dq_j\right) \tag{2.6}$$

so that the path integral representation becomes

$$\langle q_F|e^{-iHT}|q_I\rangle = \int_{b.c.} Dq(t)\ e^{i\int_0^T[(m/2)\dot{q}^2 - V(q)]dt} = \int_{b.c.} Dq(t)\ e^{i\int_0^T L(q,\dot{q},t)dt} = \int_{b.c.} Dq(t)\ e^{iS} \tag{2.7}$$

where L denotes the classical Lagrangian for the nonrelativistic particle (the Legendre transform of $H(p,q)$) which integrated gives the classical action S.

Eq. 2.7 is interpreted as follows: if we want to evaluate a quantum transition amplitude, we have to sum over all possible classical paths from q_I to q_F, each weighted with the exponential of i times the corresponding classical action. This expression is called the functional integral. Although this result is quite elegant, it is difficult to give a satisfactory mathematical meaning to this integral as the integrand is complex and strongly oscillating.

2.1.2 The n-point Green's functions in Quantum Field Theory

The path integral of QM in subsection 2.1.1 can be generalized to QFT by formal manipulations of the functional integral. In this section, we will translate the functional integral to the field variant and find the Green's functions in Minkowski space-time. These well-known Green's functions provide all the physical information of a QFT and are used to calculate propagation and interaction amplitudes of particles, such as scattering or decay. This section is based on a section of M.E. Peskin & D.V. Schroeder's book [2].

First, we introduce the path integral formalism for a real scalar field $\phi(x)$, where $x = (t, \vec{x})$ labels the coordinates in Minkowski space-time. The Green's functions, or n-point correlation function, is the vacuum expectation value of a time ordered product of n fields:

$$G(\phi(x_n), \cdots, \phi(x_1)) = \langle 0|\phi(x_n), \cdots, \phi(x_1)|0\rangle \qquad (t_n > \cdots > t_1) \tag{2.8}$$

The time evolution of each field is now given, using the Hamiltonian, by

$$\phi_H(t, \vec{x}) = e^{iHt}\phi(t = 0, \vec{x})e^{-iHt} \tag{2.9}$$

where on the left hand side of eq. (2.9) the field is promoted to a Heisenberg picture operator $\phi_H(x)$, to distinguish from ordinary numbers. As already seen in the previous section, the path integral formalism shows that it is much more convenient to work with a Lagrangian formalism instead of a Hamiltonian one. Moreover, every symmetry that the Lagrangian may have is explicitly preserved by the functional integral. The importance of this we will see later on. In field theory, we write the action as $S = \int d^4x\mathcal{L}$, where $\mathcal{L}$ is the Lagrangian density. Now, since the functional integral, eq. (2.7), holds for any quantum system, it should also hold for a QFT. In QFT, the variables $q_j(t)$ become fields $\phi(x)$ and the measure over the paths becomes a measure over the field configurations in the space, i.e. $\Pi_{t,\vec{x}} d\phi(t, \vec{x}) \equiv D\phi$. Thus, the functional integral becomes

$$\langle \phi_F(x)|e^{-iHT}|\phi_I(x)\rangle = \int_{b.c} D\phi \, \exp\left[i \int_0^T dt \int d^3x\mathcal{L}\right] \tag{2.10}$$

where the functions $\phi(x)$ over which we integrate are constrained to the specific configurations at $t = 0$ and at $t = T$.

However, a Green's function is a vacuum expectation value, not a transition amplitude. To find the functional expression for a Green's function, we start from the following integration for the 2-point correlation function

$$\int D\phi(x) \; \phi(x_1)\phi(x_2) \, \exp\left[i \int_{-T}^T dt \int d^3x\mathcal{L}\right] \tag{2.11}$$

where the boundary conditions on the path integral are $\phi(-T, \vec{x}) = \phi_I(x)$ and $\phi(T, \vec{x}) = \phi_F(x)$. First, we break up the functional integral, eq. (2.11), where the times x_1^0 and x_2^0 automatically fall in order ($x_1^0 < x_2^0$), as follows:

$$\int D\phi(x_1) \; \int D\phi(x_2) \; \phi(x_1)\phi(x_2) \; \langle \phi_F|e^{-iH(T-x_2^0)}|\phi_2\rangle\langle\phi_2|e^{-iH(x_2^0-x_1^0)}|\phi_1\rangle\langle\phi_1|e^{-iH(x_1^0-T)}|\phi_I\rangle \tag{2.12}$$

Now, by introducing completeness relations as before, $\int D\phi \, |\phi\rangle\langle\phi| = 1$, and using n fields instead of 2, we relate eq. (2.11) to a field transition amplitude of a time ordered product of fields

$$\langle \phi_F(x)|e^{-iHT}\mathcal{T}\{\phi_H(x_1), \cdots, \phi_H(x_n)\}e^{-iHT}|\phi_I(x)\rangle \tag{2.13}$$

where $\mathcal{T}$ denotes the time ordering operator. Comparing eq. (2.13) with eq. (2.8), we observe that eq. (2.13) is almost equal to the n-point correlation function. To make it equal, we first take the limit $T \to \infty(1 - i\epsilon)$, to project out the vacuum state $|0\rangle$ from $|\phi_I\rangle$ and $|\phi_F\rangle$, assuming that these states have some overlap with $|0\rangle$. This can be shown as follows. Decompose $|\phi_I\rangle$ into eigenstates $|n\rangle$ of H:

$$e^{-iHT}|\phi_I\rangle = \sum_n e^{-iE_nT}|n\rangle\langle n|\phi_I\rangle \tag{2.14}$$

Then, isolate the contribution of $|0\rangle$ from the sum

$$e^{-iHT}|\phi_I\rangle = e^{-iE_0T}|0\rangle\langle 0|\phi_I\rangle + \sum_{n\neq 0} e^{-iE_nT}|n\rangle\langle n|\phi_I\rangle \tag{2.15}$$

where E_0 is the vacuum energy and we are assuming $\langle 0|\phi_I\rangle > 0$. Since $E_n > E_0$, we get rid of all the $n \neq 0$ terms in the series by sending $T \to \infty$ in a slightly imaginary direction, taking ϵ very small. Then the exponential factor e^{-iE_0T} vanishes most slowly. So, we have:

$$\lim_{T\to\infty(1-i\epsilon)} e^{-iHT}|\phi_I\rangle = \langle 0|\phi_I\rangle e^{-iE_0\cdot\infty(1-i\epsilon)}|0\rangle \tag{2.16}$$

Both the overlap $\langle 0|\phi_I\rangle$, the overlap $\langle\phi_F|0\rangle$, and the awkward phase factors $e^{-iE_0\cdot\infty(1-i\epsilon)}$, cancel if we divide eq. (2.13) by the same expression without the time ordered product of n fields. Hence, the disconnected graphs of the fields are also subtracted, i.e. the Green's functions describe only connected fields (which propagate and/or interact) created from the vacuum and annihilated in the vacuum (at large T). So, we have obtained the n-point Green's functions from the path integral formulation (the right hand side):

$$\langle 0|\mathcal{T}\{\phi_H(x_1),\cdots,\phi_H(x_n)\}|0\rangle = \lim_{T\to\infty(1-i\epsilon)} \frac{\int D\phi\ \phi(x_1)\phi(x_2)\cdots\phi(x_n)\exp\left[i\int_{-T}^{T}dt\int d^3x\mathcal{L}\right]}{\int D\phi\exp\left[i\int_{-T}^{T}dt\int d^3x\mathcal{L}\right]} \tag{2.17}$$

2.1.3 Euclidean Field Theory

In the previous subsection we found the Green's functions in Minkowski space-time. If we now take time to be an imaginary number, the exponential factor is no longer an oscillatory factor in the Green's functions. This procedure is called a Wick rotation, because the time coordinate is rotated 90 degrees in the complex plane and goes from the real to the imaginary axis. In other words, we do a substitution $t = -i\tau$, with $\tau \in \mathbb{R}$. It changes the Minkowski metric ($ds^2 = -dt^2 + dx^2 + dy^2 + dz^2$) to a Euclidean metric ($ds^2 = d\tau^2 + dx^2 + dy^2 + dz^2$). By preforming a Wick rotation the $T \to \infty(1 - i\epsilon)$ limit becomes a limit on the imaginary axis alone, hence the boundaries of the integral are also imaginary, and $S \to iS_E$. The Euclidean action is obtained from the action in Minkowski space-time by using the derivative $d\tau/dt = i$ in the argument to write it in terms of τ. The integration measure also changes, but, as before, we do not write this awkward term explicitly. We obtain

$$G_E(\phi(x_1),\cdots,\phi(x_n)) = \lim_{\tau\to\infty} \frac{\int D\phi\ \phi_E(x_1)\phi_E(x_2)\cdots\phi_E(x_n)\exp\left[-\int_{-\tau}^{\tau}d\tau\int d^3x_E\mathcal{L}_E\right]}{\int D\phi\exp\left[-\int_{-\tau}^{\tau}d\tau\int d^3x_E\mathcal{L}_E\right]} \tag{2.18}$$

where the subscript E is to remind us of the fact that we are working in Euclidean space-time. The exponential weight in the integral is now e^{-S_E} and, if the Euclidean action S_E is a real-valued function of the fields and bounded from below, this can be interpreted as a Boltzmann factor of a statistical mechanics system. Moreover, the form of eq. (2.18) resembles a statistical average, where the denominator is the partition function of the system:

$$Z = \int D\phi \; e^{-S_E[\phi]} \tag{2.19}$$

Now, considering any operator in a QFT, instead of just a scalar field, we write the Green's functions or n-point correlation function for a set of operators in Euclidean space-time as:

$$\langle \mathcal{O}_1 \cdots \mathcal{O}_n \rangle_E = \frac{1}{Z} \int D[\mathcal{O}] \; \mathcal{O}_1 \cdots \mathcal{O}_n \; e^{-S_E[\mathcal{O}]} \tag{2.20}$$

Note that, strictly speaking, only the left hand side of eq. (2.20) contains operators $\mathcal{O}$. Therefore, to distinguish between real operators and the O's on the right hand side, the latter are called composite operators. On the lattice the composite operators naturally translate to observables, and we will measure vacuum expectation values of these observables using statistical averages.

2.2 Wilson's formulation of Field Theory

K. Wilson found [3] a geometric way to think about gauge theories. A gauge theory is a theory that is invariant under local transformations of a certain continuous symmetry group, i.e. a Lie group. In subsection 2.2.1, we will use Wilson's formulation to look at the Abelian U(1) group to understand a gauge symmetry. Thereafter, in subsection 2.2.2, we will go to the SU(N) group and discuss the locally SU(N) invariant Lagrangian. Using perturbation theory, the n-point correlation function can be evaluated analytically to obtain the Feynman rules. The Feynman rules can in turn be used to calculate the amplitudes of processes. If $N = 3$, we obtain the famous Quantum Chromodynamics (QCD) theory concerning quarks and gluons. Quarks are fermions, matter particles with half-integer spin. Gluons are bosons, force carrier particles with integer spin. This theory is also known as the strong nuclear force of the Standard Model. However, in subsection 2.3.3, we will apply Wilson's formulation on a lattice, which can be used to perform non-perturbative computations. We will find a pure gluonic, locally SU(N) invariant, action in favour of a lattice computation. These sections are based on M.D. Schwartz's book [4].

2.2.1 The Abelian case

As before, consider a scalar field $\phi(x)$. The global phase of this field is just a convention, so a theory of such a field should be invariant under redefinitions $\phi(x) \to e^{i\alpha}\phi(x)$. This is an Abelian U(1) transformation, meaning it has a commuting generator (the unitary Lie group U(N) with $N = 1$ number of degrees of freedom has the identity element in the exponent of the phase present as a generator). This phase can be seen as a rotation along a circle in the complex plane. Now, suppose we want to examine the field at two points x^μ and y^μ, where μ runs from 1 to 4 denoting the 4 space-time dimensions, which are very far away from each other. In a gauge theory, the phase of x^μ and y^μ are independent of one another. But how can we tell whether $\phi(x) = \phi(y)$? Because $\phi(y) - \phi(x) \to \phi(y)e^{i\alpha(y)} - \phi(x)e^{i\alpha(x)}$ and even $|\phi(y) - \phi(x)|$ depend on the choice of local phases. Moreover, it is impossible to compute $\partial_\mu\phi(x)$ since the derivative is the difference between fields at two points, and the difference depends on the phase choices.

This motivates the introduction of a new field $W(x,y)$, the Wilson line: a bi-local field that depends on two fields. This new field must transform as

$$W(x,y) \to e^{i\alpha(x)} W(x,y) e^{-i\alpha(y)} \tag{2.21}$$

such that:

$$\begin{aligned} W(x,y)\phi(y) - \phi(x) &\to e^{i\alpha(x)} W(x,y) e^{-i\alpha(y)} e^{i\alpha(y)}\phi(y) - e^{i\alpha(x)}\phi(x) \\ &= e^{i\alpha(x)}\big[W(x,y)\phi(y) - \phi(x)\big] \end{aligned} \tag{2.22}$$

The point is that the difference transforms as the field $\phi(x)$. Using $W(x,y)\phi(y) - \phi(x)$, taking $y^\mu = x^\mu + \delta x^\mu$, dividing by δx^μ, and letting $\delta x^\mu \to 0$, lets us turn this difference into a derivative

$$D_\mu \phi(x) \equiv \lim_{\delta x^\mu \to 0} \frac{W(x, x+\delta x)\phi(x+\delta x) - \phi(x)}{\delta x^\mu} \tag{2.23}$$

which transforms as:

$$D_\mu \phi(x) \to e^{i\alpha(x)} D_\mu \phi(x) \tag{2.24}$$

$W(x,x) = 1$, so if δx^μ is small we are be able to expand

$$W(x, x+\delta x) = 1 - ie\delta x^\mu A_\mu(x) + \mathcal{O}(\delta x^2) \tag{2.25}$$

where e is an arbitrary number (or the non-renormalized electric charge coupling in Quantum Electrodynamics (QED), which obeys an Abelian U(1) group symmetry) and A_μ is the gauge field (or the photon field of bosonic nature in QED). Then it follows from the transformation of $W(x,y)$, eq. (2.21), that:

$$A_\mu(x) \to A_\mu(x) + \frac{1}{e}\partial_\mu \alpha(x) \tag{2.26}$$

In a reverse argument, putting eq. (2.26) in eq. (2.25):

$$\begin{aligned} W(x, x+\delta x) &\to 1 - ie\delta x^\mu A_\mu(x) - i\delta x^\mu \partial_\mu \alpha(x) + \mathcal{O}(\delta x^2) \\ &= (1 - ie\delta x^\mu A_\mu(x))(1 - i\delta x^\mu \partial_\mu \alpha(x)) + \mathcal{O}(\delta x^2) \\ &= (1 - ie\delta x^\mu A_\mu(x))\left(1 - i\delta x^\mu \left[\lim_{\delta x^\mu \to 0} \frac{\alpha(x+\delta x) - \alpha(x)}{\delta x^\mu}\right]\right) + \mathcal{O}(\delta x^2) \\ &= e^{i\alpha(x)} W(x, x+\delta x) e^{-i\alpha(x+\delta x)} \end{aligned} \tag{2.27}$$

Now, using eq. (2.23) together with eq. (2.25), we find the covariant derivative:

$$\begin{aligned} D_\mu \phi(x) &= \lim_{\delta x^\mu \to 0} \frac{(1 - ie\delta x^\mu A_\mu)(\phi(x) + \delta x^\mu \partial_\mu \phi(x)) - \phi(x)}{\delta x^\mu} \\ &= \lim_{\delta x^\mu \to 0} \frac{-ie\delta x^\mu A_\mu(x)\phi(x) + \delta x^\mu \partial_\mu \phi(x) + \mathcal{O}(\delta x^2)}{\delta x^\mu} \\ &= (\partial_\mu - ieA_\mu)\phi(x) \end{aligned} \tag{2.28}$$

So, the gauge field is naturally introduced as a connection, allowing us to compare field values at different points despite their arbitrary local phase. This is equivalent to the Christoffel symbol in General Relativity, which is another example of a connection: it allows us to compare field values at different points despite their local coordinate system.

It is possible to write a closed-form expression for $W(x, y)$:

$$W_P(x, y) = \exp\left(ie \int_y^x A_\mu(z) dz^\mu \right) \tag{2.29}$$

This integral is along a path P from y^μ to x^μ. More precisely, the path P is a function of $z^\mu(\lambda)$ with $z^\mu(0) = y^\mu$ and $z^\mu(1) = x^\mu$, leading to:

$$W_P(x, y) = \exp\left(ie \int_0^1 \frac{dz^\mu(\lambda)}{d\lambda} A_\mu(z(\lambda)) d\lambda \right) \tag{2.30}$$

Hence, expanding and using the fundamental theorem of calculus gives:

$$\begin{aligned} W_P(x, x + \delta x) &= 1 - ie \frac{d}{dx} \int_1^0 \frac{dz^\mu(\lambda)}{d\lambda} A_\mu(z(\lambda)) d\lambda + \mathcal{O}(\delta x^2) \\ &= 1 - ie \delta x^\mu A_\mu + \mathcal{O}(\delta x^2) \end{aligned} \tag{2.31}$$

We can also check the expression for the Wilson line by applying a gauge transformation on the gauge field, eq. (2.26), showing that it transforms as it should:

$$\begin{aligned} W_P(x, y) &\to \exp\left(ie \int_y^x A_\mu(z) dz^\mu + i \int_y^x \partial_\mu \alpha(z) dz^\mu \right) \\ &= e^{ia(x)} W_P(x, y) e^{-i\alpha(y)} \end{aligned} \tag{2.32}$$

If $x = y$ we ontain a contour integral, named the Wilson loop:

$$W_P^{\text{loop}} = \exp\left(ie \oint_P A_\mu(z) dx^\mu \right) \tag{2.33}$$

Wilson loops are gauge invariant by eq. (2.32). By invoking Stoke's theorem, we can write the contour integral as:

$$W_P^{\text{loop}} = \exp\left(ie \int_\Sigma \frac{1}{2} (\partial_\nu A_\mu - \partial_\mu A_\nu) d\sigma^{\mu\nu} \right) \equiv \exp\left(i \frac{e}{2} \int_\Sigma F_{\mu\nu} d\sigma^{\mu\nu} \right) \tag{2.34}$$

where we integrate over the surface Σ (with surface element $\sigma^{\mu\nu}$) that is bounded by the path P. We define $F_{\mu\nu}$ as the field strength tensor.

Now, consider $[D_\mu, D_\nu]\phi(x)$. This naturally transformations as

$$[D_\mu, D_\nu]\phi(x) \to e^{i\alpha(x)} [D_\mu, D_\nu]\phi(x) \tag{2.35}$$

where the notation $[\cdot, \cdot]$ denotes the usual commutation relation. Writing in terms of gauge field gives:

$$[D_\mu, D_\nu]\phi(x) = \big([\partial_\mu, \partial_\nu] - ie[A_\mu, \partial_\nu] - ie[\partial_\mu, A_\nu] - e^2 [A_\mu, A_\nu] \big) \phi(x) \tag{2.36}$$

Using the following relations

$$[\partial_\mu, \partial_\nu]\phi(x) = 0 \tag{2.37}$$

$$[A_\mu, A_\nu]\phi(x) = 0 \tag{2.38}$$

$$[A_\mu, \partial_\nu]\phi(x) = A_\mu \partial_\nu \phi(x) - \partial_\nu (A_\mu \phi(x)) = -(\partial_\nu A_\mu)\phi(x) \tag{2.39}$$

$$[\partial_\mu, A_\nu]\phi(x) = (\partial_\mu A_\nu)\phi(x) \tag{2.40}$$

we find:

$$\begin{aligned}[D_\mu, D_\nu]\phi(x) &= ie(\partial_\nu A_\mu - \partial_\mu A_\nu)\phi(x) \\ &= -ie(\partial_\nu A_\mu - \partial_\mu A_\nu)\phi(x) = -ieF_{\mu\nu}\phi(x)\end{aligned} \tag{2.41}$$

Thus, $[D_\mu, D_\nu]$ turns out to be the QED field strength tensor: $F_{\mu\nu} \equiv \frac{i}{e}[D_\mu, D_\nu]$. The field strength tensor has now obtained a geometric interpretation: it is the difference between what we obtain from $D_\mu D_\nu$, which compares values of fields separated in the ν direction followed by a separation in the μ direction, and what we obtain from making the comparison in the other order as sketched in fig. 2.3. Equivalently, it is the result of comparing field values around an infinitesimal closed loop in the μ-ν plane, which is not coincidentally also the limit of the Wilson loop around a small rectangular path, as we will in subsection 2.2.3.

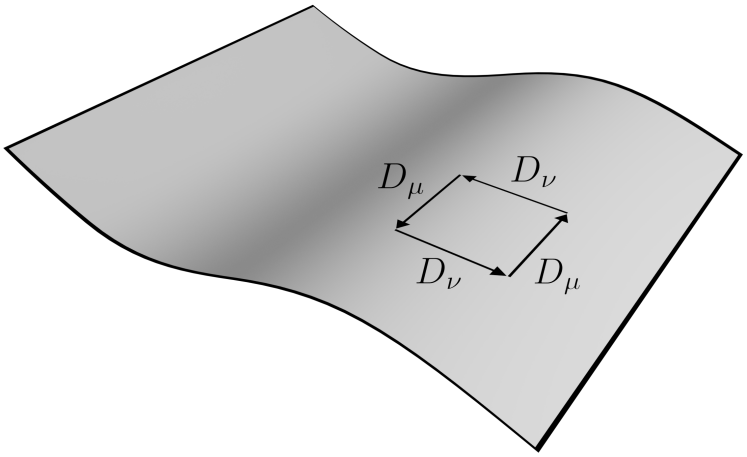

Figure 2.3: Geometric interpretation of the field strength tensor $F_{\mu\nu}$.

2.2.2 The Non-Abelian case

In the non-Abelian case we have the same problem as the Abelian case: we cannot compare field values at different points and cannot make a well-defined derivative. We investigate now the SU(N) symmetry, where the 'S' stands for special so that the determinant of a group element should be 1, in addition to the unitarity requirement as in the previous section. Since we have a larger number of degrees of freedom we obtain non-commuting generators in the exponent of a phase change, i.e. $\psi_i(x) \to \left(e^{i\alpha^a T^a}\right)_{ij}\psi_j(x)$. The $\psi(x)$'s are now Dirac spinors (details can be found in any QFT book such as [2]), which represent fermion fields. i and j, ranging from $1 \cdots N$, represent the correct matrix/vector shape multiplication. T^a is a generator of the group in the fundamental representation (we omit a subscript F for these matrices), and there are $N^2 - 1$ generators for a SU(N) group, i.e. $a = 1, \cdots, N^2 - 1$. For SU(2), these are the three well-known (2×2) Pauli matrices while for SU(3) these are the eight (3×3) Gell-Mann matrices. These matrices can be constructed by obeying the group algebra. The generators of a Lie group form a Lie algebra which is defined through its commutation relation and normalization

$$[T^a, T^b] = if^{abc}T^c, \quad \sum_{c,d} f^{acd}f^{bcd} = N\delta^{ab} \tag{2.42}$$

where f^{abc} are the structure constants, a fully antisymmetric tensor in its indices describing the structure of the algebra (for SU(3): $f^{abc} = \epsilon^{abc}$, the Levi-Civita tensor). Indeed, as we have seen in the previous subsection, the Abelian group U(1) has $f^{abc} = 0$.

Now that we understand the SU(N) symmetry, we return to Wilson's formulation. This is not as difficult anymore, because for the non-Abelian symmetry the Wilson line construction is the same. The caveat here is that we have to be careful about the non-commutative nature of the group generators. To emphasize that we are now using a different theory with a different coupling, we replace $e \to g$. Hence:

$$W_P(x,y) = P\left\{\exp\left(ig\int_y^x A_\mu^a(z)T^a dz^\mu\right)\right\} \tag{2.43}$$

where $P\{\cdots\}$ is the path-ordering operator. This can be seen as follows: the exponential in the Wilson line is defined by its Taylor expansion, and the path ordering applies to the fields in each term explicitly

$$\begin{aligned} W_P(x,y) = I + ig\int_0^1 \frac{dz^\mu(\lambda)}{d\lambda}A_\mu^a(z(\lambda))T^a d\lambda - \frac{1}{2}g^2\int_0^1 d\lambda\int_0^1 d\tau \frac{dz^\mu(\lambda)}{d\lambda}\frac{dz^\nu(\tau)}{d\tau} \\ \times A_\mu^a(z(\lambda))A_\nu^b(z(\tau))[T^aT^b\theta(\lambda-\tau) + T^bT^a\theta(\tau-\lambda)] + \cdots \end{aligned} \tag{2.44}$$

where I is the $N \times N$ identity matrix and θ is the Heaviside step function to ensure the path ordering. The Wilson line transforms similarly as in the Abelian case:

$$W_P(x,y) \to e^{i\alpha^a(x)T^a}W_P(x,y)e^{-i\alpha^a(y)T^a} \tag{2.45}$$

Therefore, it is convenient to write $\underline{A}_\mu \equiv A_\mu^a T^a$, so that the Wilson line becomes similar as in the Abelian case:

$$W_P(x,y) = P\left\{\exp\left(ig\int_y^x \underline{A}_\mu dz^\mu\right)\right\} \tag{2.46}$$

The infinitesimal expansion is now

$$W_P(x, x+\delta x) = I - ig\underline{A}_\mu dx^\mu + \mathcal{O}(\delta x^2) \tag{2.47}$$

and the covariant derivative becomes:

$$D_\mu = \partial_\mu - ig\underline{A}_\mu \tag{2.48}$$

To make the notation even more compact, we express the local transformations as:

$$U(x) = e^{i\alpha^a(x)T^a} \in \mathrm{SU}(N) \tag{2.49}$$

In summary, we have:

$$\psi(x) \to U(x)\psi(x) \quad \text{and} \quad W_P(x,y) \to U(x)W_P(x,y)U(y)^\dagger \tag{2.50}$$

To determine how A_μ^a transforms, we could just expand the transformation of W. However, a more efficient way is to utilize the fact that the covariant derivative must transform like the field $D_\mu\psi \to UD_\mu\psi$. Therefore, we can write

$$(\partial_\mu - ig\underline{A'}_\mu)U\psi = U(\partial_\mu - ig\underline{A}_\mu)\psi \tag{2.51}$$

$$\partial_\mu U\psi + U\partial_\mu\psi - ig\underline{A'}_\mu U\psi = U\partial_\mu\psi - igU\underline{A}_\mu\psi \tag{2.52}$$

$$\partial_\mu U - ig\underline{A'}_\mu U = -igU\underline{A}_\mu \tag{2.53}$$

$$\Rightarrow \underline{A'}_\mu = U\underline{A}_\mu U^{-1} - \frac{i}{g}(\partial_\mu U)U^{-1} \tag{2.54}$$

where $\underline{A'}_\mu$ denotes the transformed gauge field. Hence, $U^{-1} = U^\dagger$, and expanding gives:

$$\begin{aligned} A^{a\,\prime}_\mu T^a &= e^{i\alpha^b T^b} A^a_\mu T^a U^{-1} e^{-i\alpha^b T^b} - \frac{i}{g}(e^{i\alpha^a T^a})e^{-i\alpha^a T^a} \\ &= (I + i\alpha^b T^b) A^a_\mu T^a (I - i\alpha^b T^b) - \frac{i}{g}(i\partial_\mu \alpha^a T^a)(I - i\alpha^a T^a) + \mathcal{O}(\alpha^2) \\ &= A^a_\mu T^a + i\alpha^b A^a_\mu [T^b, T^a] + \frac{1}{g}\partial_\mu \alpha^a T^a + \mathcal{O}(\alpha^2) \end{aligned} \tag{2.55}$$

Combining eq. (2.42) with the fact that we can relabel indices, and that an antisymmetric tensor has the same sign after two permutations, allows us to write:

$$i\alpha^b A^a_\mu [T^b, T^a] = -f^{bac}\alpha^b A^a_\mu T^c = -f^{bca}\alpha^b A^c_\mu T^a = -f^{abc}\alpha^b A^c_\mu T^a \tag{2.56}$$

If we now divide eq. (2.55) by T^a, we obtain the transformation law for the gauge field:

$$A^a_\mu(x) \to A^a_\mu(x) + \frac{1}{g}\partial_\mu \alpha^a(x) - f^{abc}\alpha^b(x) A^c_\mu(x) \tag{2.57}$$

The non-Abelian field strength tensor also picks up an extra term due to the non-commutativity of the generators. Using the Abelian case (eq 2.41), and realizing that the fields in eq. (2.38) have to be multiplied with generators, we write:

$$\begin{aligned} \underline{F}_{\mu\nu} &= F^a_{\mu\nu} T^a = \partial_\mu \underline{A}_\nu - \partial_\nu \underline{A}_\mu - igA^a_\mu A^b_\nu [T^a, T^b] \\ &= \partial_\mu \underline{A}_\nu - \partial_\nu \underline{A}_\mu + gA^a_\mu A^b_\nu f^{abc} T^c \\ &= \partial_\mu \underline{A}_\nu - \partial_\nu \underline{A}_\mu + gf^{abc} A^b_\mu A^c_\nu T^a \end{aligned} \tag{2.58}$$

Again, dividing by T^a yields:

$$F^a_{\mu\nu} = \partial_\mu A^a_\nu - \partial_\nu A^a_\mu + gf^{abc} A^b_\mu A^c_\nu \tag{2.59}$$

Note that the antisymmetric nature of the field strength tensor ($F^a_{\mu\nu} = -F^a_{\nu\mu}$) is still preserved in the non-Abelian case, with $f^{abc} \neq 0$. Using a similar argument as for the gauge field, i.e. that the field strength tensor should transform as the field $F_{\mu\nu}\phi \to UF_{\mu\nu}\phi$, we find the transformation of $F_{\mu\nu}$ as follows

$$\begin{aligned} \underline{F'}_{\mu\nu} &= U\underline{F}_{\mu\nu}U^{-1} \\ &= (I + i\alpha^b T^b) F^a_{\mu\nu} T^a (I - i\alpha^b T^b) \\ &= F^a_{\mu\nu} T^a + i\alpha^b F^a_{\mu\nu} [T^a, T^b] \\ &= F^a_{\mu\nu} T^a + f^{abc}\alpha^a F^c_{\mu\nu} T^a \end{aligned} \tag{2.60}$$

hence:

$$F^a_{\mu\nu} \to F^a_{\mu\nu} + f^{abc}\alpha^a F^c_{\mu\nu} \tag{2.61}$$

We have now not only found all the fields used in the SU(N) theory, but also how they transform. We have found N fermion fields transforming in the fundamental representation, and $N^2 - 1$ boson fields transforming in the adjoint representation ($f^{abc} = i(T^a_{adj.})^{bc}$, different matrices than T_F). These fermion and boson fields represent the quarks and gluons, respectively. The gluon field was introduced as a connection, by means of the covariant

derivative. We also studied the field strength tensor and its transformation. The covariant derivative can be used to write a gauge invariant kinetic term for the fermions, and a potential term $m\bar{\psi}\psi$ (which is clearly gauge invariant) can be used to give mass to the fermions, where $\bar{\psi} = \psi^\dagger\gamma^0$. The Diract spinor ψ contains the fermion field (the quarks) and the antifermion field (the antiquarks). Although gluons are assumed to be massless (just like photons in QED), they do have a kinetic term. This kinetic term is known as the Yang-Mills Lagrangian: $\mathcal{L}_{YM} = -\frac{1}{2}\mathrm{tr}(F^a_{\mu\nu}T^aF^{\mu\nu,b}T^b)$. Due to the cyclic identity of the trace, the term is gauge invariant, and can be written as $\mathcal{L}_{YM} = -\frac{1}{4}(F^a_{\mu\nu})^2$ using the property that $\mathrm{tr}(T^aT^b) = \frac{1}{2}\delta^{ab}$ in the fundamental representation of the Lie algebra. The numerical factor of $-\frac{1}{2}$ is due to the canonical normalization. Since we are working with relativistic fields, Lorentz invariance should be obeyed by the Lagrangian. Therefore, the spinor fields must be multiplied in an appropriate way with γ^μ matrices. Using the Feynman slash notation ($\not{A} = \gamma^\mu A_\mu$), we can now write down the locally SU(N) invariant Lagrangian:

$$\mathcal{L} = -\frac{1}{4}(F^a_{\mu\nu})^2 + \sum_{i,j=1}^{N} \bar{\psi}_i(\delta_{ij}i\not{\partial} + g\not{A}^aT^a_{ij} - m\delta_{ij})\psi_j \tag{2.62}$$

where the summation over N indicates the possible 'color' charges and hence we have conservation of color in the Lagrangian.

As this work only concerns the gluonic part (glueballs are made up of gluons), we drop the fermionic part in the Lagrangian. This results in us studying the pure Yang-Mills theory:

$$\mathcal{L}_{YM} = -\frac{1}{4}(F^a_{\mu\nu})^2 \tag{2.63}$$

Before we proceed to the discretization of SU(N) theories on the lattice, there is still one more important point we would like to make. Again, due to the non-commutativity of the generators, we have an extra term in the definition of the field strength tensor, eq. (2.59). For this reason QCD (and in fact every other SU(N) theory) also has vertices of three and four interacting bosons, in addition to the boson propagator, the fermion propagator, and the boson-fermion-fermion interaction. The self-interactions of the bosons come from the Yang-Mills Lagrangian: the square of $F_{\mu\nu}$ generates these vertices. It are these interactions that make gluons stick together and theoretically form massive glueball states.

2.2.3 Pure SU(N) Yang-Mills action on the lattice

Lattice gauge theory seems to be the only improvable method for computing non-perturbative gauge theories nowadays. The lattice formulation is a simple extension of what we have discussed in the previous section, but, instead of a continuous path, we consider a discrete lattice. In such a discrete lattice theory, we should always ensure that we recover the continuum limit (the Yang-Mills Lagrangian) when the lattice spacing goes to zero.

We define a 3+1 dimensional lattice with N_{sites} in each dimension, spaced a distance a apart. The metric on the lattice is naturally Euclidean, and we take the dimensions of the lattice to be equally large (for now). On the lattice, QFT reduces to QM with N^4_{sites} fields. The matter fields $\phi(n)$ reside naturally on the lattice sites n. $\phi(n)$ and $\phi(n+\hat{\mu})$ denote the field values on the nearest neighbor sites. Here, μ denotes a unit vector of length a in the μ-direction. Because the gauge transformations are now also discrete, we rotate fields by group elements defined separately on each site:

$$\phi(n) \to U(n)\phi(n), \quad U(n) = e^{i\alpha^a(n)T^a} \tag{2.64}$$

To compare field values at different sites in a gauge invariant way, we need the discrete version of the Wilson line. For this, we define the transformation

$$W_\mu(n) \to U(n) W_\mu U^\dagger(n+\hat{\mu}) \tag{2.65}$$

so that:

$$\begin{aligned}\phi^\dagger(n) W_\mu(n) \phi(n+\hat{\mu}) &\to \phi^\dagger(n) U^\dagger(n) U(n) W_\mu(n) U^\dagger(n+\hat{\mu}) U(n+\hat{\mu}) \phi(n+\hat{\mu}) \\ &= \phi^\dagger(n) W_\mu(n) \phi(n+\hat{\mu})\end{aligned} \tag{2.66}$$

Now, the products of fields on distant lattice sites can be multiplied in a gauge invariant way by multiplying together $W_\mu(n_i)$ factors along any path between the sites. The W_μ fields are thought to live between neighboring sites, and are therefore called link fields.

To connect any two sites, we have one link between every neighboring pair and for convenience we define

$$W_{-\mu} = W^\dagger(n-\hat{\mu}) \tag{2.67}$$

which acts as a link in the opposite direction. Analogous to the continuum case, we write:

$$W_\mu = \exp[ia \underline{A}_\mu(n)] \tag{2.68}$$

where a is the lattice spacing, and $\underline{A}_\mu(n) = A^a_\mu T^a$ as before. The coupling g, which is not necessarily a useful quantity in the discussion, has been absorbed into the gauge field.

To construct the Yang-Mills action, we need a gauge invariant observable constructed out of link fields. As already mentioned, these are the analogs of the Wilson loops. Indeed, from the transformation property, eq. (2.65), any trace of a closed loop of links is gauge invariant, because of the cyclic identity of the trace. The simplest loop goes between two sites and back. However, since $W_\mu(n) W_{-\mu}(n+\hat{\mu}) = I$, this is not a particularly useful quantity. The next simplest loop goes in a little square: a plaquette, shown in fig. 2.4. The plaquette is constructed as follows:

$$\begin{aligned}W_{\mu\nu} &\equiv W_{-\nu}(n+\hat{\nu}) W_{-\mu}(n+\hat{\mu}+\hat{\nu}) W_\nu(n+\hat{\mu}) W_\mu(n) \\ &= W^\dagger_\nu(n) W^\dagger_\mu(n+\hat{\nu}) W_\nu(n+\hat{\mu}) W_\mu(n)\end{aligned} \tag{2.69}$$

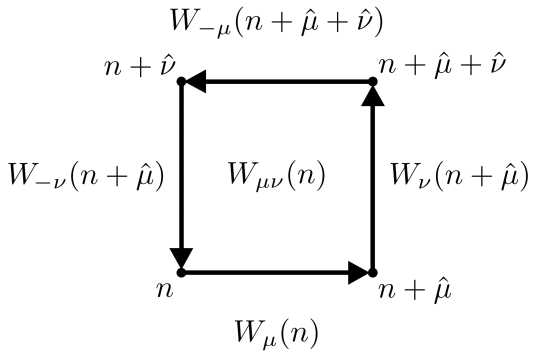

Figure 2.4: Visual representation of a plaquatte.

We now want to relate the plaquette to the continuum field strength. This can be done by using the Campbell-Baker-Hausdorf formula: $\exp(A)\exp(B) = \exp(A+B+1/2[A,B]+\cdots$, because of the non-commutativity of the exponents of the links. Up to order a^2 we write:

$$\begin{aligned}
W_{\mu\nu} &= \exp(-ia\underline{A}_\nu(n))\exp(-ia\underline{A}_\mu(n+\hat{\nu}))\exp(ia\underline{A}_\nu(n+\hat{\mu}))\exp(ia\underline{A}_\mu(n)) \\
&= \exp\big(-ia\underline{A}_\nu(n) - ia\underline{A}_\mu(n+\hat{\nu}) - \frac{a^2}{2}[\underline{A}_\nu(n), \underline{A}_\mu(n+\hat{\nu})] + \cdots\big) \\
&\times \exp\big(ia\underline{A}_\nu(n+\hat{\mu}) + ia\underline{A}_\mu(n) - \frac{a^2}{2}[\underline{A}_\nu(n+\hat{\mu}), \underline{A}_\mu(n)] + \cdots\big) \\
&= \exp\big(-ia\underline{A}_\nu(n) - ia\underline{A}_\mu(n+\hat{\nu}) + ia\underline{A}_\nu(n+\hat{\mu}) + ia\underline{A}_\mu(n) \\
&- \frac{a^2}{2}\Big\{[\underline{A}_\nu(n), \underline{A}_\mu(n+\hat{\nu})] + [\underline{A}_\nu(n+\hat{\mu}), \underline{A}_\mu(n)] \\
&- [\underline{A}_\nu(n) + \underline{A}_\mu(n+\hat{\nu}), \underline{A}_\nu(n+\hat{\mu}) + \underline{A}_\mu(n)]\Big\} + \mathcal{O}(a^3)\big)
\end{aligned} \tag{2.70}$$

To connect to the continuum limit we Taylor expand

$$\underline{A}_\nu(n+\hat{\mu}) = \underline{A}_\nu(n) + a\partial_\mu\underline{A}_\nu(n) + \mathcal{O}(a^2) \tag{2.71}$$

which gives:

$$\begin{aligned}
\ln\big(W_{\mu\nu}(n)\big) &= ia\{\underline{A}_\mu(n) + \underline{A}_\nu(n) + a\partial_\mu\underline{A}_\nu(n) - \underline{A}_\mu(n) - a\partial_\nu\underline{A}_\mu(n) - \underline{A}_\nu(n)\} \\
&+ \frac{a^2}{2}\Big\{[\underline{A}_\nu(n) + \underline{A}_\mu(n) + a\partial_\nu\underline{A}_\mu(n), \underline{A}_\nu(n) + a\partial_\mu\underline{A}_\nu(n) + \underline{A}_\mu(n)] \\
&- [\underline{A}_\nu(n), \underline{A}_\mu(n) + a\partial_\nu\underline{A}_\mu(n)] - [\underline{A}_\nu(n) + a\partial_\mu\underline{A}_\nu(n), \underline{A}_\mu(n)]\Big\} + \mathcal{O}(a^4) \\
&= \left\{ia^2\left(\partial_\mu\underline{A}_\nu - \partial_\nu\underline{A}_\mu\right) - \frac{a^2}{2}\left(2[\underline{A}_\nu, \underline{A}_\mu] - [\underline{A}_\mu, \underline{A}_\mu] - [\underline{A}_\nu, \underline{A}_\nu]\right)\right\} + \mathcal{O}(a^3)
\end{aligned} \tag{2.72}$$

Now, using the fact that $[A,B] = -[B,A]$ and that $[\underline{A}_\mu, \underline{A}_\mu] = A^a_\mu A^b_\mu [T^a, T^b] = iA^a_\mu A^b_\mu f^{abc}T^c = iA^b_\mu A^a_\mu f^{bac}T^c = 0$ because $f^{abc} = -f^{bac} \neq f^{bac}$, we write

$$\begin{aligned}
W_{\mu\nu}(n) &= \exp\Big\{ia^2\big(\partial_\mu\underline{A}_\nu(n) - \partial_\nu\underline{A}_\mu(n)\big) + a^2[\underline{A}_\mu(n), \underline{A}_\nu(n)] + \mathcal{O}(a^3)\Big\} \\
&= \exp\Big\{ia^2\underline{F}_{\mu\nu} + \mathcal{O}(a^3)\Big\}
\end{aligned} \tag{2.73}$$

where we used $\underline{F}_{\mu\nu}$ from eq. (2.58). Expanding at small a gives us:

$$W_{\mu\nu}(n) = I + ia^2\underline{F}_{\mu\nu} - \frac{a^4}{2}\underline{F}^2_{\mu\nu} + \mathcal{O}(a^6) \tag{2.74}$$

What we are looking for is something that approaches the discretization of the continuum Euclidean Yang-Mills action after rescaling $A_\mu \to \frac{1}{g}A_\mu$:

$$S_{YM,E} = \int d^4x \left[\frac{1}{4g^2}(F^a_{\mu\nu})\right] \tag{2.75}$$

Therefore, the Yang-Mills action on the lattice with inverse coupling β_L, the Wilson action, is defined as:

$$S_{\text{lattice}}[W_{\mu\nu}] = \frac{a^4}{2g^2}\sum_{n,\mu,\nu}\text{tr}(\underline{F}^2_{\mu\nu}) = \frac{\beta_L}{N}\sum_{n,\mu>\nu}\text{Re tr}(I - W_{\mu\nu}), \quad \beta_L = \frac{2N}{g^2} \tag{2.76}$$

Where $\mu > \nu$ indicates that all plaqettes are going counterclockwise and we sum over all plaquettes in the lattice at every lattice point n. This action will be used to evaluate the Boltzmann term in the Green's functions by summing over the plaquette values. However, this derivation of the action is only up to order a^2 and one can do better by evaluating higher orders. Another improvement is to include tadpole improvement, which is done by dividing each link by the mean link or the fourth root of the plaqette expectation value $u_0 = \langle 0|W_{\mu\nu}|0\rangle^{1/4}$, since that observable only consists of tadpoles. A tadpole is named after its diagram shape and does not depend on the external momenta of the gluon fields, i.e. is scale-less. According to P.G. Lepage [5], one can build an improved action for example as follows

$$S = \frac{\beta_L}{N} \sum_{n,\mu>\nu} \mathrm{Re\ tr}\left(I - \frac{5}{3}\frac{W_{\mu\nu}}{u_0^4} - \frac{R_{\mu\nu} + R_{\nu\mu}}{16u_0^6} \right) \tag{2.77}$$

where $R_{\mu\nu}$ are flat rectangles of six links. The mean link u_0 can be computed iteratively by guessing a value to use in the action, measure the mean link, and then readjusting u_0 accordingly. According to Lepage, this tuning cycle converges rapidly and can be done very quickly, especially on small lattice volumes. Note that, the tadpole improvement is effectively a rescaling of β_L, since for every β_L the average plaquette expectation value gives a certain value. The tadpole improvement makes effectively β_L larger (since u_0 is typically small) and therefore the coupling smaller. Our main algorithm for the lattice computations will be based on eq. (2.76), so for practical purposes we have decided to stay in first instance with the simple plaquette action.

2.3 The Haar measure

In this section we will look at the measure of Green's functions on the Yang-Mills lattice. This section is based on the book [6] of C. Gattring & C.B. Lang, as are the following sections. To recap, the quantization of the system in the path integral formalism is implemented as an integral over all field configurations defined in the measure. On the lattice, the integration measure for the link variables is the product measure over the link fields

$$D[W] = \prod_{n\in\Lambda} \prod_{\mu}^{4} dW_\mu \tag{2.78}$$

where Λ denotes all points in the four-dimensional lattice. The action is gauge invariant $S[W'_{\mu\nu}] = S[W_{\mu\nu}]$, and therefore the functional integral, so we can write:

$$Z = \int D[W]\, e^{-S[W_{\mu\nu}]} = \int D[W']\, e^{-S[W'_{\mu\nu}]} = \int D[W']\, e^{-S[W_{\mu\nu}]} \tag{2.79}$$

This means that $D[W'] = D[W]$, so the measure is of course also gauge invariant. We find the condition that

$$dW_\mu(n) = dW'_\mu(n) = d(U(n)W_\mu(n)U^\dagger(n+\hat{\mu})) \tag{2.80}$$

for the integration over the individual link variables. The measure, called the Haar measure, is a measure for integrating over a continuous compact group G, such as the SU(N) group. Since $U(n)$ and $U(n+\hat{\mu})$ can be chosen independently, the measure dW for a group element must be invariant under left and right multiplication with another group element $V \in G$:

$$dW = d(WV) = d(VW) \tag{2.81}$$

Eq. (2.81) and the normalization (integration over all of G)

$$\int dW \;\; 1 = 1 \tag{2.82}$$

are the defining properties of the Haar measure.

To become more familiar with how the Haar measure works, we show a few SU(N) integrals. The basic tool for analyzing these integrals is the following equation for integrals over functions $f(W)$

$$\int dW f(W) = \int dW f(VW) = \int dW f(WQ) \tag{2.83}$$

where V and Q are arbitrary SU(N) matrices. This relation follows directly from eq. (2.81). We start with the integral over an individual link

$$\int dW W_{ij} = \int dW (VW)_{ij} = V_{ik} \int dW W_{kj} \tag{2.84}$$

where the subscripts denote the matrix structure of the links. For eq. (2.84) we must have $V_{ik} = \delta_{ik}$. However, the last equation must hold for arbitrary group elements V, such that the integral vanishes:

$$\int dW W_{ij} = 0 \tag{2.85}$$

Equivalently for the integral over the product of two links:

$$\int dW W_{ij} W_{lk} = 0 \tag{2.86}$$

However, the following integral will give us a non-zero outcome:

$$\int dW W_{ij} (W^\dagger)_{lk} \overset{j=l}{=} \int dW (W_{i1}(W^\dagger)_{1k} + W_{i2}(W^\dagger)_{2k} + \cdots + W_{iN}(W^\dagger)_{Nk}) \tag{2.87}$$

$$= \int dW (WW^{-1})_{ik} = \int dW \delta_{ik} = \delta_{ik} \Rightarrow \int dW W_{ij} (W^\dagger)_{lk} = \frac{1}{N} \delta_{ik} \delta_{jl} \tag{2.88}$$

In eq. (2.88) we have used that $W^\dagger = W^{-1}$ and the normalization of the Haar measure, eq. (2.82). For the right hand side of eq. (2.87), it is important to realize that the N contributions are entirely equivalent. For example, the first term can be transformed into the second term by exchanging rows 1 and 2 as well as columns 1 and 2. This operation transforms an element of SU(N) into another group element, and both of these elements are summed over in the group integral. This equivalence implies that each of the N terms contributes $1/N$ to the result. This equation is interesting since it allows one to integrate the common link variable that occurs in a product of two traces of plaquettes, resulting in a trace of link variables around the two plaquettes, as in fig. 2.5, for SU(3):

$$\int dW \mathrm{tr}[VW] \mathrm{tr}[W^\dagger Q] = \frac{1}{3} \mathrm{tr}[VQ] \tag{2.89}$$

The essence here is that the integral only gives a nonvanishing result if the integrand contributes to 1, i.e. the Haar measure projects out the contribution of the integrand to the

trivial or singlet representation of the gauge group, and does so when the integrand is gauge invariant.

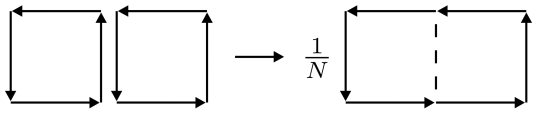

Figure 2.5: Integration of a common link on a SU(N) lattice.

2.4 Wilson and Polyakov loops

In this section a general discussion is provided on gauge invariant observables that can be constructed on the pure Yang-Mills lattice. From the moment we constructed plaquettes, we know that prototypes of gauge invariant observables, made from only gauge fields, are the trace of a product of link variables forming a loop. Loops of size larger than the plaquette are just named Wilson loops, which we now define on the lattice. First, we define a product of link variables as:

$$L[W] = \mathrm{tr}\Big[\prod_{n,\mu\in L} W_\mu(n)\Big] \tag{2.90}$$

where L is a closed loop of links on the lattice, and the product runs over these links. We divide the link product along different space-time directions in spatial and temporal products. The spatial product becomes:

$$S(m,n,n_t) = \prod_{(k,j)\in\mathcal{C}_{m,n}} W_j(k,n_t) \tag{2.91}$$

This connects two spatial points m and n along some path $\mathcal{C}_{m,n}$ with all link variables restricted to the time argument n_t. The temporal product becomes

$$T(n,n_t) = \prod_{j=0}^{n_t-1} W_4(n,j)$$

taking $\mu = 4$ to be the time direction. This is a straight line of n_t link variables in the time direction, all situated at spatial position n. Attaching four pieces gives a closed loop $\mathcal{L}$:

$$\mathcal{L} : (m,n_t) \xrightarrow{S} (n,n_t) \xrightarrow{T^\dagger} (n,0) \xrightarrow{S^\dagger} (m,0) \xrightarrow{T} (m,n_r) \tag{2.92}$$

To define a Wilson loop on the lattice, we take the trace of $\mathcal{L}$:

$$W_\mathcal{L}[W] = \mathrm{tr}[S(m,n,n_t)T^\dagger(n,n_t)S^\dagger(m,n,0)T(m,n_t)] \tag{2.93}$$

If the piece of loop $\mathcal{C}_{m,n}$ used in $S(m,n,n_t)$ is a straight line in one spatial dimension, we speak of a planar Wilson loop. Otherwise the loop is called non-planar. Examples of both of these kinds of loops are shown in fig. 2.6.

Another observable can be constructed if we specify certain boundary conditions for the gauge fields. If we choose boundary conditions that are periodic in the time direction and make the temporal extent n_t of the Wilson loop as large as possible (i.e. $n_t \to N_t$, where N_t is the total number of lattice points in the time direction), then the spatial pieces of the Wilson loop sit on top of each other but are oriented in the opposite direction. If we gauge

the spatial pieces of the loop to the identity element I, the Wilson loop reduces to the two disconnected paths of temporal link variables, $T(m, N_t)$ and $T^\dagger(n, N_t)$, located in space at the two positions m and n. Both of these paths wind around the temporal direction of the lattice but have opposite orientations. The observable we find is the Polyakov loop:

$$P_L[W] = \mathrm{tr} \prod_{j=0}^{N_t-1} W_4(m, j) \tag{2.94}$$

In summary, we have found two possible ways to construct gauge invariant observables on the lattice, besides the trace of plaquettes: the Wilson and Polyakov loops, where the latter was only introduced for completeness. In fact, the glueball observables on the lattice are constructed using solely a spatial form of Wilson loops. We will construct these observables later on since it requires a more in-depth discussion.

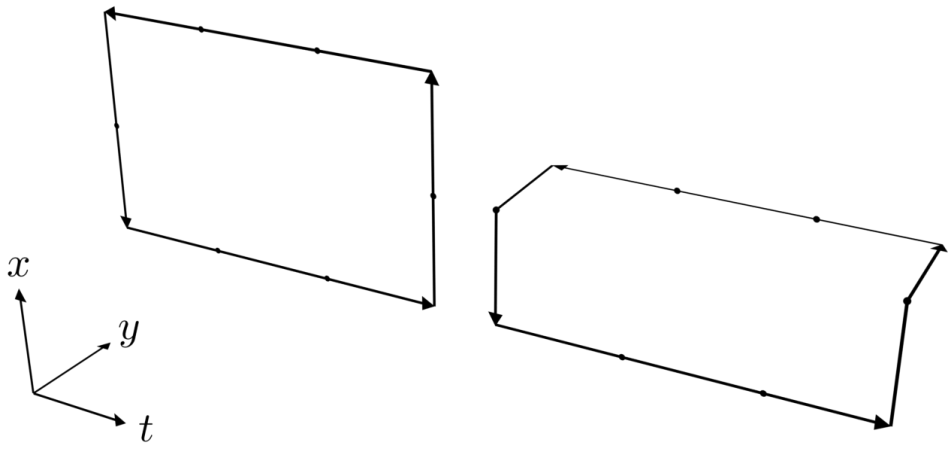

Figure 2.6: A planar (left) and a non-planar Wilson loop (right).

2.5 Propagation in Euclidean time

In Euclidian space time we can obtain the mass of a particle from the 2-point correlator. Take for example an operator $\mathcal{O}$, representing a glueball with the right quantum numbers. We have already seen that the 2-point correlation function of the same particle (the propagator) represents the probability amplitude of a particle travelling from the one to the other space-time coordinates, where the particle is created out of the vacuum, propagates, and is annihilated back to the vacuum. The chance of this happening can tell us about the physical properties of the particle we are inspecting. To see this, we use a QM argument to inspect the left hand side of eq. (2.20). Note that, therefore, the final result of this section also holds in the path integral formalism in favour of observables in the lattice computation.

From a QM perspective, we can define the 2-point Euclidian correlator for an operator at two different times as:

$$\langle \mathcal{O}_2(t)\mathcal{O}_1(0)\rangle_T = \frac{1}{Z_T}\ \mathrm{tr}[e^{-(T-t)H}\mathcal{O}_2\ e^{-tH}\mathcal{O}_1] \tag{2.95}$$

$$Z_T = \mathrm{tr}[e^{-TH}] \tag{2.96}$$

where H is again the Hamiltonian operator, which governs the time evolution, and Z_T is the partition function. The parameters T and t are real, non-negative numbers denoting Euclidean time distance of propagation, where t is the actual distance of interest to us, and T is a formal maximal distance, which will be taken to be infinite in the end. We first evaluate the partition function, eq. (2.96). To evaluate the trace, we sandwich the operator between vectors of an orthonormal basis, then sum over all basis vectors. As usual, we choose the basis of the eigenstates of H as those in eq. (2.14). The eigenstates are denoted as $|n\rangle$, such that: $H|n\rangle = E_n|n\rangle$. The energy eigenvalues E_n are real numbers, and the states are ordered as follows, $E_0 \leq E_1 \leq E_2 \leq \cdots$, where the index n labels all the combinations of quantum numbers describing the states. We now write the partition function as:

$$Z_T = \sum_n \langle n|e^{-TH}|n\rangle = \sum_n e^{-TE_n} \quad (\langle n|n\rangle = 1)$$

We evaluate the correlator in a similar way:

$$\begin{aligned}\langle \mathcal{O}_2(t)\mathcal{O}_1(0)\rangle_T &= \frac{1}{Z_T}\sum_{m,n}\langle m|e^{-(T-t)H}\mathcal{O}_2|n\rangle\langle n|e^{-tH}\mathcal{O}_1|m\rangle \\ &= \frac{\sum_{m,n}\langle m|\mathcal{O}_2|n\rangle\langle n|\mathcal{O}_1|m\rangle e^{-(T-t)\Delta E_m}\ e^{-t\Delta E_n}}{1+e^{-T\Delta E_1}+e^{-T\Delta E_2}+\cdots}, \quad \Delta E_n \equiv E_n - E_0\end{aligned} \tag{2.97}$$

Thus, the Euclidean correlator depends only on the energies normalized relative to the energy E_0 of the vacuum. It is exactly these energy differences that can be measured in an experiment. Now we use E_n to denote the energy difference relative to the vacuum, i.e. $E_n = \Delta E_n$. Analyzing the limit $T \to \infty$, the denominator equals 1 (assuming the vacuum is unique) and in the numerator only those terms where $E_m = 0$ survive, hence $|m\rangle = |0\rangle$:

$$\langle \mathcal{O}_2(t)\mathcal{O}_1(0)\rangle_E = \lim_{T\to\infty}\langle \mathcal{O}_2(t)\mathcal{O}_1(0)\rangle_T = \sum_n \langle 0|\mathcal{O}_2|n\rangle\langle n|\mathcal{O}_1|0\rangle\ e^{-tE_n} \tag{2.98}$$

By subtracting the product of vacuum expectation values of each operator separately, we can now write the 2-point connected correlation function as follows:

$$\langle \mathcal{O}_2(t)\mathcal{O}_1(0)\rangle - \langle \mathcal{O}_2(t)\rangle\langle \mathcal{O}_1(0)\rangle = \sum_{n\neq 0}\langle 0|\mathcal{O}_2|n\rangle\langle n|\mathcal{O}_1|0\rangle\ e^{-tE_n} \tag{2.99}$$

This expression is central to the interpretation of lattice field theory. It is a sum of exponentials, where each exponent corresponds to an energy level. The energy of the ground state E_0, redefined as $E_1 \to E_0$, dominates the correlator at large time scales:

$$\langle \mathcal{O}_2(t)\mathcal{O}_1(0)\rangle - \langle \mathcal{O}_2(t)\rangle\langle \mathcal{O}_1(0)\rangle \xrightarrow{t\to\infty} \langle 0|\mathcal{O}_2|0\rangle\langle 0|\mathcal{O}_1|0\rangle\ e^{-tE_0} \tag{2.100}$$

Note that the factor in front of the exponential can be seen as a constant. The energy of a particle in relativistic units ($c = 1$) is given by $E_n^2 = p_n^2 + m^2$, and for the ground state is assumed that $p_0 = 0$. So, by fitting a single exponential $A\,e^{-mt}$ to the 2-point connected correlator at large times, we can obtain the mass of the glueball.

2.6 zero-temperature and the lattice

In this section, we are going to explain how temperature works on the lattice. This section is based on a section of A. Zee's book [1]. The natural framework is again the correlation function and a cubic lattice formulation with a lattice spacing a. To understand the path integral representation of a QFT in terms of temperature, we use the well-known thermal partition function, assuming that the system is in thermal equilibrium:

$$Z(T,V) \equiv \mathrm{tr}[e^{-\beta H}] \equiv \sum_n \langle n|e^{-\beta H}|n\rangle = \sum_n e^{-\beta E_n}, \quad \beta = \frac{1}{kT} \tag{2.101}$$

For convenience, we set Boltzmann's constant $k = 1$. Following eq. (2.10), which tells us how to write the amplitude for the propagation of a field in the time interval given by T, we can now interpret the inverse temperature $1/T$ as a time variable, and after Wick rotating eq. (2.10), we write:

$$\langle \phi_F(x)|e^{-H/T}|\phi_I(x)\rangle = \int D\phi \, \exp\Big[- \int_0^{1/T} dt \int d^3x \mathcal{L} \Big] \tag{2.102}$$

In order to calculate the trace over states, we put $\phi_F(\vec{x}) = \phi_I(\vec{x})$. The resulting expression for the partition function is almost equal to eq. (2.19), where the time variable of the action now runs from 0 to $1/T$, and the field ϕ is taken with periodic boundary conditions,

$$\phi(\vec{x}, 1/T) = \phi(\vec{x}, 0) \tag{2.103}$$

such that we can write:

$$Z(T,V) = \int D\phi \, \exp\Big[- \int_0^{1/T} dt \int d^3x \mathcal{L} \Big] \tag{2.104}$$

The exponent in eq. (2.104) reproduces the standard Euclidean action of QFT in the limit $T \to 0$. Hence, in QFT, we normally work in the zero-temperature limit. The point is that noting depends on real-time for a system in thermodynamic equilibrium. Consider N_t to be the size of the temporal direction of our lattice and N_s the size of the spatial ones. Eq. (2.104) implies that the temperature on the lattice is:

$$T = \frac{1}{aN_t} \tag{2.105}$$

However, we are work in Euclidean space-time in which every direction is treated on equal footing, i.e. the signs of the metric for the different coordinates are the same. Any of the four can be chosen as the temporal one, so to obtain a lattice of zero-temperature one naturally takes:

$$N_t \gg N_s \tag{2.106}$$

Note that one can also choose to do a finite temperature computation instead by taking $N_t \ll N_s$. However, we have chosen to stick with the zero-temperature system in this study.

3 Large-N and Quantum Chromodynamics

The goal of this work is to study the glueball spectrum in the large-N limit of QCD. This limit concerns the number of degrees of freedom of the SU(N) theory, where we take N to tend to infinity. In section 3.1, we will explain the mathematical structure of the large-N limit. Thereafter, in sections 3.2 and 3.3, we will understand why the large-N limit is so interesting to study. In section 3.4, we will conclude by discussing a recently proposed nonperturbative solution and candidates for the glueball spectrum. This motivates why we want to study the glueball masses in the large-N limit. The discussion in this chapter is an isolated discussion with respect to the lattice, mostly based on the reviews by A.V. Manohar [7] and B. Lucini & M. Panero [8].

3.1 't Hooft limit and N-counting rules

In the 1970's, G. 't Hooft was the first physicist to study the large-N limit for non-Abelian gauge theories [9], in particular QCD. 't Hooft suggested a generalization of the theory, in which the number of color charges N goes to infinity in the following way: $g \to 0$ and $N \to \infty$, so that the 't Hooft coupling stays fixed $\lambda = g^2 N$. This implies that the number of quark flavors n_f could be scaled too, however, 't Hooft proposed to hold n_f fixed. To make sense of the 't Hooft limit, at least perturbatively, we will first look to the β-function. Thereafter, we explore the N-counting rules in the 't Hooft limit. We will use these to see some of the simplifications in the 't Hooft limit, on which we further elaborate in the next section.

In continuum perturbation theory we use the renormalization group to treat the UV-divergent Feynman diagrams. The first step in renormalizing depends on one or more parameters which are introduced in the regularization scheme. Since the procedure is to make the momentum integration ultraviolet finite, we can view it as that the regularization scheme introduces a momentum cutoff, equivalent an energy scale μ. The second step in the renormalization procedure consists of defining the renormalized Green's functions, which approach a finite limit as the cutoff is removed. This demands that the bare parameters of the theory become cutoff dependent, such as the coupling g, by imposing a set of renormalization conditions. The dependence of the coupling g on the energy scale is described by the β-function:

$$\frac{dg}{d\ln(\mu)} = \beta(g) \tag{3.1}$$

In the perturbative regime $g \ll 1$, eq. (3.1) is well approximated by the first two terms of the QCD β-function. These terms, up to two-loop ($\mathcal{O}(g^5)$), are universal, i.e do not depend on the choice of renormalization scheme:

$$\mu\frac{dg}{d\mu} = -\frac{1}{(4\pi)^2}\left(\frac{11N - 2n_f}{3}\right)g^3 - \frac{1}{(4\pi)^4}\left(\frac{34N^3 - 13N^2 n_f + 3n_f}{3N}\right)g^5 + \mathcal{O}(g^7) \tag{3.2}$$

If we now introduce the 't Hooft limit in terms of λ, we find:

$$\mu\frac{d\lambda}{d\mu} = -\frac{11}{24\pi^2}\lambda^2 - \frac{17}{192\pi^4}\lambda^3 + \mathcal{O}(\lambda^4) \tag{3.3}$$

Notice that the coefficients on the right-hand side are still negative as in eq. (3.2). Eq. (3.3) predicts that the 't Hooft limit of QCD is an asymptotically free theory like normal QCD, and therefore governs the same dynamics. This means that at large energy scales or small distances, the theory becomes free, i.e. the coupling goes asymptotically to zero. By taking

the β-function only up to order λ^2, we can solve this differential equation and observe the asymptotic freedom more clearly

$$\mu = \Lambda_{\mathrm{SU}(N)}\, e^{\frac{24\pi^2}{33\lambda^3}} \tag{3.4}$$

where $\Lambda_{\mathrm{SU}(N)}$ is the integration constant or scale parameter which has the dimension of energy. This is interesting because the pure Yang-Mills theory has no dimensional parameters, g is dimensionless, and there is no mass term in its classical action. This phenomenon is associated with dimensional transmutation and is a pure quantum effect. Another interesting feature due to the large-N limit, is that eq. (3.3) does not depend on n_f, and hence is subleading with respect to the number of gluon degrees of freedom. In fact, there are also other large-N descriptions, such as the Veneziano limit (where n_f is sent to infinity holding the n_f/N ratio fixed), however, these turned out to lead to more complicated computations. They are therefore not considered in this work.

The properties and simplifications of QCD in the 't Hooft limit can be studied in terms of the N-counting rules, which requires two ingredients. Again, the number of color degrees of freedom becomes large, the coupling becomes small, and λ is kept fixed, so in this limit it is convenient to write the Feynman rules by replacing g with $\sqrt{\lambda/N}$. This replacement is not enough as we also require the double-line notation. First consider the quark propagator:

$$\langle \psi^i(x)\bar{\psi}^j(y)\rangle = \delta^{ij} S(x-y) \tag{3.5}$$

This diagrammatically represents a single line, i.e. a fermionic field propagating from space-time position x to y or an antifermion doing the opposite, traveling back in time. Because of the δ^{ij}, the color at the beginning of the line is the same as at the end of the line, hence, color is conserved. Note that the term $S(x-y)$ describes the exact rule of propagation. The gluon propagator can be written as

$$\langle A^a_\mu(x) A^b_\nu(y)\rangle = \delta^{ab} D_{\mu\nu}(x-y) \tag{3.6}$$

with similar interpretation, except for the fact that the gluon is now its own anti-particle. Under conjugation, the gluon goes into a gluon and a and b are now indices in the adjoint representation, ranging from 1 to N^2-1. The index is also here conserved in the propagation (indicated by the delta function), and again $D_{\mu\nu}(x-y)$ describes the exact rule of propagation. General theoretical observations of group theory allow an adjoint index to be written as a pair of fundamental and anti-fundamental indices: $A^a_\mu = A^{ij}_\mu (T^a)^{ij}$. Using this, the gluon propagator becomes

$$\langle A^{ij}_\mu(x) A^{kl}_\nu(y)\rangle = \left(\frac{1}{2}\delta^{il}\delta^{kj} - \frac{1}{2N}\delta^{ij}\delta^{kl}\right) D_{\mu\nu}(x-y) \to \frac{1}{2}\delta^{il}\delta^{kj} D_{\mu\nu}(x-y) \tag{3.7}$$

where in the propagation the adjoint indices cannot change, i.e. $a = b$, and the identity $\sum_a T^a_{ij} T^a_{kl} = \frac{1}{2}\delta_{il}\delta_{kj} - \frac{1}{2N}\delta_{ij}\delta_{kl}$ in SU(N) was used. As we are in the large-N limit, we omit the second term. In U(N) the identiy is $\sum_a T^a_{ij} T^a_{kj} = \frac{1}{2}\delta_{il}\delta_{kj}$, so we effectively work with this gauge symmetry. Diagrammatically we are left with two lines: one propagating from x to y and the other propagating from y to x. So, we have obtained the double-line notation. In fig. 3.1, the Feynman interaction rules are shown with the double-line notation together with the appropriate order of these diagrams.

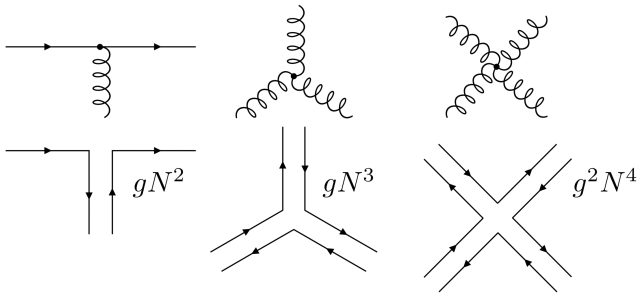

Figure 3.1: Interactions in the double-line notation with the appropriate order: the single line represents the quark and the double-line represents the gluon, which is usually drawn with a spiral line.

With this notation, we can see from the orders of diagrams that in the 't Hooft limit amplitudes for physical processes are dominated by planar and so-called quenched diagrams. Respectively this means that diagrams are to be drawn flat, i.e. no internal crossing lines, and that the loops do not contain virtual or internal quark loops. The order of these diagrams (as in fig. 3.1) can be observed from the Lagrangian, eq. (2.62), and the field strength tensor, eq. (2.59). Every gluon-quark-quark and three gluon interaction gives a factor g. A four gluon vertex goes as g^2. Moreover, every line gives a factor N, since there are N colors to choose for each line. With these rules, we can find the order of any diagram. However, we still have to incorporate the 't Hooft limit by replacing the coupling g with the coupling λ. A few examples of this are shown in fig. 3.2, revealing that indeed non-planar quenched diagrams dominate the theory in the 't Hooft limit. It should be noted that including more or fewer gluons in the left diagram of fig. 3.2 does not change the order of N (only of λ), because the amount of g changes accordingly. So, pure planar gluonic diagrams are always $\mathcal{O}(N^2)$.

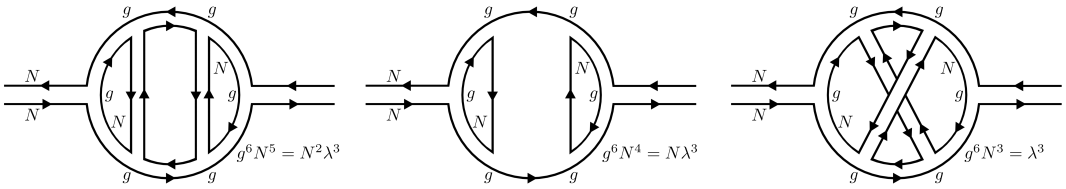

Figure 3.2: Example diagrams with double-line notation and the order in the 't Hooft limit. Left: dominating pure gluonic graph, middle: diagram with an internal quark loop, right: non-planar gluonic graph.

To better understand the N-dependence of diagrams, we rescale the Lagrangian, eq. (2.62), by $A \to \frac{1}{g}A = \sqrt{\frac{N}{\lambda}}A$ and $\psi \to \sqrt{N}\psi$. So, we write:

$$\mathcal{L} = N\Big[-\frac{1}{4\lambda}(F^a_{\mu\nu})^2 + \sum_{i,j=1}^{N} \bar{\psi}_i(\delta_{ij}i\partial\!\!\!/ + A\!\!\!/^a T^a_{ij} - m\delta_{ij})\psi_j \Big] = N\tilde{\mathcal{L}} \tag{3.8}$$

The Lagrangian now has an overall factor of N. Note that the $N \to \infty$ limit of the theory is not equivalent to the classical theory of quarks and gluons (usually putting $1/\hbar \to \infty$ in the exponent of the Green's function), because the fields themselves are dependent on N. We now can read off the powers of N directly from the Lagrangian. Each vertex gives and every

color index loop gives a factor of N. Every propagator gives a power of $1/N$ (the propagator $\propto$ the inverse of the differential operator). Moreover, we can think of each double-line graph as a surface obtained by gluing polygons together at the double-lines. Since each line has an arrow on it, and double-lines have oppositely directed arrows, we can only construct orientable polygons in the theory. Let us now consider only diagrams with no external lines, thus every index must close to form a polygon. With this in mind, we calculate the powers of N in a diagram as follows:

$$N^{V-E+F} \equiv N^{\chi} \tag{3.9}$$

Here V is the number of vertices, E the number of edges, and F the number faces of the surface. We know that a two-dimensional oriented surface is topological equivalent to a sphere with some number of holes cut out of it and some number of handles stuck on it, represented by χ. The Euler character χ is by definition

$$\chi = 2 - 2h - b \tag{3.10}$$

where b and h denote the amount of holes (topological boundaries) and handles (or genus of a surface) respectively. This means that in the large-N limit, the maximum order of any diagram in the theory is $\mathcal{O}(N^2)$. This is when $h = 0$ and $b = 0$, the surface is equivalent to a sphere. Meaning in terms of polygons that we have planar diagrams, and hence non-planar diagrams ($h > 0$) are subleading. And, as we already have observed, $b > 0$ diagrams are subleading too, equivalently as the amount of internal quark loops creates boundaries in the geometric interpretation.

Up to this point, we have explained the mathematical idea of the 't Hooft limit and some of its implications. However, this does not mean that this limit correctly represents QCD, because QCD in the Standard Model is a SU(3) theory. It does, however, help to extend our understanding of the behaviour of the number of color degrees of freedom in QCD and the corresponding confinement phenomenon: the strong coupling of elementary particles at low energies (or large distances) has only color neutral states. A pure Yang-Mills theory can be seen as the full QCD case where the masses of the fermions are taken to be infinite, hence in this limit it is impossible for the quarks to propagate, and therefore they do not contribute in the dynamical sector of the theory. Thus, we have a theory with only propagating gauge fields, and from their interactions it is possible to create a spectrum of glueballs. Consider the SU(3) case with fermions, we have 3 colors, from which it is possible to make color neutral states or equivalently color singlets, by using 2 quarks with opposite color charge, a color and a anti-color, making up a meson. Similarly, we have 8 gluons which make up the color neutral glueballs consisting non-trivially of multiple gluons. In the large-N 't Hooft it works exactly the same, only the number of color degrees of freedom and number of gluons become large. Theoretically, glueballs are supposed to be present in QCD of the Standard Model. However, their mixing with bound quark states, such as mesons, can hide their contribution in the measured spectrum. In the next section, we will see that this mixing is suppressed in the large-N limit, and that it is most convenient to study pure Yang-Mills in the 't Hooft limit. And, as we already have seen, the large-N limit already makes the theory more manageable since a lot of diagrams become subleading. For completeness, note that 3 quarks can also form color-neutral states in QCD, which are called baryons. These particles pose a special problem in the $N \to \infty$ limit, because baryons must be made out of N quarks, while a normal meson is always made of 2 quarks, irrespective of N. In the large-N limit, baryons, therefore, behave in a different fashion compared to mesons (studied by E. Witten [10]).

3.2 Phenomenological implications of the large-N limit for mesons and glueballs

Under the assumption that the t'Hooft limit for QCD is a confining theory, this limit leads to a number of interesting phenomenological implications. For this discussion, we are going to use the functional integral in Minkowski space-time from section 2.1 and the rescaled Lagrangian, eq. (3.8). We write the denominator of the Green's functions, eq.(2.17), as

$$Z_0 = \int DA\ D\bar{\psi}\ D\psi\ \exp\left\{iN \int dt\ d^3x \tilde{\mathcal{L}}[A, \psi, \bar{\psi}]\right\} \tag{3.11}$$

where the subscript 0 denotes that no composite operators were added. If we now want to add composite operators to this expression we add a source term in the exponent of the form $NJ_a\mathcal{O}_a$ and take appropriate derivatives to obtain the n-point connected correlation function:

$$Z_J = \frac{1}{Z_0} \int DA\ D\bar{\psi}\ D\psi\ \exp\left\{iN \int dt\ d^3x \left(\tilde{\mathcal{L}}[A, \psi, \bar{\psi}] + J_a\mathcal{O}_a\right)\right\} \tag{3.12}$$

$$\langle \mathcal{O}_1(x_1) \cdots \mathcal{O}_n(x_n)\rangle = (iN)^{-1} \frac{\delta}{\delta J_1(x_1)} \cdots \frac{\delta}{\delta J_n(x_n)} \ln Z_J \bigg|_{J=0} \tag{3.13}$$

In the previous section we saw that the leading contribution in the 't Hooft limit is $\mathcal{O}(N^2)$ and as a consequence the n-point correlation function is dominated by planar gluon interactions which scale as $\mathcal{O}(N^{2-n})$. In the case of correlation functions involving quarks this is $\mathcal{O}(N^{1-n})$. Let $\mathcal{G}_i$ be a purely gluonic gauge invariant operator with the appropriate quantum numbers to describe a glueball. The two-point correlation function $\langle \mathcal{G}_i\mathcal{G}_i\rangle$, or propagation of the glueball, creates a glueball with an amplitude of $\mathcal{O}(1)$. The glueball-glueball interactions, such as scattering or decays, are described by higher-order connected correlations functions $\langle \mathcal{G}_i \cdots \mathcal{G}_n\rangle$ with $n \geq 3$. Because of the order calculation, this means that at least these interactions are suppressed by $\mathcal{O}(1/N)$, i.e. each additional glueball gives an order $1/N$ suppression. Similarly, meson states can be described by a gauge invariant operator $\mathcal{M}_i$ involving quark spinors with the appropriate quantum numbers. Now, $\langle \mathcal{M}_i\mathcal{M}_i\rangle$ scales to $1/N$ in the 't Hooft limit, and so $\sqrt{N}\mathcal{M}_i$ scales as $\mathcal{O}(1)$. Resulting in that the n-point correlation function $\langle \sqrt{N}\mathcal{M}_i \cdots \sqrt{N}\mathcal{M}_n\rangle$ now scales as $\mathcal{O}(N^{1-n/2})$, i.e. each additional meson gives a suppression of $1/\sqrt{N}$ as we take the existence of a meson to be equivalent to that of a glueball. We can also look at the order of the glueball-meson mixing $\langle \mathcal{G}_1 \cdots \mathcal{G}_n\sqrt{N}\mathcal{M}_1 \cdots \sqrt{N}\mathcal{M}_m\rangle$, which scales as order $\mathcal{O}(N^{2-n-m/2})$. This means that the glueball-meson interaction is at least $1/\sqrt{N}$ suppressed and vanishes in the 't Hooft limit. All in all we see that t'Hooft limit, a strongly interacting theory of quarks and gluons, has become a weakly interacting theory of stable hadrons (composite particles made of elementary QCD particles) from which it is convenient to study pure Yang-Mills theory. Moreover, exotic states like tetraquarks are absent in the 't Hooft limit because the leading order contributions to their propagators come from terms that correspond to the propagation of mesons.

3.3 Examples of mesonic behavior in large-N

In the 1960's, S. Okubo [11], G. Zweig [12] and J. Iizuka [13] found empirically that any strongly occurring process is suppressed if, through only the removal of internal gluon lines, its Feynman diagram can be separated into two disconnected diagrams: one containing all of the initial-state particles and one containing all of the final-state particles. Fig. 3.3 shows an example of this OZI rule: the two diagrams describe the propagation of a meson denoted by a

blob. In the diagram on the left, the quark/antiquark lines originating from the initial state, propagate to the final state, getting dressed by two internal gluons on the way, is proportional to $N\lambda^2$. The diagram on the right, which shows the same process through the annihilation of the initial quark and antiquark, an intermediate emission of two virtual gluons, and then the creation of a quark-antiquark pair that ends up in the final meson, is proportional to λ^2. This means that the right diagram is one power of N suppressed relative to the left diagram, so the large-N limit supports the OZI rule. In fact, the large-N expansion is the only known framework within QCD that provides an explanation for the OZI rule.

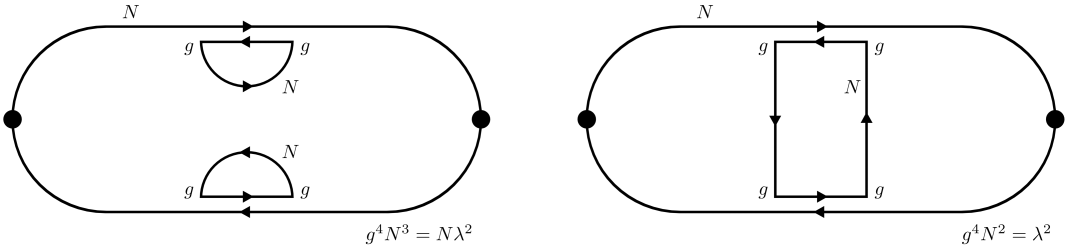

Figure 3.3: The large-N limit offers a simple interpretation for the OZI-rule: the figure shows an example of Feynman diagrams relevant for the propagation of a meson, where the diagram on the right is suppressed.

Another example is related to the global anomaly in the chiral symmetry of QCD. The chiral symmetry of the classical theory is not a symmetry of the quantum theory based on the same Lagrangian. We consider the three lightest quarks (up, down, and strange) and treat them as massless. The Dirac operator $i\gamma^\mu D_\mu$ anticommutes with the chirality operator γ_5. Therefore, if we write the independent rotations of the left- and right-handed components fields as $\psi_{R,L} = P_{R,L}\psi$ (where $P_{R,L} = \frac{I \pm \gamma_5}{2}$ and $\psi = \psi_L + \psi_R$), the Lagrangian is invariant under a global non-Abelian chiral symmetry $\mathrm{U}_R(3)\times\ \mathrm{U}_L(3)$. We write this effective Lagrangian, where left- and right-handed fields do not mix, i.e. no chirality changing interactions, as

$$\mathcal{L} = -\frac{1}{4}(F^a_{\mu\nu})^2 + i\bar{\psi}^j_R \not{D}\psi^j_R + i\bar{\psi}^j_L \not{D}\psi^j_L \tag{3.14}$$

where j indicates one of the considered quarks (color conservation is omitted, but is of course still there). However, the QCD vacuum has a non-vanishing vacuum expectation value for right-handed quarks interacting with left-handed quarks, $\langle\bar{\psi}_L\psi_R\rangle \neq 0$, implying we have spontaneous symmetry breaking $\mathrm{U}_R(3)\times\ \mathrm{U}_L(3) \to \mathrm{U}(3)_{\text{diagonal}}$. Goldstone's theorem says that if we spontaneously break one global symmetry down to another, we always obtain one massless boson particle per broken generator. This can be seen as rotations in the minimum of a Mexican-hat shaped potential. Accordingly, we should obtain $2n_f^2 - n_f^2 = 9$ meson particles: the three pions, the four kaons, and the two η particles. In reality, the quarks do have mass. Therefore, the Goldstone bosons (pseudoscalar mesons) pick up a light mass, becoming so-called pseudo-Goldstone bosons. Moreover, the original Lagrangian in the massless limit is invariant under multiple independent global symmetries

$$\psi \to e^{i\alpha}\psi, \quad \psi \to e^{i\beta\gamma_5}\psi, \quad \psi \to e^{i\gamma^a T^a}\psi, \quad \psi \to e^{i\delta^b\gamma_5 T^b}\psi \tag{3.15}$$

under which the left- and right-handed fields transforming the same way are called vector symmetries and under which they transform oppositely (i.e. different sign in the exponent)

are called chiral or axial symmetries (containing a γ_5). So, for example, $\mathrm{U}(1)_{\mathrm{axial}}$ (using $\gamma_5^2 = I$) transforms as:

$$\psi_L + \psi_R \to e^{i\beta\gamma_5}(\psi_L + \psi_R) = (I + i\beta\gamma_5)\left(\frac{I-\gamma_5}{2} + \frac{I+\gamma_5}{2}\right)\psi = e^{-i\beta}\psi_L + e^{i\beta}\psi_R \quad (3.16)$$

The global $\mathrm{U}_R(n_f)\times\ \mathrm{U}_L(nf)$ symmetry of the classical Lagrangian for the massless quarks can now be re-expressed in terms of vector (V) and axial (A) transformations as: $\mathrm{SU}(n_f)_V\times$ $\mathrm{U}(1)_V\times\ \mathrm{SU}(n_f)_A\times\ \mathrm{U}(1)_A$. The vector symmetries are approximately exact, but $\mathrm{SU}(n_f)_A$ is spontaneously broken. Correspondingly, $n_f^2 - 1$ pseudo-Goldstone bosons appear in the spectrum. In QCD, these pseudo-Goldstone bosons include pions, kaons, and the η particle (but not the η'). The fate of the $\mathrm{U}(1)_A$ symmetry is of particular interest since it is related to a problem: if the QCD vacuum is invariant under the symmetry it should give us a light hadron spectrum consisting of (nearly) mass-degenerate particles of opposite parity, which are not seen experimentally. If $\mathrm{U}(1)_A$ is spontaneously broken, we would get an η' particle, but this particle (with the right quantum numbers) is experimentally too heavy in comparison with the other particles. What we say is that the $\mathrm{U}(1)_A$ is explicitly broken at the quantum level but not at the classical level, an anomaly, due to the non-invariance of the measure (of the Green's functions) for the quark fields under $\mathrm{U}(1)_A$. This means that the conservation of the $\mathrm{U}(1)_A$ Noether current is violated at the quantum level, i.e $\partial_\alpha j_A^\alpha \neq 0$, which can be non-trivially written as

$$\partial_\alpha j_A^\alpha = -n_f q(x), \quad q(x) = \frac{g^2}{32\pi^2}\mathrm{tr}(\epsilon_{\mu\nu\sigma\rho}F^{\rho\sigma}F^{\mu\nu}) \quad (3.17)$$

where $q(x)$ is the topological charge density. This means that the anomaly is proportional to g^2 and is suppressed as $1/N$ in the 't Hooft limit. Therefore, we do not have the anomaly in the theory.

3.4 Glueball spectrum from a proposed solution to large-N Yang-Mills

M. Bochicchio [14] proposed a nonperturbative string solution for the glueball and meson spectrum of QCD in the large-N 't Hooft limit. He summarizes his findings for the glueball spectrum as follows:

$$\text{Open-String sector:} \quad m_{k,s}^2 = \big(k + \frac{s}{2}\big)\Lambda_{\mathrm{QCD}}^2, \quad \text{even } s, \quad k = 1, 2, \cdots \quad (3.18)$$

$$\text{Closed-String sector:} \quad m_{k,s}^2 = 2\big(k + \frac{s}{2}\big)\Lambda_{\mathrm{QCD}}^2, \quad \text{odd } s, \quad k = 1, 2, \cdots \quad (3.19)$$

k and s are the string quantum numbers labeling the states and the excitations respectively. Λ_{QCD} is the scale parameter, that in his scheme coincides, by definition, with the mass of the lightest glueball candidate ($k = 1$, $s = 0$ and open-string), phenomenologically identified with $f_0(1505\mathrm{MeV})$ [15]. Fig. 3.4 shows some of Bochicchio's predictions, denoted by back dots, together with possible experimental candidates, denoted by coloured dots. The blue and red lines denote the open- and closed-sting glueballs respectively, and for those lines the mass of the pseudo-Goldstone boson, an experimentally value, m_{PGB} is zero. This value is only relevant in the meson sector, presented by the green line. The $f_0(1505)$, $f_0(2100)$, and $f_2(2150)$ experimental candidates, lie very close to the theoretical large-N glueball values. Bochicchio's spectrum is very promising which supports a lattice study in the large-N limit to determine the glueball spectrum to be of interest.

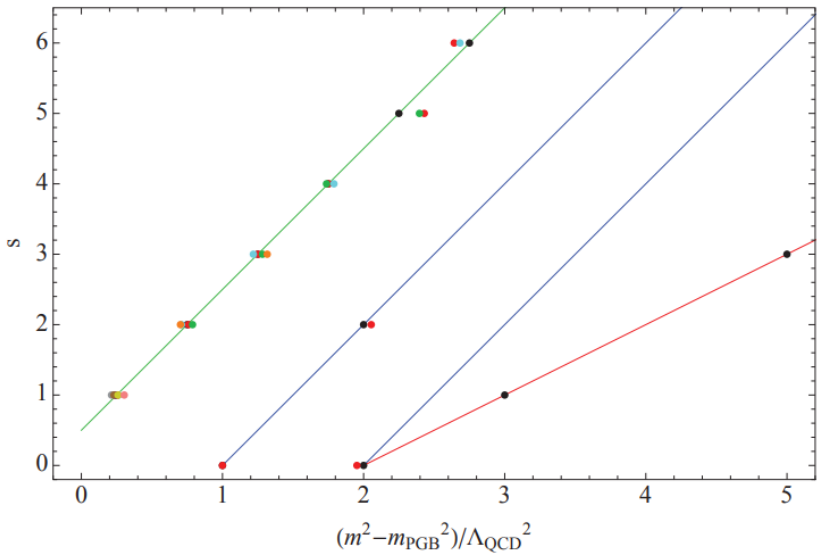

Figure 3.4: Glueball and meson spectrum (black dots and colored lines) together with experimental candidates (colored dots) as a function of the quantum number s from [14].

4 Glueball spectroscopy

We want to find the glueball masses using the Euclidean correlator, so according to what we discussed in chapter 2, we have to find glueball observables on the lattice. To do so, we need to relate the irreducible representations of the lattice in the continuum limit to irreducible representations of the discrete lattice. We have chosen to restrict ourselves to a finite lattice of size $N_s^3 \times N_t$ which obeys a cubic group symmetry. In section 4.1, we will look into how observables on the lattice translate to physical values. In section 4.2, we will study the cubic group using the book [16] of H.F. Jones. Thereafter, in section 4.3, we will use the paper [17] of B. Berg A. Billoire to study the construction of glueball observables on the lattice. In section 4.4, we will conclude with an example by giving the derivation of an observable to represent the scalar 0^{++} glueball state by use of spatial plaquettes.

4.1 β-function and physical scales

After our calculation of observables on the lattice, we have to translate the observables in terms of lattice units to an observable in physical units. First we are going see what happens to observables in the continuum limit. Thereafter, we translate numbers to dimensionfull physical values at a finite lattice spacing and in the continuum.

Suppose that we have found a mass in lattice units $\hat{m} = ma$. If we let $a \to 0$ we obtain the continuum limit. Then we would require that $\hat{m} \to 0$ because the mass m needs to remain finite. Equivalently, we can consider $\hat{m}$ in the statistical system as the inverse of a correlation length $\hat{\xi} = 1/\hat{m}$, as by definition $\langle \mathcal{O}(t)\mathcal{O}(0)\rangle \propto \exp(-t/\hat{\xi})$. Then in the continuum limit the correlation length diverges which is a sign of a phase transition or critical point of the statistical system. The relationship between the continuum limit and the critical points can be understood as follows. If we want our lattice results to be valid in the continuum limit, we require that the system loses its memory of the underlying lattice structure. The only parameter we have in the pure Yang-Mills lattice theory is the dimensionless coupling constant g in β_L. Therefore, g is the only parameter we can tune to reach the critical point of the theory, meaning that when $a \to 0$, we should have $g \to g_{\text{crit}}$ at the same time.

Using the β-function in the perturbative regime for the pure SU(N) Yang-Mills gauge theory (section 3.1), and considering the lattice spacing a as the inverse of the energy scale, we can write at two loops in perturbation theory:

$$-a\frac{dg}{da} = -\beta_0 g^3 - \beta_1 g^5 + \mathcal{O}(g^7) \quad \beta_0 = \frac{11N}{48\pi^2}, \quad \beta_1 = \frac{17N^2}{384\pi^4} \tag{4.1}$$

Solving only up to one-loop ($\mathcal{O}(g^3)$) yields

$$g^2 = -\frac{1}{\beta_0 \ln(a^2\Lambda_{\text{LAT}}^2)} \tag{4.2}$$

where Λ_{LAT} is the lattice scale integration constant. We can also solve for a up to two-loop ($\mathcal{O}(g^5)$) using the geometric series and considering g to be small:

$$\frac{1}{a}\frac{da}{dg} = \frac{1}{\beta_0 g^3 + \beta_1 g^5} = \frac{1}{\beta_0 g^3}\left(\frac{1}{1+\frac{\beta_1}{\beta_0}g^2}\right) = \frac{1}{\beta_0 g^3}\sum_n^\infty \left(-\frac{\beta_1}{\beta_0}g^2\right)^n \tag{4.3}$$

$$\Rightarrow a = \Lambda_{LAT}^{-1}\, e^{-\frac{1}{2\beta_0 g^2}}\, g^{-\frac{\beta_1}{\beta_0^2}}\left[1+\mathcal{O}(g^2)\right] \tag{4.4}$$

This function shows that $g_{\text{crit}} = 0$ if we want physical quantities to remain finite as $a \to 0$, which is precisely the asymptotic freedom we discussed in section 3.1. So, in the $\beta_L \to \infty$ limit every dimensionful parameter, such as mass, is measured in terms of the lattice scale parameter Λ_{LAT}. Moreover, to ensure we are extracting continuum physics, every observable should follow the exponential behavior in eq. (4.4), called asymptotic scaling, which means we are sufficiently close to $g = 0$.

There are multiple ways to set the physical scale, i.e. to determine a in physical units, but the most convenient way is to use the Sommer parameter [18]. The method is based on the force $F(r) = dV(r)/dr$ between two static quarks a distance r apart. For sufficiently heavy quarks, quark-antiquark bound states can be described by an effective nonrelativistic Schrödinger equation, and the force $F(r)$ can be studied. From comparing with experimental data for the bottom quarks ($\bar{b}b$) and charm quarks ($\bar{c}c$) spectra, it is found that:

$$F(r_0)\, r_0^2 = 1.65 \quad \text{with} \quad r_0 \equiv 0.5 \text{ fm} \tag{4.5}$$

It is well known how the QCD static quark potential can be parameterized, and the force becomes:

$$F(r) = \frac{d}{dr}V(r) = \frac{d}{dr}\left(A + \frac{B}{r} + \sigma r\right) = -\frac{B}{r^2} + \sigma \tag{4.6}$$

Since the force between the quarks is the derivative of $V(r)$, the constant A is only an irrelevant normalization of the energy. The second term is the Coulomb part (as in QED) with strength B. The third term is characteristic for QCD and indicates confinement: it is a linearly rising term with the real constant σ, called the string tension. Using eq. (4.5) and (4.6) we write

$$F(r_0)\, r_0^2 = -B + \sigma\, r_0^2 = 1.65 \tag{4.7}$$

which implies in terms of lattice units:

$$\frac{r_0}{a} = \sqrt{\frac{1.65 + B}{\sigma\, a^2}} \tag{4.8}$$

The static quark potential on the lattice can be calculated in multiple ways [19]. The most commonly used methods are the correlation of Polyakov loops at different spatial points m and n (with similar interpretation as in section 2.5), and the expectation values of Wilson loops at large times (both defined in section 2.4), with $r = a|m - n| = a\tilde{r}$:

$$\langle P_L(m) P_L^\dagger(n)\rangle \propto e^{-tV(r)}\big(1 + \mathcal{O}(e^{-t\Delta E})\big) \approx e^{-aN_t V(a\tilde{r})}, \quad \langle W_{\mathcal{L}}(\tilde{r}, n_t)\rangle \propto e^{-an_t V(a\tilde{r})} \tag{4.9}$$

The numbers B and σa^2 can be determined from a fit of these objects calculated for different $\tilde{r}$, since

$$aV(a\tilde{r}) = Aa + \frac{B}{\tilde{r}} + \sigma a^2 \tilde{r} \tag{4.10}$$

which in turn can be used to calculate the Sommer parameter r_0/a.

We summarize the determination of the lattice spacing as follows:

Step 1 Determine B and σa^2 and from the numerical data for $aV(an_s)$.

Step 2 Use eq. (4.8) to calculate the dimensionless number $X = r_0/a$.

Step 3 Then, the lattice spacing is given by $a = (0.5/X)$ fm $= 0.5/(hcX)$ MeV^{-1}, with $hc = 1239.8419$ MeV·fm.

If we now find the mass of a glueball in lattice units, we can find the mass in a physical unit: $m = \hat{m}/a$, at a finite lattice spacing. We can also use the Sommer parameter and eq. (4.4) to determine Λ_{LAT} (as we choose g in a lattice computation) and use this result to find the mass of the glueball in physical units in the continuum limit.

4.2 The symmetry group of the cube

Glueballs are (like any other particles) described quantum numbers J^{PC}, where J denotes the spin, P the parity, and C the charge parity. From the previous section, we know that, for the lattice theory, all physical masses are calculated in terms of the lattice spacing and become proportional to the lattice scale in the continuum limit:

$$m(J^{PC}) = c(J^{PC}) \times \Lambda_{LAT} \tag{4.11}$$

The problem we encounter in the rest of this chapter is one of spectroscopy: how to make observables on the lattice, which represent glueballs with appropriate quantum numbers, such that we can measure the dimensionless quantity $c(J^{PC})$ using the 2-point connected correlation function?

The lattice naturally respects the symmetry of the cubic group. The cubic group, denoted O, is part of the well-known crystal groups and contains discrete rotations along the symmetry axes (depicted in fig. 4.1). If a cube is rotated $\psi = 2\pi/n$ along an axis, this axis is called a n-fold rotation axis. The identity transformation ($n = 1$) is denoted by E, while other rotations are denoted by C_n. For example, two successive rotations are denoted as C_n^2. By inspecting the cube, we find the following possible rotations: E, $3C_{4i}$ $i \in \{x, y, z\}$, $4C_{3i}$ $i \in \{\alpha, \cdots, \delta\}$, and $6C_{2i}$ $i \in \{a, \cdots, f\}$, where the number in front denotes the number of rotation axes. So, in total we have $1 + 3 \cdot 3 + 4 \cdot 2 + 6 \cdot 1 = 24$ specific rotations, which are further divided in five different conjugacy (equivalence) classes. Two elements a and b of a group G are said to be equivalent if $b = gag^{-1}$, for another element $g \in G$. The cubic group can be divided in the following conjugacy classes

$$O: \quad E, \quad 6C_2, \quad 8C_3\ C_3^2, \quad 6C_4\ C_4^3, \quad 3C_4^2 \tag{4.12}$$

where the number in front denotes the number of elements in each class. So, for example, in the C_3 class a $2\pi/3$ counterclockwise rotation is equivalent to a clockwise rotation of $\pi/3$ over the α-axis (or the other way around), and since there are 4 similar axes of symmetry this conjugacy class contains 8 elements.

Group theory tells us the that for each conjugacy class, an irreducible representation of the group exists. This implies there are five irreducible representations of the cubic group. Furthermore, group theory dictates that the dimensions of these representations satisfy the following relation,

$$\sum_{\mu} n_\mu^2 = [G] \tag{4.13}$$

where $[G]$ is the order of the finite group G, i.e. 24, and n_μ is the dimension of each irreducible representation μ that we sum over. The only possible way to obey eq. (4.13) is for the dimensions to be 1, 1, 2, 3, 3. In the notation of crystallographic point groups, we denote the irreducible representations as A_1, A_2, E, T_1, and T_2 respectively. A is called the

trivial representation and T the vector representation. Each representation is fixed by its characters in the conjugate classes, as reproduced in table 4.1. The character of a conjugacy class is the trace of the matrices associated with the class elements in each representation, and is invariant for each representation. This table can be algebraically constructed using $\chi^{\mu}(E) = n_{\mu}$, where χ denotes the character, and the fact that the characters of irreducible representations act as a set of orthonormal basis vectors, i.e. $\sum k_i \chi_i^{(\mu)} \chi_i^{(\nu)\dagger}/[G] = \delta_{\mu\nu}$, where k_i denotes the number of elements in each conjugacy class.

	E	$6C_2$	$8C_3$	$6C_4$	$3C_4^2$
A_1	1	1	1	1	1
A_2	1	-1	1	-1	1
E	2	0	-1	0	2
T_1	3	-1	0	1	-1
T_1	3	1	0	-1	-1

Table 4.1: Character table for the irreducible representations of the cubic group O. The number in front of the symbol for the conjugate classes denotes the number of elements in its class.

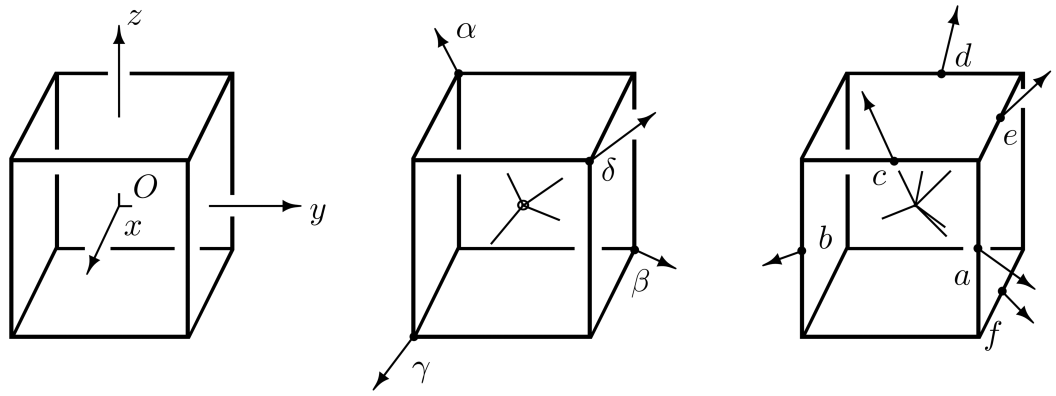

Figure 4.1: Rotations of the cubic group O.

In the next section the irreducible representations of O will be related to the quantum number J. Including parity is on top of these representations is straightforward. It can be achieved by adding reflections in the cubic point group by taking the direct product of O with $\mathcal{P}$. $\mathcal{P}$ is the group of order 2 containing the identity and the inversion with respect to the origin of the axes. Hence, the full group contains 10 conjugacy classes and therefore 10 irreducible representations. These irreducible representations are denoted $A_1^{\pm}$, $A_2^{\pm}$, $E^{\pm}$, $T_1^{\pm}$, and $T_2^{\pm}$, according to parity $P = \pm 1$. So, if the character of an irreducible representation obeys $\chi(O \times 1) = \chi(O \times -1)$, the $P = +1$ sign stands. Otherwise we have $\chi(O \times 1) = -\chi(O \times -1)$ and the $P = -1$ sign stands.

Charge parity can be added in similar fashion by reversing the orientation in the cubic point group (see section 4.4). So, in total this gives us 20 irreducible representations. We denote the irreducible representation as $\mathcal{R}^{PC}$, where $\mathcal{R} \in \{A_1, A_2, E, T_1, T_2\}$, $P \in \{+1, -1\}$ and $C \in \{+1, -1\}$.

4.3 Spin states and the cubic group

In the continuum limit of the lattice the rotational invariance must be restored, so glueball observables must be irreducible representations of SO(3) instead of the cubic group. Therefore, we need to know how the irreducible representations of SO(3) are decomposed in terms of O. We denote states which belong to an irreducible representation of spin J in SO(3) by

$$|\psi\rangle_J \quad (\beta_L = \infty) \tag{4.14}$$

where the spin is an integer number $J = 0, 1, \cdots$ (as glueballs are bosons). Each representation J has a degeneracy of $2J + 1$ or, in other words, a number of polarizations. For simplicity, we neglect parity and charge conjugation for the moment. All values of β_L have an exact cubic symmetry on the lattice. Therefore, a state (in a certain representation $\mathcal{R}$) can be represented on the lattice as:

$$|\psi\rangle_{\mathcal{R}} \tag{4.15}$$

In the continuum limit a state can be expanded into the states of spin J

$$|\psi\rangle_{\mathcal{R}} = \sum_J c_J^{\mathcal{R}} |\psi\rangle_J \tag{4.16}$$

where c is a constant. So, we have a linear combination of states $|\psi\rangle_J$ translated to $|\psi\rangle_{\mathcal{R}}$. If one embeds the cubic group into the rotation group, where the spin J of SO(3) is so-called subduced to O, one can translate a state the other way around and find a linear combination of states $|\psi\rangle_{\mathcal{R}}$ to represent a state $|\psi\rangle_J$. These subduced representations up to $J = 12$ are studied by S.L. Altmann & A.P. Cracknell [20], and are shown in table 4.2. For example, the spin 2 state of the continuum limit, which has 5 polarizations, splits into the direct sum of $E \oplus T_2$ in the cubic group.

	0	1	2	3	4	5	6	7	8	9	10	11	12
A_1	1	0	0	0	1	0	1	0	1	1	1	0	2
A_2	0	0	0	1	0	0	1	1	0	1	1	1	1
E	0	0	1	0	1	1	1	1	2	1	2	2	2
T_1	0	1	0	1	1	2	1	2	2	3	2	3	3
T_1	0	0	1	1	1	1	2	2	2	2	3	3	3

Table 4.2: Subduced representations of SO(3) to O up to $J = 12$. The top row is J while theleft column is $\mathcal{R}$. Given are the multiplicities with the representation $\mathcal{R}$ to decompose a state with spin J.

Now, a glueball observable with a spin J can be constructed if we find a pure gluonic gauge invariant observable on the lattice, which is equivalent to the right (combination of) irreducible representation(s) of the cubic group. In the next section, we will see that a sum of spatial plaquettes can for example form the irreducible representation A_1 on the lattice, which describes a $J = 0$ glueball.

4.4 Irreducible representations of the cubic group in terms of Wilson loops

From section 2.4 we know that the trace of a closed loop of link fields is gauge invariant: the Wilson loop. With respect to the cubic group, we consider such loops to be completely spatial.

For the following discussion, only the shape and orientation of the loops are important, and if we consider a loop to have a length L, we represent the Wilson loop by a L-tuple:

$$(\hat{f}_1, \cdots, \hat{f}_L) \quad \text{with} \quad \sum_i^L \hat{f}_i = 0 \tag{4.17}$$

Where $\hat{f}_i \in \{\pm\hat{e}_j | j = 1, 2, 3\}$, and $\hat{e}_j$ are unit vectors corresponding to the spatial coordinates of the lattice. The latter condition in eq. (4.17) just says that the path has to be closed. Two L-tuples are equivalent if they are identical up to a cyclic permutation. The equivalence class corresponding to $(\hat{f}_1, \cdots, \hat{f}_L)$ is denoted by $[\hat{f}_1, \cdots, \hat{f}_L]$. The parity operation simply reverts every link $\hat{f}_i$, because this is equivalent to an inversion with respect to the starting point

$$P[\hat{f}_1, \cdots, \hat{f}_L] = [-\hat{f}_1, \cdots, -\hat{f}_L] \tag{4.18}$$

and a path with defined parity $P = \pm$ can conventionally be written as a linear combination:

$$[\hat{f}_1, \cdots, \hat{f}_L]_\pm = \frac{1}{2}\big([\hat{f}_1, \cdots, \hat{f}_L] \pm [-\hat{f}_1, \cdots, -\hat{f}_L]\big) \tag{4.19}$$

A charge parity operation, represented by the Hermitian conjugate of the tuple, is equivalent to reversing the orientation of the links

$$C[\hat{f}_1, \cdots, \hat{f}_L] = [-\hat{f}_L, \cdots, -\hat{f}_1] \tag{4.20}$$

and a path with defined charge parity $C = \pm$ can conventionally be written as a linear combination:

$$[\hat{f}_1, \cdots, \hat{f}_L]_\pm = \frac{1}{2}\big([\hat{f}_1, \cdots, \hat{f}_L] \pm [-\hat{f}_L, \cdots, -\hat{f}_1]\big) \tag{4.21}$$

Note that a Wilson loop observable always gives us an imaginary number, since the link fields are elements of the SU(N) group. Therefore, determining the charge parity of a loop amounts to either taking the real ($C = +$) or imaginary ($C = -$) part of the trace of a link product (always constructed counter clockwise on a site n, as the plaquette in the lattice action, eq. (2.76)).

We aim to find Wilson loops which transform in the irreducible representations of O. To do so, we focus on the simplest case where we consider the three spatial plaquettes to have a length of 4 (fig. 4.2). We write these plaquettes mathematically as:

$$O_1 = [1, 2, -1, -2] \quad O_2 = [3, 1, -3, -1] \quad O_3 = [2, 3, -2, -3] \tag{4.22}$$

The plaquettes are P-invariant. Consider for example O_3:

$$\begin{aligned} P[2, 3, -2, -3]_\pm &= P\frac{1}{2}\big([2, 3, -2, -3] \pm [-2, -3, 2, 3]\big) \\ &= \frac{1}{2}\big([-2, -3, 2, 3] \pm [2, 3, -2, -3]\big) \\ &= \frac{1}{2}\big([2, 3, -2, -3] \pm [-2, -3, 2, 3]\big) = [2, 3, -2, -3]_\pm \end{aligned} \tag{4.23}$$

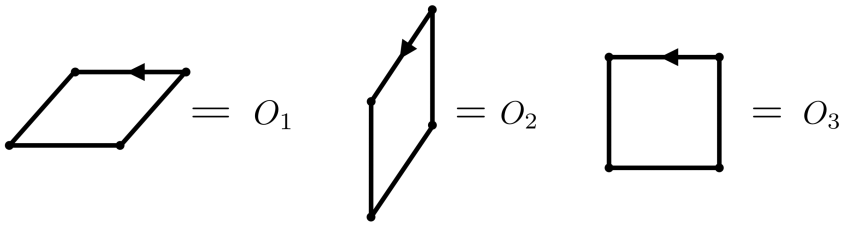

Figure 4.2: Spatial Wilson loops of length 4.

So, $P = +$ for observables constructed out of plaquettes. However, the plaquettes are not C-invariant. Consider for example O_3 again (as schematically shown in fig. 4.3):

$$\begin{aligned} C[2,3,-2,-3]_\pm &= C\frac{1}{2}\big([2,3,-2,-3] \pm [3,2,-3,-2]\big) \\ &= \frac{1}{2}\big([3,2,-3,-2] \pm [2,3,-2,-3]\big) \\ &= \begin{cases} \frac{1}{2}\big([2,3,-2,-3] + [3,2,-3,-2]\big) \\ -\frac{1}{2}\big([2,3,-2,-3] - [3,2,-3,-2]\big) \end{cases} \quad = \pm[2,3,-2,-3]_\pm \end{aligned} \tag{4.24}$$

So, $CO_{3\pm} = \pm O_{3\pm}$, and therefore it is of importance to take into account the charge parity of a plaquette if we want to work with a group element on it.

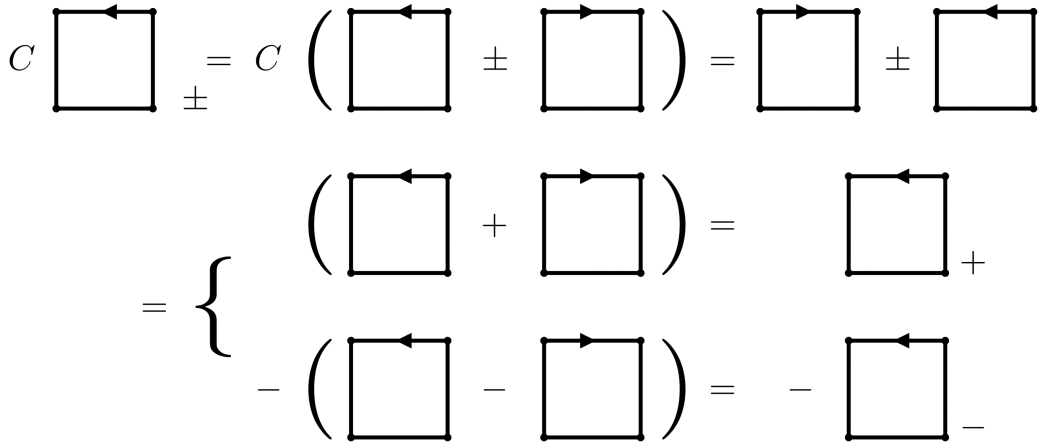

Figure 4.3: Charge parity on the $O_{3\pm}$ plaquette.

We now define how a given element of the symmetry group $g \in O$ acts on a L-tuple. Since the path $\mathcal{P}$ of an L-tuple is a collection of elementary spatial unit vectors, the operation of rotation on the path is defined by what the rotation does to each vector

$$\mathcal{M}_g(\mathcal{P}) = [\mathcal{R}(\hat{f}_1), \cdots, \mathcal{R}(\hat{f}_L)] \tag{4.25}$$

where $\mathcal{R}$ stands for a rotation of the O group in a three-dimensional representation, $\mathcal{M}$ denotes an arbitrary representation, and $\mathcal{P}$ denotes the path of the loop. We can take, for

example, a rotation $g = C_{4y}$ and study the behaviour of $O_{3\pm}$, depicted in fig. 4.3, as:

$$\mathcal{R}_{C_{4y}} = \begin{pmatrix} 0 & 0 & -1 \\ 0 & 1 & 0 \\ 1 & 0 & 0 \end{pmatrix} \tag{4.26}$$

$$\begin{aligned} \mathcal{M}_{C_{4y}}([2,3,-2,-3]_\pm) &= [\mathcal{R}_{C_{4y}}(\hat{2}), \cdots, \mathcal{R}_{C_{4y}}(-\hat{2})]_\pm \\ &= [2,-1,-2,1]_\pm = [1,2,-1,-2]_\pm = O_{1\pm} \end{aligned} \tag{4.27}$$

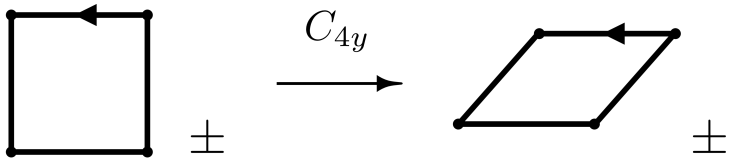

Figure 4.4: C_{4y} rotation on $O_{3\pm}$.

If we also compute how the other plaquettes transform, we can create a matrix $D_{\mathcal{M}}(C_{4y})$, which transforms directly the three considered plaquettes. The trace of this matrix gives the character of a conjugacy class in the representation $\mathcal{M}$. Performing one calculation for every class yields:

class E: $\mathrm{D}_{\mathcal{M}}(E)$:	$\mathrm{O}_{1\pm} \to O_{1\pm}$	$\mathrm{O}_{2\pm} \to O_{2\pm}$	$\mathrm{O}_{3\pm} \to O_{3\pm}$	$\Rightarrow \chi = 3$
class C_2: $\mathrm{D}_{\mathcal{M}}(C_{2a})$:	$\mathrm{O}_{1\pm} \to CO_{1\pm}$	$\mathrm{O}_{2\pm} \to O_{3\pm}$	$\mathrm{O}_{3\pm} \to O_{2\pm}$	$\Rightarrow \chi = C$
class C_3: $\mathrm{D}_{\mathcal{M}}(C_{3\alpha})$:	$\mathrm{O}_{1\pm} \to CO_{2\pm}$	$\mathrm{O}_{2\pm} \to O_{3\pm}$	$\mathrm{O}_{3\pm} \to CO_{1\pm}$	$\Rightarrow \chi = 0$
class C_4: $\mathrm{D}_{\mathcal{M}}(C_{4x})$:	$\mathrm{O}_{1\pm} \to O_{2\pm}$	$\mathrm{O}_{2\pm} \to CO_{1\pm}$	$\mathrm{O}_{3\pm} \to O_{3\pm}$	$\Rightarrow \chi = 1$
class C_4^2: $\mathrm{D}_{\mathcal{M}}(C_{2x})$:	$\mathrm{O}_{1\pm} \to CO_{1\pm}$	$\mathrm{O}_{2\pm} \to CO_{2\pm}$	$\mathrm{O}_{3\pm} \to O_{3\pm}$	$\Rightarrow \chi = 2C + 1$

With these characters we can decompose the representation $\mathcal{M}$ into the direct sum of irreducible representations O with multiplicity a_ν

$$a_\nu = \frac{1}{[G]} \sum k_i \chi_i^{(\nu)\dagger} \chi_i^{\mathcal{M}} \tag{4.28}$$

from which follows that $\mathcal{M}^{++} = A_1^{++} \oplus E^{++}$ and $\mathcal{M}^{+-} = T_1^{+-}$. However, we want to obtain the opposite: how an irreducible representation of O can be decomposed in the direct sum of the spatial plaquettes. In other words, we want to determine the orthonormal basis corresponding to each invariant subspace of the three-dimensional representation space. This basis will be formed by linear combinations of the spatial plaquettes. To accomplish this, we look for a basis in which each $D_{\mathcal{M}}(g)$ is of block-diagonal form for all g. This is the case when one finds the diagonalization of matrix C, which commutes with all $D_{\mathcal{M}}(g)$. We sum all the matrices of each class to obtain such a C matrix. When A is the matrix that simultaneously diagonalizes all C matrices, i.e. $A^{-1}CA = C_D$, we can read off directly the orthonormal basis of the invariant subspaces from the columns of the matrix A^{-1}. For $C = +$ we obtain:

$$C(E) = \begin{pmatrix} 1 & 0 & 0 \\ 0 & 1 & 0 \\ 0 & 0 & 1 \end{pmatrix}, C(C_2) = \begin{pmatrix} 2 & 2 & 2 \\ 2 & 2 & 2 \\ 2 & 2 & 2 \end{pmatrix} C(C_3) = \begin{pmatrix} 0 & 4 & 4 \\ 4 & 0 & 4 \\ 4 & 4 & 0 \end{pmatrix},$$

$$C(C_4) = \begin{pmatrix} 2 & 2 & 2 \\ 2 & 2 & 2 \\ 2 & 2 & 2 \end{pmatrix}, C(C_4^2) = \begin{pmatrix} 3 & 0 & 0 \\ 0 & 3 & 0 \\ 0 & 0 & 3 \end{pmatrix} \Rightarrow A^{-1} = \begin{pmatrix} 1 & -2 & 0 \\ 1 & 1 & 1 \\ 1 & 1 & -1 \end{pmatrix}$$

Since A_1 is one-dimensional and E is two-dimensional, the first column of A^{-1} is the decomposition of A_1 in terms of plaquettes, and the second and third column the decomposition of E. For $C = -$ we have that the three-dimensional representation $\mathcal{M}$ is an irreducible representation of O, the vector representation T_1, meaning that it has an eigenspace spanned by three plaquettes. Consequently, the C matrices are diagonals:

$$C(E) = \begin{pmatrix} 1 & 0 & 0 \\ 0 & 1 & 0 \\ 0 & 0 & 1 \end{pmatrix}, C(C_2) = \begin{pmatrix} -2 & 0 & 0 \\ 0 & -2 & 0 \\ 0 & 0 & -2 \end{pmatrix} C(C_3) = \begin{pmatrix} 0 & 0 & 0 \\ 0 & 0 & 0 \\ 0 & 0 & 0 \end{pmatrix},$$
$$C(C_4) = \begin{pmatrix} 2 & 0 & 0 \\ 0 & 2 & 0 \\ 0 & 0 & 2 \end{pmatrix}, C(C_4^2) = \begin{pmatrix} -1 & 0 & 0 \\ 0 & -1 & 0 \\ 0 & 0 & -1 \end{pmatrix} \Rightarrow A^{-1} = \begin{pmatrix} 1 & 0 & 0 \\ 0 & 1 & 0 \\ 0 & 0 & 1 \end{pmatrix}$$

We have summarized our findings in table 4.3. Note again that $P = +$ since the plaquettes are invariant under the parity transformation. Now, take the irreducible representation A_1^{++}. This representation is equal to the 0^{++} representation (from section 4.3), and is equal to the sum of the spacial plaquettes: $O_{1+} + O_{2+} + O_{3+}$, with positive charge parity. So, we found an observable on the lattice for the 0^{++} glueball: $\mathcal{O}(0^{++}) = \text{Re tr}(O_{xy} + O_{yz} + O_{xz})$. This is a scalar glueball, since it has 1 polarization. Note that the plaquettes can also be used to form other glueball observables.

Representation of O	Linear combination of plaquettes
A_1^{++}	$O_{1+} + O_{2+} + O_{3+}$
E^{++}	$-2O_{1+} + O_{2+} + O_{3+}$, $O_{2+} - O_{3+}$
T_1^{+-}	O_{1-}, O_{2-}, O_{3-}

Table 4.3: Linear combinations of plaquettes that form irreducible representations of the O group.

One can construct Wilson loops with all kinds of shapes and sizes such as double plaquettes, bent plaquettes and twisted plaquettes of length 6, of which examples are shown in fig. 4.5. These loops can also be related to irreducible representations of the cubic group to form all kinds of glueball observables, which is extensively studied in [17]. However, for the sake of simplicity we stick to the scalar 0^{++} glueball observable in this study.

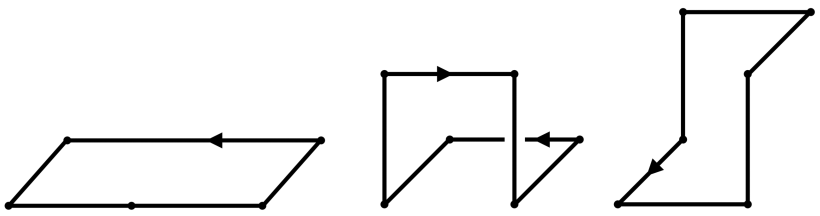

Figure 4.5: Examples of more complicated Wilson loops of length 6. These Wilson loops can be used to study glueball observables too. From left to right: double, bent and twisted plaquette.

5 Numerical simulation of the pure SU(N) Yang-Mills theory

In this chapter, we will explain how to simulate a pure SU(N) Yang-Mills theory on a Euclidean space-time lattice. Specifically, we will explain how to numerically calculate its correlation functions. First, in section 5.1, we will explain the Monte Carlo method for calculating the expectation value of an observable (such as the correlation function) by averaging over lattice configurations. We will update the lattice to new configurations using the Markov process, by which the lattice will find thermal equilibrium after a number of updates. The Markov process imposes some restrictions on how to update the lattice. The first Monte Carlo algorithm that obeys these restriction is the Metropolis algorithm, and is explained in section 5.2. Thereafter, in section 5.3, we will generate the $N \times N$ link matrices that need to be updated, and in section 5.4 we will discuss the boundary conditions and the start conditions for these gauge fields. In section 5.5, we will discuss the heat bath algorithm as an alternative to the Metropolis algorithm. In section 5.6, we will briefly discuss overrelaxation which speeds up the motion through configuration space to accelerate computations. In section 5.7, we will conclude with discussing two methods for improving the error estimation of expectation values, in view of the correlation function. This chapter is based on the book [6] of C. Gattringer & C.B. Lang.

5.1 The Monte Carlo method

As discussed in chapter 2, the vacuum expectation value of an observable, in the discretized Euclidean pure Yang-Mills field theory on a lattice, is given by the path integral formalism as

$$\langle \mathcal{O} \rangle_E = \frac{1}{Z} \int D[W]\, e^{-S_G[W]}\, \mathcal{O}[W] \quad \text{with} \quad Z = \int D[W]\, e^{-S_G[W]} \tag{5.1}$$

where $S_G[W]$ is the pure gauge action on the lattice, eq. (2.76), and $\mathcal{O}[W]$ the observable in terms of the links W. A Monte Carlo integration approximates eq. (5.1) by an average of the observable evaluated on N sample lattice configurations W_n, distributed with probability $\propto \exp(-S_G[W_n])$, where the sum is computed over sufficient configurations generated by Monte Carlo algorithms.

5.1.1 Importance sampling

From probability theory, we know that we can approximate an integral over a function by averaging the function values $f(x_n)$ at values x_n randomly chosen according to the uniform distribution $\rho_u(x_n) = 1/(b-a)$:

$$\frac{1}{b-a} \int_a^b dx\; f(x) = \langle f \rangle_{\rho_u} = \lim_{N\to\infty} \frac{1}{N} \sum_{n=1}^{N} f(x_n) \tag{5.2}$$

This method replaces the exact mean by the sample mean. This is useful as we are confined to finite samples in experiments. The error in the sample mean behaves like $\mathcal{O}(1/\sqrt{N})$, which is in itself a probabilistic statement since the error itself has a statistical error and so on. However, using the sample mean works well in actual calculations.

The Monte Carlo integration in eq. (5.2) is easily applicable to higher-dimensional integrals. All that changes is x_n, which denotes a vector of random variables, chosen in multi-dimensional space. Normally, the computational effort grows exponentially with the

requested accuracy if one would like to use the usual quadrature technique. However, for the Monte Carlo integration the estimated error is always $\propto 1/\sqrt{N}$. This implies that if we want to improve the accuracy of the integral by a factor of two, we have to take four times as many random points.

However, we also need to take into account the Boltzmann factor $\exp(-S)$, which, depending on the action, assigns a different weight to different configurations. When summing over configurations, it is more important to consider configurations with larger weights compared to configurations with smaller weights. This is known as importance sampling. In importance sampling Monte Carlo, we can approximate the huge sum of configurations by considering only a comparatively small subset, by sampling according to weight. The expectation value of some function $f(x)$ with regard to a probability distribution with density $\rho(x)$ is given by:

$$\langle f \rangle_\rho = \frac{\int_a^b dx\ \rho(x)\ f(x)}{\int_a^b dx\ \rho(x)} \tag{5.3}$$

As in eq. (5.2), the expectation value in the importance sampling Monte Carlo is approximated by an average over N values

$$\langle f \rangle_\rho = \lim_{N\to\infty} \frac{1}{N} \sum_{n=1}^{N} f(x_n) \tag{5.4}$$

for each $x_n \in (a, b)$ randomly sampled with the normalized probability density:

$$dP(x) = \frac{\rho(x)\ dx}{\int_a^b dx\ \rho(x)} \tag{5.5}$$

The functional integral, eq. (5.1), is of the form eq. (5.3) and thus suitable for importance sampling. For this reason, we omit the subscripts for the action, and write the expectation value of an observable $\mathcal{O}$ as:

$$\langle \mathcal{O} \rangle_\rho = \lim_{N\to\infty} \frac{1}{N} \sum_{n=1}^{N} \mathcal{O}[W_n] \tag{5.6}$$

Where each of the lattice configurations W_n is randomly sampled according to the probability density, named the Gibbs measure:

$$dP(W) = \frac{e^{-S[W]}\ D[W]}{\int D[W]\ e^{-S[W]}} \tag{5.7}$$

5.1.2 Markov Chains

The problem that arises now is how to find configurations W_n following the probability distribution of eq. (5.7). The idea is to start from an arbitrary configuration and construct a stochastic sequence of configurations that eventually finds an equilibrium distribution $P[W]$, which is called a homogeneous Markov chain or Markov process:

$$W_0 \longrightarrow W_1 \longrightarrow W_2 \longrightarrow \cdots \tag{5.8}$$

The configurations W_n are generated subsequently, where the index n labels the configurations in the order of the chain. The change to a new field configuration is called an update,

or a Monte Carlo step. In fig. 5.1 a schematic sketch of a Markov chain is shown, in which the boundary limits the space of all possible configurations.

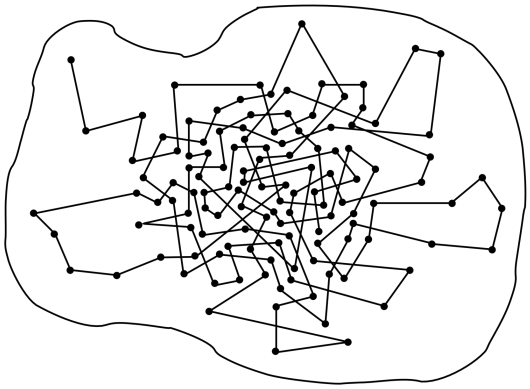

Figure 5.1: A schematic sketch of a Markov process in configuration space. The dots represent configurations that are visited subsequently represented by the connection between the dots. The Markov chain starts in the upper left corner and then quickly moves to the center of the space, where we find a large density of dots. The latter corresponds to a region of configurations with a large Boltzmann factor and thus with high probability, and the Markov chain is in such a way constructed that visits more often configurations with larger probability.

A Markov process is characterized by a conditional probability, i.e. the probability of going to W' starting from W:

$$P(W_n = W'|W_{n-1} = W) = T(W'|W) \tag{5.9}$$

This probability depends only on the configurations W' and W, but not on the index n. The transition probabilities obey trivially:

$$0 \leq T(W'|W) \leq 1, \quad \sum_{W'} T(W'|W) = 1 \tag{5.10}$$

Note that for the latter condition of eq. (5.10), the normalization sum also includes $W' = W$. Besides this, there is another important restriction on $T(W'|W)$. Once it is in equilibrium the Markov process cannot have sinks or sources of probability, meaning that the probability to go to another configuration W' at the step $W_{n-1} \to W_n$ has to be equal to the probability of going away from the configuration W'. The corresponding balance equation is written as follows:

$$\sum_{W} T(W'|W)\ P(W) \stackrel{!}{=} \sum_{W} T(W|W')\ P(W') \tag{5.11}$$

On the left-hand side, we sum over the transition probabilities leading to the final configuration W', weighted by the probability $P(W)$ that the system is actually in the configuration W. This gives the total probability to end up in configuration W', and has to be equal to move away from W', as computed in a similar manner on the right-hand side. Note that eq.

(5.11) also holds when $W' = W$, i.e. no transition. The sum on the right-hand side of eq. (5.11) can be evaluated using the normalization property, eq. (5.10), such that we find:

$$\sum_W T(W'|W)\ P(W) = P(W') \tag{5.12}$$

This shows that the equilibrium distribution $P(W)$ is a fixed point in the Markov process: once the distribution is obtained, the system stays there. Starting the process from an arbitrary configuration W_0 with an initial distribution P_0, we eventually obtain the equilibrium distribution by updating the configurations iteratively:

$$P_0 \longrightarrow P_1 \longrightarrow P_2 \longrightarrow \cdots \longrightarrow P(W) \tag{5.13}$$

To obtain a correct result for a Markov process, eq. (5.10) and (5.11) should be strictly obeyed. In an actual calculation, we only start to calculate the expectation of an observable, using eq. (5.6), after a certain number of Monte Carlo steps, as we want the lattice to have reached the equilbrium distribution. If the lattice is in equilibrium we say the lattice has thermalized. To decide when the lattice has thermalized is subtle and usually based on whether a certain observable has found its equilibrum distribution on the lattice.

If the balance equation, eq. (5.11), holds term-wise, we obtain the detailed balance equation, which is used in most Monte Carlo algorithms:

$$T(W'|W)\ P(W) = T(W|W')\ P(W') \tag{5.14}$$

In the next section, the detailed balance equation is used in the Metropolis algorithm.

5.2 The Metropolis algorithm

Metropolis et al. developed [21] an algorithm that uses the Markov process go from the configuration W_{n-1} to some new configuration W_n. Using $P(W) \propto \exp(-S[W])$ we summarize his algorithm in the following steps:

Step 1 Choose some candidate configuration W' according to some a priori selection probability $T_0(W'|W)$, where $W = W_{n-1}$.

Step 2 Accept the candidate configuration W' as the new configuration W_n with the acceptance probability:

$$T_A(W'|W) = \min\left(1,\ \frac{T_0(W|W')\ \exp(-S[W'])}{T_0(W'|W)\ \exp(-S[W])}\right) \tag{5.15}$$

If a suggested change is not accepted, the unchanged configuration is considered again in the Markov chain and included in the measurements like every configuration.

Step 3 Repeat the steps until the desired number of steps is completed.

As mentioned before, the total transition probability $T = T_0 T_A$ fulfills the detailed balance equation

$$\begin{aligned} T(W'|W)\ \exp(-S[W]) &= T_0(W'|W)\ \min\left(1,\ \frac{T_0(W|W')\ \exp(-S[W'])}{T_0(W'|W)\ \exp(-S[W])}\right)\ \exp(-S[W]) \\ &= \min(\ T_0(W'|W)\ \exp(-S[W]),\ T_0(W|W')\ \exp(-S[W'])) \\ &= T(W|W')\ \exp(-S[W']) \end{aligned} \tag{5.16}$$

due to the symmetry of the min operation. In many cases one uses a symmetric selection probability which obeys

$$T_0(W|W') = T_0(W'|W) \tag{5.17}$$

for which eq. (5.15) simplifies to:

$$T_A(W'|W) = \min(1,\ \exp(-\Delta S)) \quad \text{with} \quad \Delta S = S[W'] - S[W] \tag{5.18}$$

So, for a symmetric selection probability the information for deciding if a candidate configuration should be accepted or rejected depends only on the change in action.

We now apply the Metropolis algorithm to the SU(N) pure Yang-Mills lattice action, eq. (2.76). Starting from the configuration W, the candidate configuration W' for the Metropolis update differs from the configuration W by the value of a single link variable $W_\mu(n)$, so the change in action is local. In four dimensions, this link is shared with six plaquettes, and only these plaquettes are affected in the Metropolis step. Their local contribution to the action is

$$S[W_\mu(n)']_{\text{loc}} = \frac{\beta_L}{N}\sum_{i=1}^{6}\text{Re tr}(I - W_\mu(n)'\ P_i) = \frac{\beta_L}{N}\text{Re tr}(I - W_\mu(n)'\ A) \tag{5.19}$$

$$\text{with}\ \ A = \sum_{i=1}^{6} P_i = \sum_{\nu\neq\mu}\big(W_\nu(n+\hat{\mu})W_{-\mu}(n+\hat{\mu}+\hat{\nu})W_{-\nu}(n+\hat{\nu}) + W_{-\nu}(n+\hat{\mu})W_{-\mu}(n+\hat{\mu}-\hat{\nu})W_\nu(n-\hat{\nu})\big) \tag{5.20}$$

where P_i are products of the other three gauge link variables that make up one of the plaquettes with $W_\mu(n)'$, which are called staples. So, A is the sum over all staples. For the change in action, we write (A is not affected by the changing link):

$$\Delta S = S[W_\mu(n)']_{\text{loc}} - S[W_\mu(n)]_{\text{loc}} = -\frac{\beta_L}{N}\text{Re tr}[(W_\mu(n)' - W_\mu(n))A] \tag{5.21}$$

We need to come up with a candidate link $W_\mu(n)'$, such that the average acceptance probability, eq. (5.18), does not become too small. $W_\mu(n)'$ should therefore be an element of SU(N) that is not too far away from the old link. We use:

$$W_\mu(n)' = XW_\mu(n) \tag{5.22}$$

where X is a random element of the gauge group SU(N) in the neighborhood of I. How to construct these matrices is discussed in the next section. Note that for a symmetric selection probability, the change of choosing X should be equal to choosing X^{-1}.

We now create a recipe for the Metropolis algorithm for the pure Yang-Mills lattice single link variable update:

Step 1 Given some lattice configuration, take a site n and a direction μ together with a candidate $W_\mu(n)'$ according to eq. (5.22).

Step 2 Compute the sum of the staples A using eq. (5.20) and ΔS using eq. (5.21). If the action decreases or remains invariant ($\exp(-\Delta S) \geq 1$), the candidate is excepted. If the action increases ($\exp(-\Delta S) < 1$), compute a random number r (uniformly distributed in the [0, 1) interval) and accept the candidate if $r \leq \exp(-\Delta S)$, otherwise reject.

Step 3 Repeat the steps until the desired number of steps is performed.

Note that as long as the action remains invariant or decreases in the update scheme, the lattice will find its thermal equilibrium. If however the action increases in the updated scheme, then due to r, every now and then configurations with increased action are accepted. This could be seen as quantum fluctuations of the system.

The recipe we formulated is used for every link, and in such a way, we update the whole lattice to a new configuration. To eventually perform the Monte Carlo integration of a lattice observable, multiple configurations are saved. Note that the Metropolis algorithm is easily applicable to other (improved) actions, such as eq. (2.77). Since the computation of the sum of the staples A is computationally costly, we can iteratively offer multiple candidates to the algorithm which are then accepted or rejected according to step 2, before going to the next link. This modification is known as the multihit Metropolis algorithm, and the number of candidates can be tuned for efficiency. In section 5.5, we will discuss the heat bath algorithm, which essentially is an infinite repetition of the multihit Metropolis algorithm for every link, optimizing the local acceptance rate.

5.3 Generating candidate links

On every link lives a matrix to represent a gluon field, and in this section we are going to construct these complex SU(N) matrices that have size of $N \times N$.

Let us first consider how to construct a random SU(2) matrix. A SU(2) matrix has the following shape, taking into account complex entries and group obligations

$$W = \begin{pmatrix} a & b \\ -b^* & a^* \end{pmatrix} \quad \text{with} \quad |a|^2 + |b|^2 = 1 \tag{5.23}$$

with $a = x_0 + ix_1$ and $b = x_3 + ix_2$. This is equivalent to using the vector $x = (x_0, \vec{x})$ of four real coefficients in the following

$$W = x_0 I + i\vec{x} \cdot \vec{\sigma} \quad \text{with} \quad \det(W) = |x|^2 = x_0^2 + |\vec{x}|^2 = \sum_{i=0}^{3} x_i^2 = 1 \tag{5.24}$$

where $\vec{\sigma}$ denotes the vector of the three Pauli matrices:

$$\sigma_1 = \begin{pmatrix} 0 & 1 \\ 1 & 0 \end{pmatrix}, \quad \sigma_2 = \begin{pmatrix} 0 & -i \\ i & 0 \end{pmatrix}, \quad \sigma_3 = \begin{pmatrix} 1 & 0 \\ 0 & -1 \end{pmatrix} \tag{5.25}$$

We now generate a random number for x_0 uniformly distributed in [0,1) to calculate $|\vec{x}|$. The remaining x's form a uniform spherical distribution, so by also generating $\cos\theta \in [-1, 1]$ and $\phi \in [0, 2\pi)$ uniformly, we find:

$$x_1 = |\vec{x}| \sin\theta \cos\phi \tag{5.26}$$
$$x_2 = |\vec{x}| \sin\theta \sin\phi \tag{5.27}$$
$$x_3 = |\vec{x}| \cos\theta \tag{5.28}$$

Which can be used in eq. (5.24) to construct a matrix. However, according to eq (5.22) we need a randomly chosen element X (of the gauge group, close to the unit element) for the Metropolis algorithm. Although various methods exist for constructing such a matrix, we

have chosen to compute four random numbers uniformly distributed in $(-1/2, 1/2)$, and the SU(2) matrix is then again constructed following eq. (5.24) with x_0 and $\vec{x}$ given by

$$\vec{x} = \epsilon \frac{\vec{r}}{|\vec{r}|}, \quad x_0 = \text{sign}(r_0)\sqrt{1-\epsilon^2} \tag{5.29}$$

where ϵ is the parameter that controls the spread of X around the identity I. Note that we have to preserve the symmetry of the selection probability $T_0(W'|W)$, so X and $X^{-1} = X^\dagger$ should be chosen with equal probability. To do so, we construct a set of, say 1000, random matrices around unity and include in this set the Hermitian conjugate of each matrix before doing Monte Carlo updates. Then the matrices X to build candidate links are chosen randomly out of the set.

For larger SU(N) matrices, the complexity for generating matrices rises quickly since the minimum number of parameters of such a matrix is equal to the number of generators of the group. However, if we are able to construct SU(2) matrices, we can use a trick by multiplying N embedded SU(2) subgroup matrices to construct a SU(N) matrix. For example, a SU(3) matrix can be made using

$$R = \begin{pmatrix} r_{11} & r_{12} & 0 \\ r_{21} & r_{22} & 0 \\ 0 & 0 & 1 \end{pmatrix}, \quad S = \begin{pmatrix} s_{11} & 0 & s_{12} \\ 0 & 1 & 0 \\ s_{21} & 0 & s_{22} \end{pmatrix}, \quad T = \begin{pmatrix} 1 & 0 & 0 \\ 0 & t_{11} & t_{12} \\ 0 & t_{21} & t_{22} \end{pmatrix} \tag{5.30}$$

where a possible choice for the SU(3) matrix is given by the product:

$$W = RST \tag{5.31}$$

This method allows us to easily construct matrices of every SU(N) theory, and can be used for both random links and for updating matrices X.

In an actual computation, the matrices have to be projected to unitarity regularly because there will be an accumulation of rounding errors in the multiplication of group elements. Multiplication of unitary matrices should give a unitary matrix. The period depends on the number of digits chosen, and has to be decided based on observation. The process of re-unitarization for SU(2) is as follows: normalize the first row, and then reconstruct the second row from the first, as in eq. (5.23). For SU(3) and larger, we follow the well-known Gram-Schmidt procedure for building orthonormal basis elements in vector spaces. The first row is normalized, the second row is constructed from the current values orthogonalized to the first row, and the third row is orthogonalized to the first and second row and so on:

$$\begin{aligned} &\vec{u_1} = \vec{v_1}/|\vec{v_1}| \\ &\vec{u_n} = \vec{v_n}'/|\vec{v_n}'| \quad \text{where} \quad \vec{v_n}' = \vec{v_n} - \sum_{j=1}^{n-1} \vec{u_n}\,(\vec{v_n} \cdot \vec{u_n^*}) \quad \text{for} \quad n \geq 2 \end{aligned} \tag{5.32}$$

Here u_n and v_n respectively denote the new row and the old row. Although we now obtain a unitary matrix, due to the procedure the determinant is not necessarily equal to one anymore. To solve this, we multiply the last row with a phase p, i.e. $\det(W) = a + ib \neq 1 \Rightarrow \theta = \tan^{-1}(b/a)$ so that $p = \exp(i\theta)$. For SU(3) we can avoid this by constructing the third row taking the complex cross product $\vec{u_1}^* \times \vec{u_2}^*$.

5.4 Boundary and start conditions

Since we are developing a numerical simulation on a finite lattice, we have to implement boundary conditions. We have naturally chosen periodic boundary conditions for the gauge

fields, where N_s and N_t are the number of sites in the spatial and temporal directions, respectively:

$$W_\mu(N_s, n_y, n_z, n_t) = W_\mu(0, n_y, n_z, n_t), \quad W_\mu(n_x, N_s, n_z, n_t) = W_\mu(n_x, 0, n_z, n_t)$$
$$W_\mu(n_x, n_y, N_s, n_t) = W_\mu(n_x, n_y, 0, n_t), \quad W_\mu(n_x, n_y, n_z, N_t) = W_\mu(n_x, n_y, n_z, 0)$$

The boundary conditions correspond to the underlying manifold, in this case a torus in four dimensions: each direction of the hypercube behaves like a circle. This has as the advantage of preserving the translational symmetry of the discrete lattice.

We need to choose an initial configuration for the lattice links before we start the update algorithm. We know that it does not matter where the initial start of the Markov chain is: after a sufficient number of updates the lattice reaches thermal equilibrium. Two typical starting configurations are the hot and cold start:

Hot start The gauge field configurations are chosen randomly in group space.

Cold start All links are set to unity. In this case, the gauge action is minimal, which is approximately expected for weak coupling (large β_L). In statistical models this regime corresponds to low temperatures, hence the name.

Although we can use either starting configuration (or even a combination) for the Monte Carlo calculation, we should keep in mind that we first have to thermalize the lattice before computing expectation values.

5.5 The heat bath algorithm

The heat bath algorithm combines step 1 and 2 of the single link Metropolis update into a single-step, choosing the new link value $W_\mu(n)'$ according to the local probability distribution using the surrounding staples:

$$dP(W) = dW \exp\left(\frac{\beta_L}{N}\text{Re tr}[WA]\right) \tag{5.33}$$

Note that dW denotes the Haar integration measure. In this algorithm the link variable always changes as an advantage.

We first present the heat bath method for SU(2), based on the paper by M. Creutz [22]. The method for SU(2) can later be exteded to SU(N). The SU(2) group is special since the sum of two SU(2) matrices is proportional to another SU(2) matrix. Using this property we write the sum of the staples A as

$$A = aV \quad \text{with} \quad a = \sqrt{\det(A)} \tag{5.34}$$

where it is expected that $\det(A) \geq 0$. If for any reason $\det(A)$ still vanishes we choose a random SU(2) matrix for the new link. Otherwise the matrix $V = A/a$ is a properly normalized SU(2) matrix, and we use the heat bath algorithm to generate a new link. Inserting eq. (5.34) in eq. (5.33), and setting N = 2, we obtain:

$$dP(W) = dW \exp\left(\frac{1}{2}a\beta_L\text{Re tr}[WV]\right) \tag{5.35}$$

The Haar measure, as we have seen in section 2.3, may also be written as $d(WV)$. We define $X = WV$, and write the local probability distribution for X as:

$$dP(X) = dX \, \exp\left(\frac{1}{2} a\beta_L \mathrm{Re} \, \mathrm{tr}[X]\right) \tag{5.36}$$

If we now generate a matrix X according to this distribution the candidate link is obtained by:

$$W_\mu(n)' = W = XV^\dagger \tag{5.37}$$

We have reduced the problem of generating matrices X according to the distribution eq. (5.36). As in eq. (5.24), we write the Haar measure in terms of real parameters

$$\begin{aligned} dX &= \frac{1}{\pi^2} d^4x \; \delta(x_0^2 + |\vec{x}|^2 - 1) \\ &= \frac{1}{\pi^2} d^4x \frac{\theta(1-x_0^2)}{2\sqrt{1-x_0^2}} \left(\delta(|\vec{x}| - \sqrt{1-x_0^2}) + \delta(|\vec{x}| + \sqrt{1-x_0^2}) \right) \end{aligned} \tag{5.38}$$

where in the second line, a well-known formula for the Dirac delta function was used. We write the volume element as

$$d^4x = d|\vec{x}| \; |\vec{x}|^2 \; d^2\Omega \; dx_0 \tag{5.39}$$

where $d^2\Omega$ denotes the spherical angle element in the integration of the 3-vector $\vec{x}$. Only the first Dirac delta of eq. (5.38) contributes and $|\vec{x}|$ is frozen to $\sqrt{1-x_0^2}$, so the $\vec{x}$ integration is removed:

$$dX = \frac{1}{\pi^2} d^2\Omega \; dx_0 \frac{(1-x_0^2) \; \theta(1-x_0^2)}{2\sqrt{1-x_0^2}} = \frac{1}{2\pi^2} d^2\Omega \; dx_0 \sqrt{1-x_0^2} \;\; \theta(1-x_0^2) \tag{5.40}$$

Note that a matrix X has $|x_0| \leq 1$, so we omit the step function θ. Now, since the $\mathrm{tr}[X] = 2x_0$, eq. (5.24), and using $d^2\Omega = d\cos\theta \; d\phi$ in spherical coordinates, we write the distribution of X as

$$dP(X) = \frac{1}{2\pi^2} d\cos\theta \; d\phi \; dx_0 \sqrt{1-x_0^2} \; e^{a\beta_L x_0} \tag{5.41}$$

with $x_0 \in [-1, 1]$, $\cos\theta \in [-1, 1]$ and $\phi \in [0, 2\pi)$. To find the matrix X, we need to find the variables x_0, θ and ϕ distributed according to eq. (5.41). The latter two are just uniformly distributed and are used to calculate the $\vec{x}$ using eq. (5.26), (5.27), and (5.28), if we have x_0, since $|\vec{x}| = \sqrt{1-x_0^2}$. The problem now resides to finding the random variable x_0 distributed according to $\sqrt{1-x_0^2} \; e^{a\beta_L x_0}$. M. Creutz proposes in his paper [22] an algorithm for this, however, A.D. Kennedy and B.J. Pendleton found [23] a better algorithm which we use and present here. First, introduce a variable λ as:

$$\begin{aligned} & x_0 = 1 - 2\lambda^2 \quad \text{with} \quad x_0 \in [-1, 1] \\ & \Rightarrow dx_0 \sqrt{1-x_0^2} \; e^{a\beta_L x_0} \propto d\lambda \; \lambda^2 \sqrt{1-\lambda^2} \; e^{-2a\beta_L \lambda^2} \end{aligned} \tag{5.42}$$

After this transformation, we need to generate λ with the modified Gaussian distribution density

$$p_1(\lambda) = \lambda^2 e^{-2a\beta_L \lambda^2} \tag{5.43}$$

and accept or reject it using the square root function:

$$p_2(\lambda) = \sqrt{1-\lambda^2} \tag{5.44}$$

This works as follows:

Step 1 Generate three random numbers $r_i, i = 1, 2, 3$ uniformly distributed in (0,1]. Then

$$\lambda^2 = -\frac{1}{2a\beta_L}\big(\ln(r_1 + \cos^2(2\pi r_2)\,\ln(r_3)\big) \tag{5.45}$$

follows the required Gaussian distribution $p_1(\lambda^2)$.

Step 2 We need to correct for the factor $p_2(\lambda)$ and thus only accept values of λ which obey

$$r \leq \sqrt{1-\lambda^2} \quad \Rightarrow \quad r^2 \leq 1-\lambda^2 \tag{5.46}$$

where r is an random variable uniformly disrtributed in [0,1), and the accepted value gives $x_0 = 1-\lambda^2$ following the requested distribution.

So, we are now able to compute the x's, which in their turn, are used to compute the matrix X using eq. (5.24). In summary, we update a SU(2) link variable in the heat bath algorithm as follows:

Step 1 Find the sum of the staples A using eq. (5.20), compute $a = \sqrt{\det(A)}$ and find $V = A/a$.

Step 2 Find a group element X according to distribution eq. (5.41) as we discussed above.

Step 3 The new link variable is $W = XV^\dagger$.

Unfortunately, there is no heat bath algorithm that directly produces SU(3) or higher N link variables. However, N. Cabbibo and E. Marinari found [24] a pseudo heat bath method by iterating the heat bath method for the SU(2) subgroups of SU(N). Two subgroups would be sufficient to cover the whole group space, but for symmetry reasons one normally chooses three such subgroups as in eq. (5.31). Each of the submatrices is determined accordingly using the heat bath algorithm for SU(2). To illustrate this, we modify the SU(3) link variable W by left multiplication of R, and the exponent of eq. (5.33) now becomes:

$$\frac{\beta_L}{3}\mathrm{Re\ tr}[RWA] \tag{5.47}$$

Taking $U = WA$ the trace contains the terms:

$$\mathrm{tr}[RU] = r_{11}u_{11} + r_{12}u_{21} + r_{21}u_{12} + r_{22}u_{22} + \text{terms without } r_{ij} \tag{5.48}$$

A heat bath algorithm for R is therefore only influenced by those terms in U that multiply the four nontrivial terms in R, i.e. the sub-block of U corresponding to the relevant submatrix of R. We find that the role of A in eq. (5.33) is replaced by the relevant submatrix U, and we use the heat bath algorithm to find R with $\beta_L \to \beta_L/3$. We subsequently multiply R with U to obtain a new $U = RWA$, which provides the heat bath factors for S. And multiplying S with U once more gives the heat bath factors for T, such that the three heath bath matrices give the new value of the link variable:

$$W \Rightarrow W' = TSRW \tag{5.49}$$

5.6 Overrelaxation

S. L. Adler introduced [25] a stochastic overrelaxation algorithm for multi-quadratic actions. The overrelaxation algorithm changes a candidate variable by going beyond the minimum of the local action, depending on $\omega \in [1, 2]$. The algorithm speeds up the motion through configuration space as it reflects the candidate (W) with respect to the minimum action to a new candidate (W') which has the same probability as the old candidate (W). Therefore, the new candidate is changed (a lot) and automatically accepted in the Monte Carlo update algorithm.

According to F.R. Brown and T.J. Woch [26], the solution for SU(2) links is especially simple if one takes $\omega = 2$. This changes the link as follows:

$$W \Rightarrow W' = V^\dagger W^\dagger V^\dagger \tag{5.50}$$

with a gauge group element V such that the action is invariant. For V, we choose again the normalized sum of the staples, and we find that the action is indeed invariant:

$$\mathrm{tr}[W'A] = \mathrm{tr}[V^\dagger W^\dagger V^\dagger A] = a\ \mathrm{tr}[V^\dagger W^\dagger] = \mathrm{tr}[A^\dagger W^\dagger] = \mathrm{tr}[WA] \tag{5.51}$$

Note also that the selection probability T_0 is symmetric, since $W' = V^\dagger W^\dagger V^\dagger$ implies $W = V^\dagger W'^\dagger V^\dagger$. And again, in the rare case that $\det(A)$ vanishes, any random link variable is used and accepted.

An implementation for larger N gauge groups is again more difficult and therefore one usually preforms overrelaxation on the SU(2) subgroups. Interestingly, P. de Forcrand suggested [27] such an overrelaxation over the whole SU(N) group using the Metropolis algorithm. Note that overrelaxation alone is not ergodic: it only samples the configuration space of constant action (the microcanonical ensemble). However, since we want to determine configurations according to the canonical ensemble, i.e. distributed according to the Boltzmann weight, we have to implement the overrelaxation steps on top of the Metropolis or heat bath algorithm.

5.7 Resampling techniques

It is often very expensive to compute expectation values in Monte Carlo calculations. On top of this, the number of measurements can be too small to obtain a reliable estimate for the variance of the computed expectation values. In this section, we present two efficient and simple statistical methods dealing with this. Both assume that the data is not correlated.

Bootstrap Assume that we are interested in some observable θ which is estimated from a set of N measurements. We name the value obtained from the original data set, by eq. (5.6), $\hat{\theta}$. We repeatedly create new samples from the original sample by randomly choosing data from the original set. We can essentially do this for free as we just recycle the original data set for building of new sets. We do this K times and thus obtain K sets of N data. Note that values can end up in the new samples more than once. For each of these sets we compute θ_k accordingly, with $k = 1, \cdots, K$. Then, we compute estimators for $\langle\theta\rangle$ and $\sigma^2_{\hat{\theta}}$ as:

$$\tilde{\theta} = \frac{1}{K}\sum_{k=1}^{K}\theta_k, \quad \sigma^2_{\tilde{\theta}} = \frac{1}{K}\sum_{k=1}^{K}\left(\theta_k - \tilde{\theta}\right)^2 \tag{5.52}$$

The difference between $\tilde{\theta}$ and $\hat{\theta}$ is called bias, which is a measure for how far the result is from $\langle\theta\rangle$. As a final result we set $\langle\theta\rangle = \tilde{\theta} \pm \sigma_{\tilde{\theta}}$.

Jackknife This method is similar to bootstrap, but we construct N subsets by removing the n^{th} entry of the original set ($n = 1, \cdots, N$) and determine, again, the value θ_n for each of these sets accordingly. So:

$$\tilde{\theta} = \frac{1}{N}\sum_{n=1}^{N}\theta_n, \quad \sigma_{\hat{\theta}}^2 = \frac{N-1}{N}\sum_{n=1}^{N}\left(\theta_n - \hat{\theta}\right)^2 \tag{5.53}$$

The bias is determined from $\hat{\theta} - (N-1)(\tilde{\theta} - \hat{\theta})$. For the final result we set again $\langle\theta\rangle = \tilde{\theta} \pm \sigma_{\hat{\theta}}$.

In subsection 6.4.1, we will compute the 2-point connected correlation function using the Monte Carlo integration by averaging correlators from many configurations. However, for determining a reliable error for the correlator, we will still need more configurations. So, we have chosen to use the jackknife procedure for these computations.

6 Measurements with our own lattice implementation

In chapter 5, we have seen how we can construct our own Monte Carlo lattice simulations. In this chapter, results from these Monte Carlo lattice simulations are discussed. In section 6.1, we will perform some calculations to show what the implementation of the lattice produces in first instance. Furthermore, we will find that the scalar 0^{++} glueball 2-point correlation function has relatively large errors in the regime we want to fit, hence we cannot properly calculate the mass of the glueball. We therefore need error reduction algorithms, which will be explained in section 6.2. In section 6.3, we will show results for the 0^{++} glueball correlator with noise reduction algorithms. In section 6.4, we conclude with a computation of the Sommer parameter and try to set the physical scale in our computations.

6.1 A first computation

A first computation can tell us about the performance of the lattice simulation. In subsection 6.1.1, we will look at differences between the Metropolis and heat bath algorithm, using the average plaquette and average Wilson loop expectation values, and see which algorithm performs best. Thereafter, in subsection 6.1.2, we will briefly compare our results with Creutz's results [22]. In subsection 6.1.3, we will look at the error of observables. We discuss where these errors come from, and what reduces these errors. Finally, in subsection 6.1.4 we will compute the 2-point connected correlation function on the lattice using the scalar 0^{++} glueball observable from section 4.4.

6.1.1 Comparison of results with Metropolis and heat bath algorithms

For every lattice configuration we calculate the average plaquette as

$$S_\square = 1 - \overline{W}(\square) \quad \text{with} \quad \overline{W}(\square) = \frac{1}{n_{\text{sites}}} \frac{1}{6} \frac{1}{N} \sum_{n_{\text{sites}},\ \mu>\nu} \text{Re tr}[W_{\mu\nu}], \quad n_{\text{sites}} = N_s^3 \times N_t \tag{6.1}$$

where $\overline{W}(\square)$ denotes the average Wilson loop, and for every lattice point there are 6 plaquettes $W_{\mu\nu}$ we have to average over. We can easily extend eq. (6.1) to square $a \times a$ Wilson loops, and we define the general average Wilson loop as:

$$\overline{W}(\square, a) = \frac{1}{n_{\text{sites}}} \frac{1}{6} \frac{1}{N} \sum_{n_{\text{sites}},\ \mu>\nu} \text{Re tr}[W_{\mu\nu}(a \times a)] \tag{6.2}$$

These values can be calculated because the loops are gauge invariant, and these are simplest observables we can compute on the lattice. These observables are useful for determining whether the lattice has reached thermal equilibrium.

If the lattice has reached thermal equilibrium, we use eq. (5.6) to calculate the expectation value of an observable with standard deviation $\sigma_{\mathcal{O}}$, as

$$\langle \mathcal{O} \rangle = \frac{1}{N_{cf}} \sum_{n=1}^{N_{cf}} \mathcal{O}_n, \quad \sigma_{\mathcal{O}}^2 = \frac{1}{N_{cf} - 1} \sum_{n=1}^{N_{cf}} \Big(\mathcal{O}_n - \langle \mathcal{O} \rangle \Big)^2 \tag{6.3}$$

where N_{cf} denotes the number of measurements (the number of saved lattice configurations), which should be taken to be large. Because the lattice configurations are expected to be highly correlated, we perform N_{cor} lattice updates between measurements. However, if we take $N_{\text{cor}} = 0$, as for example in fig. 6.2, we can clearly observe the convergence of the average plaquette to the equilibrium distribution as a function of updated lattices. In this

figure we show both the Metropolis and heat bath algorithm for a SU(3) lattice with size $4^3 \times 8$, $N_{\text{cf}} = 300$, a cold start, and $\beta_L = 5.5$. In the case of the Metropolis algorithm (see section 5.3), we generated 500 matrices (and their inverses) with $\epsilon = 0.24$. If ϵ is too small, it takes a long time for the lattice to reach thermal equilibrium. If however ϵ is too large, we obtain larger errors as the randomly accepted link matrices $(W_\mu(n)')$ are changed more compared to the initial matrices $(W_\mu(n))$. This behaviour can be seen in fig. 6.1: not only has the $\epsilon = 0.1$ simulation not yet reached the equilibrium distribution, but the $\epsilon = 0.24$ simulation has a smaller error compared to the $\epsilon = 0.4$ line, i.e. $\langle \mathcal{S}_\square(\epsilon = 0.4) \rangle = 0.501 \pm 0.006$ and $\langle \mathcal{S}_\square(\epsilon = 0.24) \rangle = 0.502 \pm 0.004$. Note that for these expectation values we have only taken the configurations after 200 updates into account.

From fig. 6.2 we observe that the lattice with the heat bath algorithm reached the thermal equilibrium much faster than the Metropolis method. For convenience we introduce a new value in our analysis, N_{therm}, to denote when the lattice has thermalized, and we start measuring the expectation value of an observable by use of eq. (6.3). For the Metropolis algorithm we find $N_{\text{therm}} \sim 200$, while for the heat bath we find $N_{\text{therm}} \sim 50$. Moreover, with the chosen settings an iteration of the Metropolis algorithm took around 9 seconds while in the heat bath it only took around 6 seconds. We therefore conclude that the heat bath algorithm is significantly more efficient. This result is relevant because the computation time of Monte Carlo algorithms raises significantly for more advanced lattice settings and/or larger configurations.

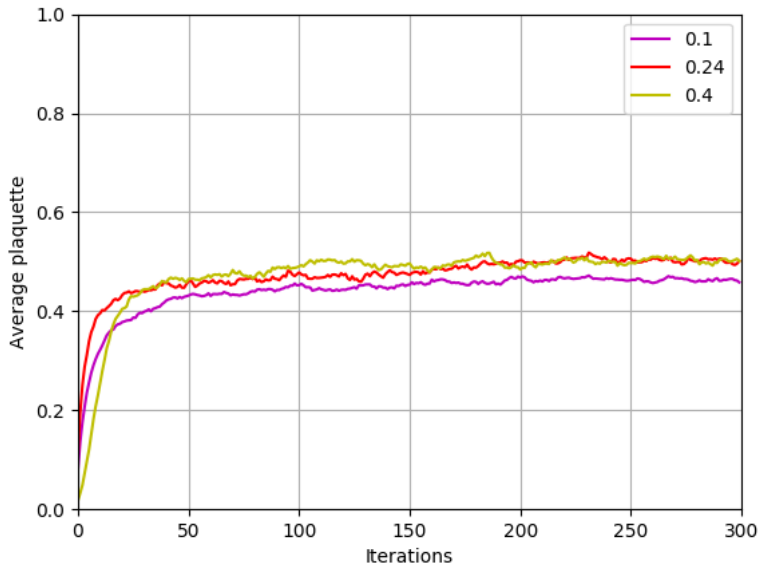

Figure 6.1: Average plaquette as a function of updated lattices. The Metropolis algorithm with ϵ =0.1, 0.24, 0.4 values is shown.

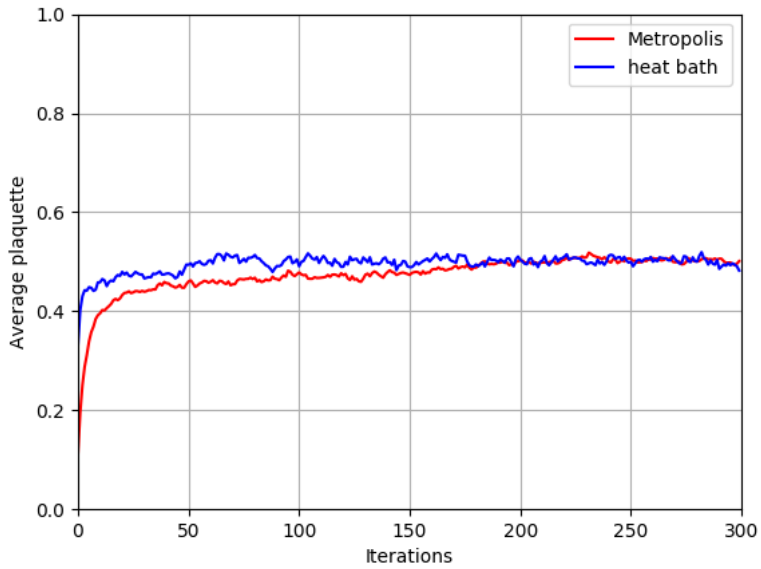

Figure 6.2: Average plaquette as a function of updated lattices. Results for both the Metropolis and heat bath algorithm are shown.

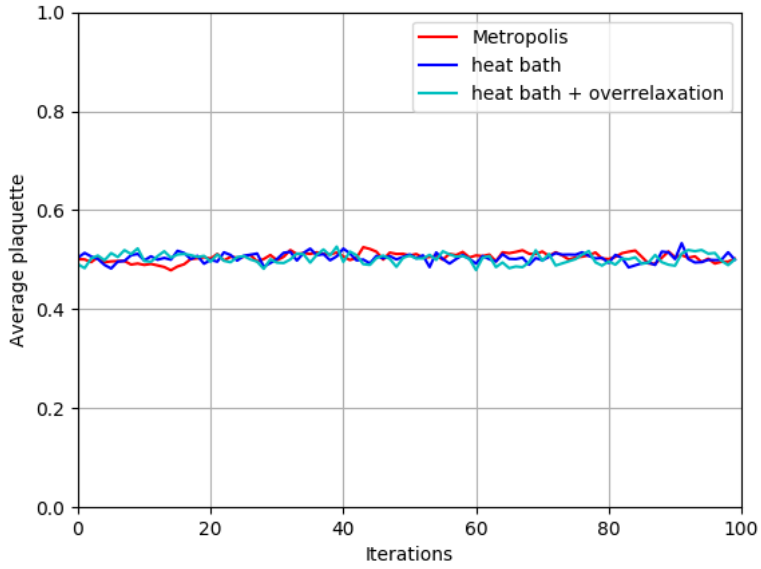

Figure 6.3: Average plaquette for the Metropolis, heat bath, and heat bath with the over-relaxation algorithm as a function of updated lattices. Plotted after 300 iterations (N_{therm}), with 10 updates between every iteration (N_{cor}) in order to calculate the expectation value of the average plaquette.

To measure the expectation value of the average plaquette, we have taken $N_{\text{cf}} = 100$, $N_{\text{cor}} = 10$, and $N_{\text{therm}} = 300$. We have taken the same lattice settings as in the previous computations. For all three algorithms: Metropolis, heat bath and heat bath plus overrelaxation, we show the average plaquette as a function of iterations in fig. 6.3, and found that all of these algorithms give equivalent results for the expectation value. $\langle \mathcal{S}_{\square} \rangle$ was measured to be 0.505 ± 0.009, 0.504 ± 0.009, and 0.502 ± 0.010 respectively. This is in agreement with G.P. Lepage [5] and therefore supporting that the simulation is properly working. However, note that the expectation values now have slightly larger errors compared to the Metropolis computation using $N_{\text{cor}} = 0$. (fig. 6.1). The latter is the result of a Monte Carlo integration with configurations that are too correlated. So, we notice that taking overrelaxation to speed up the motions through configuration space is useful, and it is important to take N_{cor} not too small (and not too large such that we generate enough configurations taking computation time into account). Although the error may slightly rise, this is expected to be the correct error. Moreover, the lattice reaches thermal equilibrium faster using the heat bath with overrelaxation algorithm, as can be observed from fig. 6.4. We therefore decided to use the heat bath with overrelaxation algorithm as our algorithm for larger simulations.

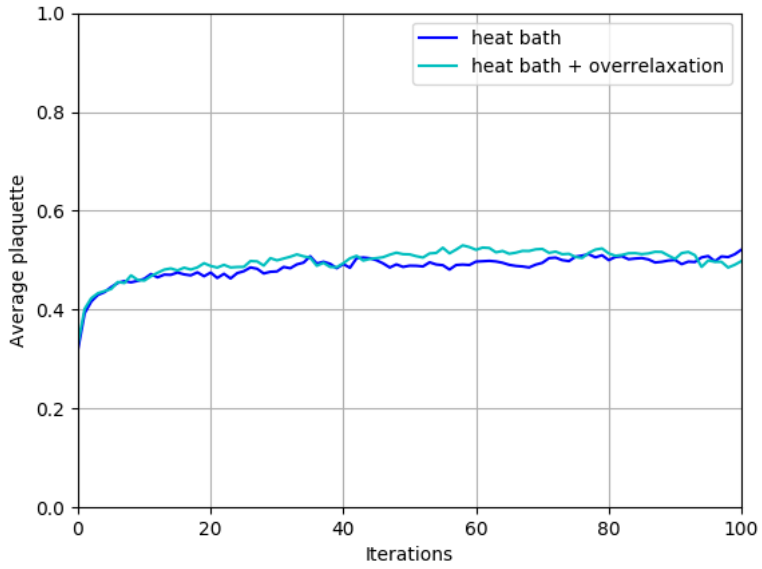

Figure 6.4: Average plaquette as a function of updated lattices. Results for both the heat bath algorithm with and without overrelaxation are shown.

6.1.2 Quantized SU(2) theory: a comparison with Creutz

Although we already have a significant evidence that our lattice implementation performs correctly, we would like to show that it is also in agreement with the results of M.Creutz [22] for the SU(2) theory. In fig. 6.5, we have reproduced one of the figures of his paper, the average plaquette as a function of updated lattices at different values of β_L, using the heat bath method (without overrelaxation) with $N_{\text{cor}} = 0$ and $N_{\text{therm}} = 0$. Note that we have added a red line for $\beta_L = 2.0$, where we used a hot start instead of an ordered cold start to show that the average plaquette converges to the same value as it should. A hot start (a start with random matrices on every link) gives us an average Wilson loop of zero, which results in approaching the plaquette average from above instead of below. If the lattice starts with identity links, we have the usual opposite behavior where the plaquette average is approached from below. The two different starts allow us to better determine when the system has converged, i.e. where the lines meet. For the example in fig. 6.5, this happens at around 13 iterations.

Interestingly, Creutz used even more β_L values to study the behaviour of the Wilson loop average as a function of β_L. He found in the strong-coupling limit

$$W(\square, 1) \underset{\beta_L \to 0}{\sim} \frac{1}{4}\beta_L \tag{6.4}$$

and in the weak-coupling limit:

$$W(\square, 1) \underset{\beta_L \to \infty}{\sim} 1 - \frac{3}{4\beta_L} \tag{6.5}$$

The values in fig. 6.5 agree with these limits. Note that between these limits, the function is smooth and continuous.

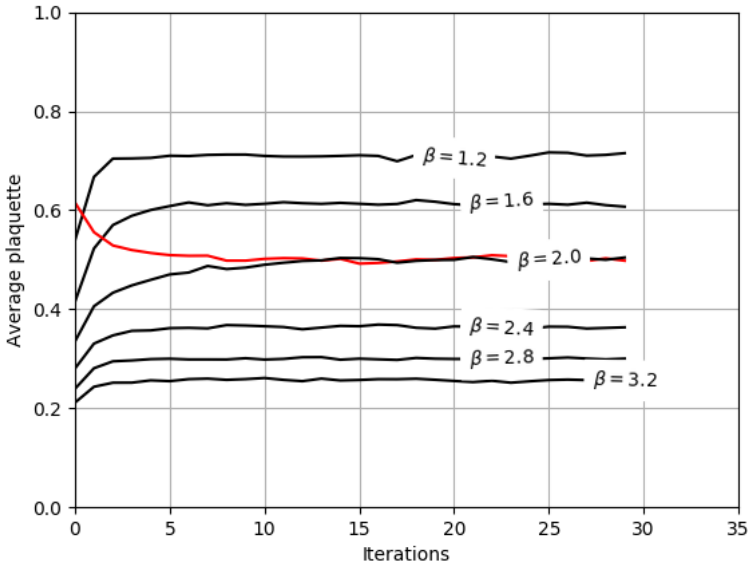

Figure 6.5: The evolution of the average plaquette value at several values of β_L for a 8^4 lattice.

6.1.3 Finite volume effects

The size of the lattice influences the errors of observables and the thermalization. To observe this, the average plaquette as a function of updated lattices with different lattice sizes is shown in fig. 6.6. In these simulations we used the heat bath algorithm with overrelaxation in SU(3) at $\beta_L = 5.5$. We took $N_{\text{cor}} = 0$, $N_{\text{therm}} = 0$ and $N_{\text{cf}} = 300$ for these computations. From fig. 6.6 we conclude two things. First, the error fluctuations decrease as the lattice size increases, known as finite-volume effects. These are infrared effects since they affect the long distance behaviour. Second, for a larger lattice it takes longer to thermalize since there are more links that have to find their equilibrium distribution. Note that we also have ultraviolet effects on the lattice. These fluctuations tend to grow with decreasing β_L (larger coupling), so larger lattice spacing (from section 4.1), as we have a coarser lattice. This effect is shown in fig. 6.5, where there are more short distance fluctuations at smaller β_L.

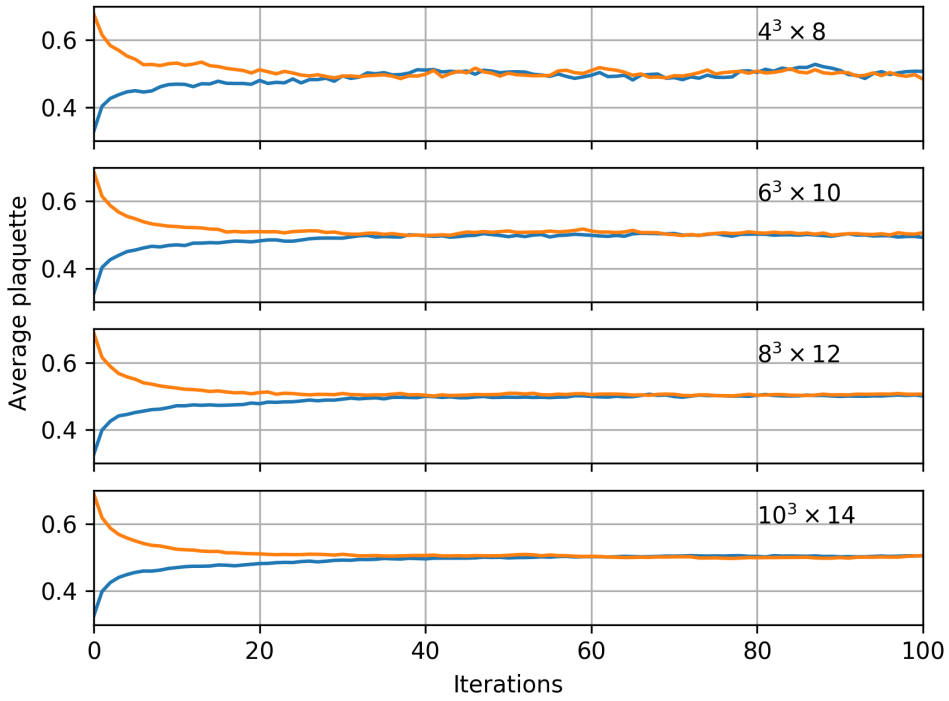

Figure 6.6: Average plaquette as a function of number of updated lattices for different lattice sizes.

To see how the expectation value of average Wilson loops behaves with respect to different lattice sizes, we computed $\langle \overline{W}(\square, a) \rangle$ using $N_{\text{therm}} = 100$ and $N_{\text{cf}} = 200$ on the computations presented in fig. 6.6. Results of this can be seen in fig. 6.7. Again, we see that the larger lattices give rise to smaller errors. Moreover, we observe that some expectation values of average Wilson loops still need to converge on small lattices, meaning that if the loop is large compared to the lattice size it has difficulties to converge to the right value. Note that we have left out computations with errors larger than actual values, such as the average

3×3 Wilson loop on the $2^3 \times 6$ lattice. For this same reason, the expected values of average Wilson 4×4 (or larger) loops are not shown as the finite volume effects completely dominate the signal. In conclusion, fig. 6.7 tells us that if we want to compute expectation values of large Wilson loops we need a large lattice. Larger loops give rise to a smaller Wilson loop expectation value, since we multiply more matrices that are smaller than identity for every loop. Moreover, the expectation values of these observables are more sensitive and need more measurements to accurately determine them.

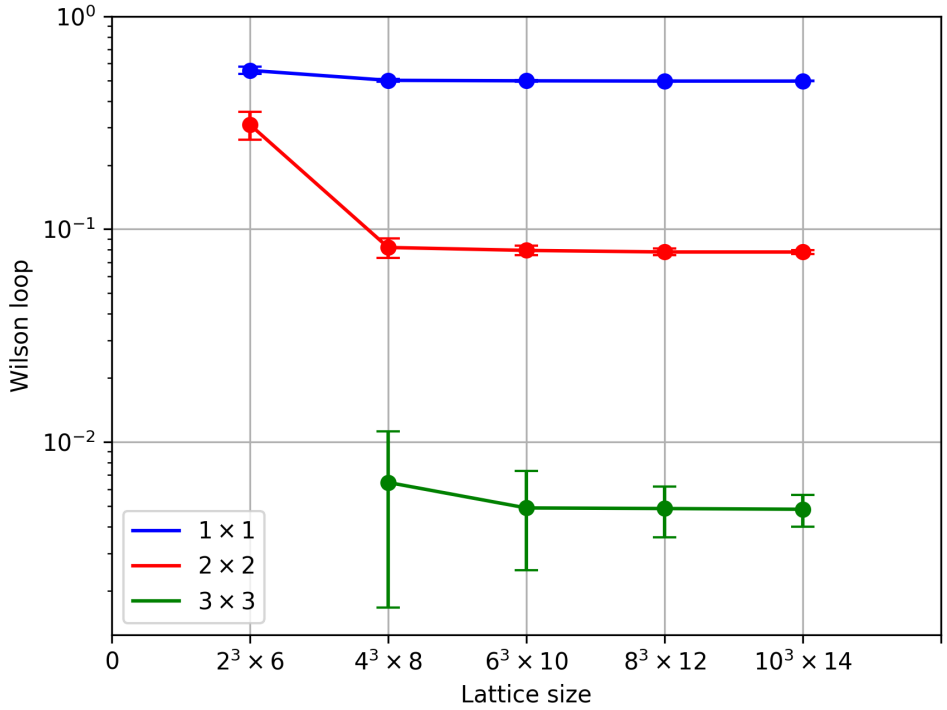

Figure 6.7: Expectation values of average Wilson loops at $\beta_L = 5.5$ as a function of lattice size.

6.1.4 The glueball correlator

Now that we have tested the correct behaviour of our lattice implementation, we calculate the 2-point correlation function on the lattice. We define the autocorrelation function for an observable X at different time slices as

$$C_X(t) = C_X(X_i, X_{i+t}) = \langle (X_i - \langle X_i \rangle)(X_{i+1} - \langle X_{i+1} \rangle) \rangle = \langle X_i X_{i+t} \rangle - \langle X_i \rangle \langle X_{i+t} \rangle \quad (6.6)$$

which is the same as the 2-point connected correlation function from section 2.5. Eq. (6.6) is evaluated by eq. (6.3), where on each lattice configuration the autocorrelation is calculated as the average over all possible correlations of the observable X with different Δt. Since the autocorrelation function is symmetric on the lattice around $T/2$ (the temporal extent), it should have (at large time scales) the following form for the glueball observables

$$C(t) = A\left(e^{-mt} + e^{-m(T-t)}\right) \quad (6.7)$$

where m denotes the mass. In terms of the lattice quantities we write

$$C(t) = A\left(e^{-\hat{m}n_t} + e^{-\hat{m}(N_t - n_t)}\right) \tag{6.8}$$

with $\hat{m}$ the mass in lattice units and $t = an_t$. We want to fit this function to obtain the mass of the particle. Note that we can only use half of the temporal range for a fit.

The autocorrelation of the 0^{++} scalar glueball is shown in fig. 6.8, where $X = \mathrm{Re}\,\mathrm{tr}(O_{xy} + O_{yz} + O_{xz})$, as derived in section 4.4. Note that, for all correlation functions we present, we use the jackknife method for the error estimation as discussed in section 5.7. For this calculation, we used a $10^3 \times 18$ SU(2) lattice with $\beta_L = 2.0$. The computation is done over 2000 lattice configurations, with $N_{\mathrm{cor}} = 15$ and $N_{\mathrm{therm}} = 300$. The red lines with arrows on top indicate that the corresponding dot (average over all lattices) is actually negative and reflected with respect to the x-axis for visualisation. We see that the errors quickly increase at lager temporal sites and stay approximately constant between $n_t = 3$ and $n_t = 15$.

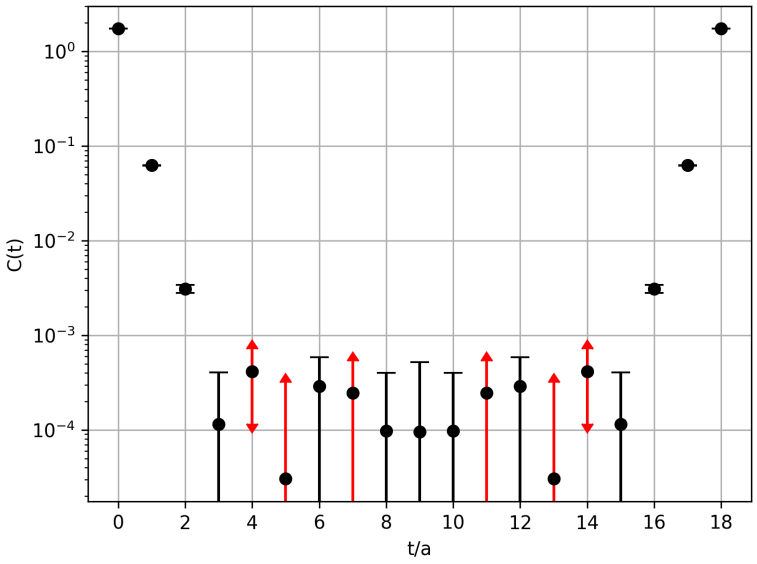

Figure 6.8: 2-point connected correlation function of the 0^{++} glueball as a function of temporal sites in SU(2).

R. Gupta has pointed out [28] that the simple choice of plaquettes suffers from two problems. First, they are much smaller than the glueballs, since we need multiple plaquettes to construct a glueball, and therefore the signal in the autocorrelation is weak. Second, they couple strongly to ultraviolet fluctuations, since the plaquettes are small, increasing the noise in the correlator. For a fixed loop size, both problems will get worse as the lattice spacing is decreased. We can try to resolve these problems by constructing larger observables, by increasing the size of the loops. This can be achieved by taking the linear combination of plaquettes which make op the 0^{++} glueball and increase the length of each of these plaquettes from 4 to for example 8. From fig. 6.7 we conclude that a lattice of size $6^3 \times 10$ or larger

should be sufficient for calculating 2×2 loop averages in SU(3). We expect similar behavior in SU(2) and work with an even larger lattice. Fig. 6.9 shows the autocorrelation of the enlarged observable with loops of size 2×2 (and with the same lattice configurations).

Although the reasoning for using an enlarged observable seems correct, it did not improve the signal. In fact, the signal became slightly worse. This is likely due to the data set being too small for this loop size. In fig. 6.10, we show the same computation of the 0^{++} plaquette correlation, but in SU(3) with $\beta = 5.5$. This computation seems a bit more promising, because we have one additional reliable data point (at $t/a = 3$). However, since we want to perform a fit at larger temporal sites (in the range of $t/a \sim 5/8$), we need to improve our signal regardless. To do so, we need noise reduction algorithms. These are discussed in the next section.

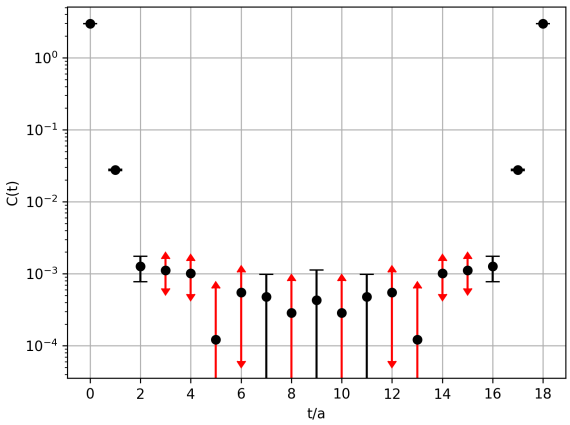

Figure 6.9: 2-point connected correlation function of the 2×2 enlarged 0^{++} glueball as a function of temporal sites in SU(2).

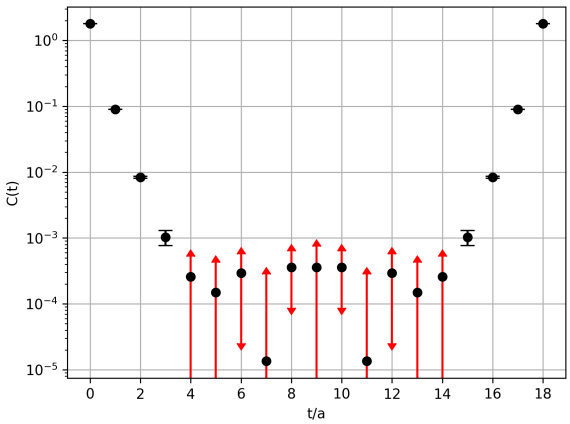

Figure 6.10: 2-point connected correlation function of the 0^{++} glueball as a function of temporal sites in SU(3).

6.2 Noise reduction algorithms

In the previous section, we have seen that the glueball correlator is too noisy to obtain the mass of the glueball from a fit. Therefore, we need noise reduction algorithms to improve the signal. In this section we present two methods to do so: the multihit and multilevel, which we will use together.

6.2.1 Multihit

The multihit technique reduces the fluctuations in the expectation values of loops and was introduced by G. Parisi, R. Petronzio & F. Rapuano [29] to determine the string tension. The idea is as follows: if A is an observable, the statistical errors are controlled by $\langle A^2 \rangle$, and we want to find another variable B, so that:

$$\langle A \rangle = \langle B \rangle \quad \text{but} \quad \langle A^2 \rangle \gg \langle B^2 \rangle \tag{6.9}$$

If we succeed, it is obvious that it is much better to measure B instead of A. If the variable A interacts only with another set of variables C, the statistical expectation of A can be written as $\langle A(C) \rangle$, i.e. the expectation value of A is determined at fixed C. If we now define two mutually independent variables A and A', with nearest neighbour interactions C and C', the distance between these variables should be at least two. We are precisely describing the link A with the staples C. Considering now Wilson loops with links W, we replace links $W(i)$ with the link averages

$$\overline{W}(i) = \frac{\int D[W]\, e^{-S[W]}\, W}{\int D[W]\, e^{-S[W]}} \tag{6.10}$$

as long as the averaged links have no common C, i.e. staple(s) on which the action depends, and we can reduce the error of the observable accordingly. Note that we have to choose carefully on which links we apply the multihit, since the links in loops occasionally have a common C. In plaquette observables we can only replace one link of the loop. Examples of 2×2 and 3×3 loops are shown in fig. 6.11, where, according to H. Meyer-Ortmanns & I. Montvay [30], we can use an average of loop averages which are in different ways multihitted in favour of the expectation value. For the plaquette we use the average over four different multihitted correlations.

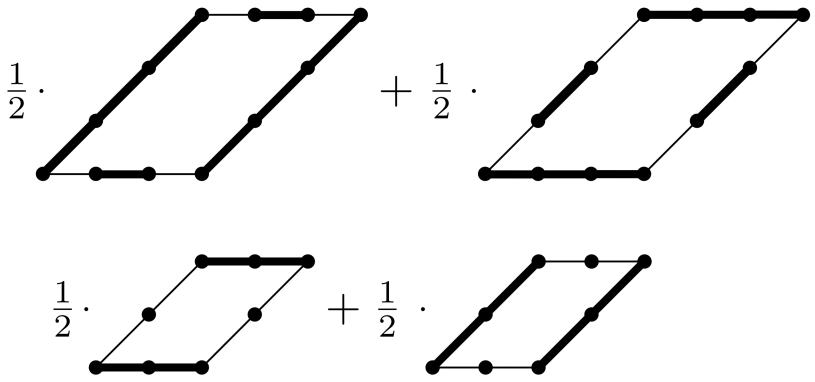

Figure 6.11: Links in 2×2 and 3×3 loops we can apply a multihit to are represented by thick lines.

Although eq. (6.10) can be evaluated numerically using a Monte Carlo algorithm (using an average of N heated hits for every chosen link), this is not practical as the computation time of the correlation will grow very significantly. R. Brower, P. Rossi & C.I. Tan investigated [31] analytic ways to compute integrals of the form eq. (6.10) for SU(N) gauge theories, but they did not find a general convenient expression for numerical SU(N) simulations. In [30] they do, however, present a fully analytic way to compute eq. (6.6) for SU(2) links

$$\overline{W_\mu(n)} = \frac{\int D[W]\; e^{\frac{1}{2}\beta_L \mathrm{Re\ tr}[W_\mu(n)A]}\; W_\mu(n)}{\int D[W]\; e^{\frac{1}{2}\beta_L \mathrm{Re\ tr}[W_\mu(n)A]}} = K \cdot A^{-1} \frac{I_2(\beta_L \cdot K)}{I_1(\beta_L \cdot K)} \quad \text{with} \quad K = \sqrt{|\det(A)|} \tag{6.11}$$

where A is again the sum of the staples, and I_1 and I_2 are the modified Bessel-functions. This can be easily incorporated in our lattice implementation. For larger N the multihit is however difficult to perform. Ph. de Forcrand found [32] a semi-analytic expression to evaluate a SU(3) link average. However, a general semi-analytic way for SU(N) is not mentioned in the literature, and is expected to be very complicated since we obtain already multiple complex contour integrals in the semi-analytic SU(3) case.

6.2.2 Multilevel

The multilevel is used to reduce fluctuations on the correlators themselves (instead of the local single loop observables), and can be used on top of the multihit. M. Lüscher & P. Weisz introduced [33] an algorithm for the Polyakov correlator in lattice gauge theory, and is essentially the same as the multihit method, but is applied to pairs of links instead of single links. This algorithm was first applied to glueball correlators by P. Majumdar, N. Mathur & S. Mondal in [34] and [35]. The idea of the multilevel algorithm is to compute the expectation values in a nested manner. Intermediate values are first constructed by averaging over sublattices with boundaries, after which the full expectation values are obtained by averaging over intermediate values with different boundaries, obtained by updating the full lattice. Incorporating the multilevel algorithm in our lattice implementation requires the introduction of two new parameters: the size of the sublattice in the time direction (as we inspect the correlation of observables at different times), and the number of updates we perform on each sublattice. The multilevel together with the multihit algorithm are illustrated in fig. 6.12.

It should be noted that since for small values of t (where most correlator contributions come from slices within the same sublattice) there can be strong effects (i.e. an increase of the error of the correlator) due to the short temporal extent of the sublattices. Therefore, it might be useful for certain loop observables to compute only correlators between those time-slices which lay in different sublattices.

6.3 The 0^{++} glueball mass

We have used the multihit together with the multilevel algorithm for the SU(2) 0^{++} autocorrelation on the lattice configurations from subsection 6.1.3. We have chosen to evaluate the SU(2) case so that we can use analytic multihit. In fig. 6.13 and 6.14 we show the autocorrelation and fit for the 0^{++} glueball constructed out of plaquettes, and in fig. 6.15 and 6.16 we show the autocorrelation and fit for the 2×2 enlarged 0^{++} glueball. Time did not allow us to use noise reduction algorithms on all these configurations, so the number of configurations (N_{cf}) are presented in the caption of the figures. We sliced every lattice configuration in sublattices of thickness 3 in the temporal direction, and performed 20 sublattice updates for

the 0^{++} glueball correlator. For the 2×2 enlarged 0^{++} glueball correlator, we used only 15 sublattice updates, because 20 updates proved to computationally demanding.

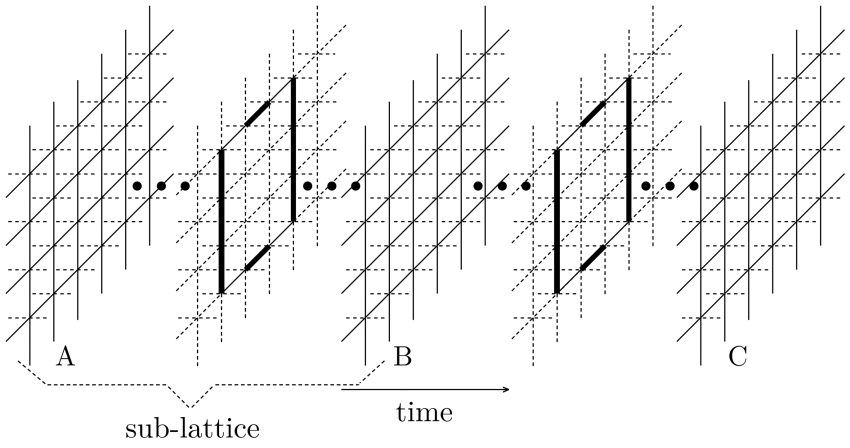

Figure 6.12: Multilevel scheme for computing glueball correlators. The time slices marked A, B and C are held fixed during the sublattice updates. The thick links are the ones that are replaced by their multihit averages.

Indeed, we observe that the multilevel and multihit have reduced the errors at larger temporal times (up to $t/a = 3$). However, we still have not obtained the correct data at large temporal distances that we were hoping for. At such short time scales, where we obtained good data, the excitations of the glueball are expected to dominate the 2-point connected correlation function, as we have discussed in section 2.5. Nevertheless, we conclude that a fit on the obtained data gives us an upper bound of glueball mass in lattice units since the excited energies are always higher than the ground state energy. For the plaquette glueball we found $\hat{m} = 2.66 \pm 0.10$, and for the 2×2 enlarged glueball $\hat{m} = 3.01 \pm 0.15$. In the summary about glueball studies of M.J. Teper [36] we found that there has been a study with the same lattice settings which found the mass of the 0^{++} glueball to be 1.76 ± 0.16 in lattice units. This supports that we have indeed a large contamination of the exited stated in our correlator signal. Note that the correlation function is in both cases slightly decreased at short temporal sites with respect to the computations without multihit and multilevel.

These upper bounds for the masses are in the vicinity of each other, as they should. Note that using the multihit and multilevel on enlarged observables does seem to help the correlation function, since the overall shape in fig. 6.15 seems more promising than fig. 6.13. Moreover, we used less configurations for the enlarged glueball correlator. However, the errors of these data points at relatively large temporal sites are smaller than the data points themselves and below zero. Similarly, in fig. 6.13 we observe that the data points are negative too, some also with a small error. For both observables, this is likely due to the error in the expectation value of the glueball observable ($\langle X \rangle$), dominating the total error of the correlator at these temporal sites. Therefore, besides using more statistics to decrease the errors, we have to very accurately determine the expectation value of the glueball observable so that further error reduction on the correlator is effective.

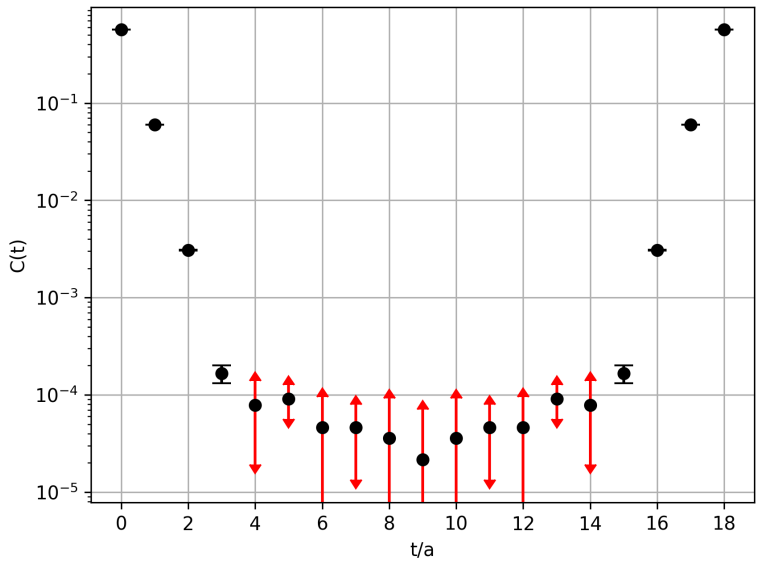

Figure 6.13: 2-point connected correlation function of the 0^{++} glueball as a function of temporal sites with multihit and multilevel noise reduction algorithms ($N_{\text{cf}} = 1500$).

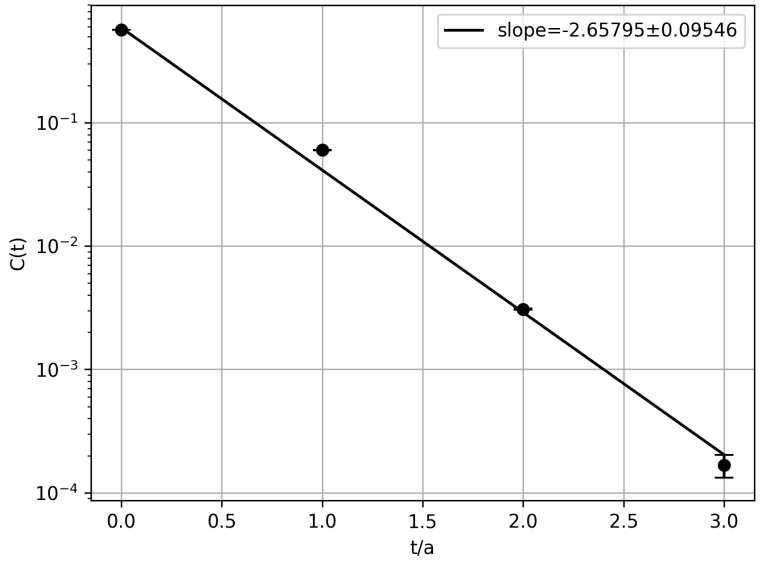

Figure 6.14: Fitted part of the 2-point connected correlation function of fig. 6.13.

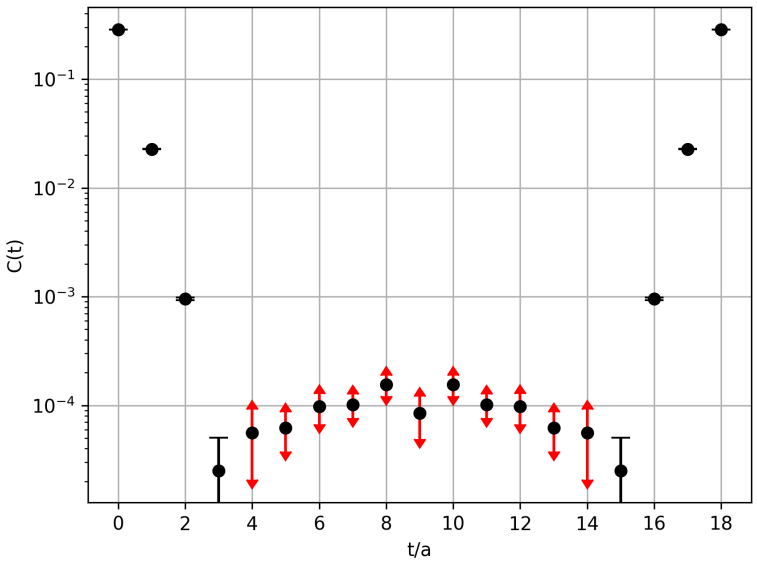

Figure 6.15: 2-point connected correlation function of the 2×2 enlarged 0^{++} glueball as a function of temporal sites with multihit and multilevel noise reduction algorithms ($N_{\text{cf}} = 1000$).

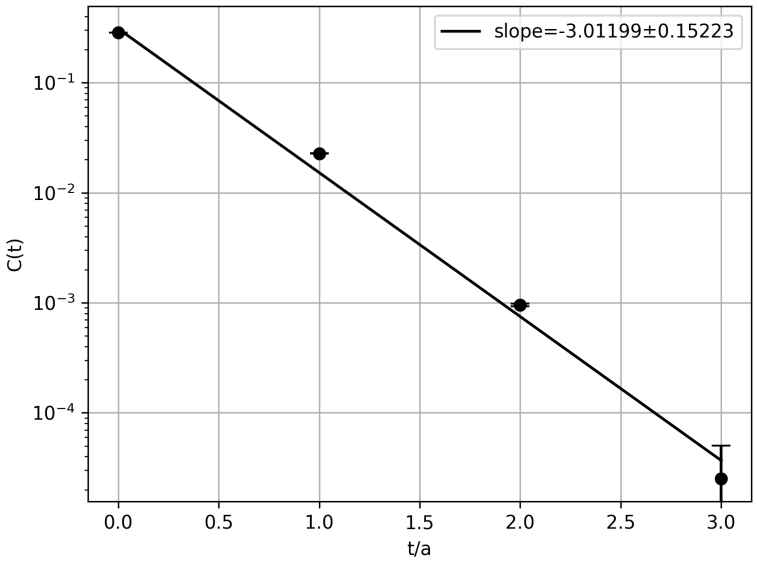

Figure 6.16: Fitted part of the 2-point connected correlation function of fig. 6.15.

6.4 Setting the physical scale

For the SU(2) lattice computation we have measured the Sommer parameter (see section 4.1) to determine the lattice spacing a in a physical unit. We have done this by calculating the expectation values (over all configurations) of average Wilson loops, as in eq. (6.2), but with loops of all kinds of shapes (including non-planar), eq. (2.93), having a spatial extent $\tilde{r}$. Because larger loops require more measurements to obtain a good average expected value (section 6.1.3), we let the lattice implementation make loops only up to $\tilde{r} < 4$. Loops that have a different shape but same $\tilde{r}$ have been averaged over uniformly. Note that every average loop is calculated with different temporal extent ranging from 0 to N_t, in order to determine the exponent at large times. In most cases, the signal of an average loop expectation value with large temporal extent was (like the glueball correlator) dominated by fluctuations. We therefore extrapolated these slopes from relatively small temporal extent ($n_t = 4$) in order to obtain a signal. However, because of this, all data points may be shift to lower (respectively maybe different) values if the computation is done more accurately. We have used a non-linear least square procedure to fit the static quark potential to the data (fig. 6.17), which takes into account the errors of the data points. Note that we only observe the linear rising term of the potential in the data. From the fit we obtained that $a = 0.476$ fm $= 3.842 \cdot 10^{-4}$ MeV^{-1}.

Although the fit to the data has a small error, we should be skeptical whether we have obtained a good fit because we extrapolated slopes of the average Wilson loops. Therefore, we compared the Sommer parameter with data from [36]. Unfortunately, there was no explicit computation of this parameter, but by extrapolating an exponential fit ($r_0/a = 2.45 \cdot 10^{-03} \exp(3.15 \cdot \beta_L)$) to data of $\beta_L = 2.5 - 2.85$ we found that r_0/a should be around 1.33 for $\beta_L = 2.0$. Our fit is not that much off from this expected value, but indeed we need better expectation values of the average Wilson loops with larger temporal extent. Therefore, we have decided to present our results in the previous section in terms of the lattice spacing. Note that the lack of significant data could explain why some values are off from the fit. Moreover, some notable data points may be manifestations of $\mathcal{O}(a^2)$ errors in the Wilson action, breaking the rotational invariance of the action. This can be restored by using an improved action up to higher order in a.

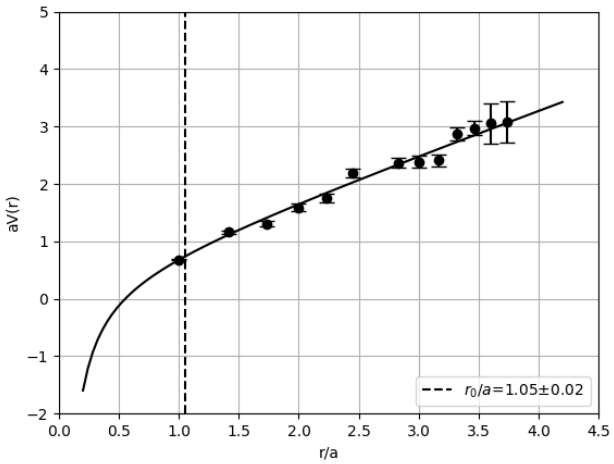

Figure 6.17: Fitted static quark potential as a function of distance r/a in SU(2). The data points are obtained from average Wilson loop expectation values.

7 Conclusions

To evaluate the the large-N glueball spectrum, we have developed a lattice implementation. Unfortunately, we were not able to produce this spectrum with the implementation since we came across some difficulties. Although the implementation seems to perform as it should, we have so far been unable to accurately produce a glueball mass. This is caused by the 2-point connected correlator signal being too noisy, even at relatively small temporal sites. To try and improve the correlator signal at larger time scales in SU(2), we implemented multihit and multilevel noise reduction algorithms. This helped us find the correlation up to three temporal sites, and allowed us to succesfully determine an upper bound for the scalar 0^{++} glueball mass (in lattice units) at $\beta_L = 2$. We have performed this calculation for the glueball observable constructed out of plaquettes and enlarged plaquettes of size 2×2. We have observed that the collelator of the enlarged observable has more potential to find the glueball mass in the future, regarding its shape and the use of less configurations to average over.

7.1 Recommendations

To obtain the desired glueball spectrum, a number of future steps can be taken. First of all, to obtain a pure mass we need to fit the 2-point connected correlator at large temporal sites. To do this, we require a better signal. To improve the signal, the main solutions seem to be a very accurate computation of the glueball observable expectation value, and larger statistics. Concretely, we need more lattice configurations to average the correlation function over and/or more sublattice updates (for the multilevel algorithm). To determine the glueball expectation value with high accuracy, we strongly suggest a separate calculation of $\langle X \rangle$ (similar to the average Wilson loop) by using the multihit algorithm (and if necessary the multilevel algorithm). Thereafter, we can calculate the 2-point connected correlation function of the glueball by subtracting the square of this number to each correlation (i.e. using in eq. (6.6) $\langle X_i \rangle \langle X_{i+t} \rangle = \langle X \rangle^2$), such that the error in the expectation value has a negligible contribution to the error in the correlator at large temporal sites. Since the statistical improvements for the errors in the correlator will increase computational costs significantly, we suggest to also look into ways of improving the speed of the calculations. For example, it may be interesting to parallelize the measurement code in the configurations rather than over the configurations. Another idea would be to rewrite the code in a faster language (such as C++) in order to speed up computations. Yet another idea could be to modify the size of the sublattices, as dividing the lattices in the temporal direction in another way might lead to a better correlator signal. We can also investigate if the use of other enlarged glueball observables yields a better correlator signal.

We could also improve the simulations by using larger observables in the action, together with subtracting tadpole contributions, such that we reduce the error in the lattice configurations. Although the tadpole improvement on large lattices will probably take a lot of time, we expect this to be a promising improvement as many similar studies also use this. Furthermore, we can construct larger observables for in the action by the Symansik's programme, as P. Weiz [37] used it to study loops of length 6. Both improvements can easily be added to the Metropolis algorithm. However, apparently these improvements cannot simply be added to the heat bath algorithm, since in literature the heat bath always seems to be used with the naïve Wilson action. We should investigate why this is the case, and what the options are to include these improvements.

Second, we need to figure out how multihit can be used at larger-N, since this is a crucial step for the slope of the 2-point connected correlation function. A natural next step here would be to incorporate the semi-analytic multihit for SU(3) [32]. For larger N, we could use the fully analytic SU(2) multihit on the SU(2) subgroups of SU(N), although this is not currently supported in literature. Essentially, we should investigate whether there exists a better way to directly evaluate the multihit algorithm for a SU(N) link (since a Monte Carlo method is not an option regarding computation time with the current code).

Third, if we can find a good signal for the correlator and a way to do multihit at larger N, we expect to be able to determine the mass of (for example) the scalar 0++ glueball in the large-N limit. The glueball mass needs to be translated to the continuum theory using for example the Sommer parameter. In this case, we should also increase the static quark potential signal, because the expectation values of Wilson loops with large temporal extend are dominated by fluctuations as well. This could be done by using more configurations to average over and/or using the correlation of Polyakov loops instead, in combination with noise reduction algorithms [33]. Moreover, this will also allow us to use loops with a larger spatial extent, in order to obtain a better fit. Note that working with larger β_L should yield more data on the Coulomb part of the potential, which will also result in a better fit. Besides this, it is a good idea to do multiple lattice computations with different β_L in the large-N limit, to be sure one is extracting a proper scale parameter.

Fourth, we would eventually want to study the entire glueball spectrum, which can be done by constructing different observables on the lattice. However, instead of constructing specific glueball observables for every state, we can also use the variational method which uses the correlation of a set of loop observables, which can then later be projected to the glueball states, as was used by B. Lucini, A. Rago & E. Rinaldi [38]. It is possible that the variational method can help to reduce errors in the correlations for the glueballs as well. In [38] they use blocking and smearing algorithms to reduce noise. Before multihit and multilevel, these algorithms were the standard in gluonic lattice computations. It can be interesting to investigate whether these methods can be combined with the multihit and multilevel algorithms to improve the signal of the correlator.

Finally, we would like to mention that the lattice model of T. Eguchi & H. Kawai [39] would reduce the calculation enormously. They have proven that the original theory of a large-N lattice is equivalent to point model, by carefully choosing appropriate boundary conditions. However, how one can construct glueball observables in such a implementation is unclear, and we have therefore chosen to work with the hypercube as most lattice computations do.

There is still a lot of work to be done on the lattice implementation. Luckily, with the code that has been developed in this project, future students can directly start doing computations and investigate in depth suggested recommendations. In such a way, I firmly believe that the glueball spectrum in the large-N limit will eventually be found. I hope other students will be as interested in this subject as I have been, and are eager to continue this research.

Bibliography

[1] A. Zee. *Quantum Field Theory in a Nutshell.* Princeton University Press, 2010.

[2] M.E. Peskin and D.V. Schroeder. *An Introduction to Quantum Field Theory.* Westview Press, 1995.

[3] K.G. Wilson. Confinement of quarks. *Physical Review*, D 10, 2445, 1974.

[4] M.D. Schwartz. *Quantum Field Theory and the Standard Model.* Cambridge University Press, 2014.

[5] G.P. Lepage. Lattice QCD for Novices, 2005.

[6] C. Gattringer and C.B Lang. *Quantum Chromodynamics on the Lattice.* Springer, 2010.

[7] A.V. Manohar. Large N QCD, 1998.

[8] B. Lucini and M. Panero. SU(N) gauge theories at large N. *Physics Reports*, 526, 93, 2013.

[9] G. 't Hooft. A planar diagram theory for strong interactions. *Nuclear Physics*, B 72, 461, 1973.

[10] E. Witten. Baryons in the $1/N$ expansion. *Nuclear Physics*, B 160, 57, 1979.

[11] S. Okubo. ϕ-meson and unitary symmetry model. *Physics Letters*, 5, 165, 1963.

[12] G. Zweig. An SU(3) model for strong interaction symmetry and its breaking. *CERN Report*, TH-401, 1964.

[13] J. Iizuka. Systematics and phenomenology of meson family. *Progress of Theoretical Physics*, Suppl. 37, 21, 1966.

[14] M. Bochicchio. An asymptotic solution of large-N QCD, for the glueball and meson spectrum and the collinear s-Matrix. *AIP Conference Proceedings*, 1735, 030004, 2016.

[15] M. Tanabashi et al. Particle data group. *Physics Review*, D 98, 030001, 2018.

[16] H.F. Jones. *Groups, Represenatations and Physics.* Taylor & Francis Group, 1998.

[17] B. Berg and A. Billoire. Glueball spectroscopy in 4d SU(3) lattice gauge theory. *Nuclear Physics*, B 221, 109, 1983.

[18] R. Sommer. A new way to set the energy scale in lattice gauge theories and its application to the static force and α_s in SU(2) Yang-Mills theory. *Nuclear Physics*, B 411, 839, 1994.

[19] N.A. Campbell, C. Michael, and P.E.L. Rakow. The String tension from lattice QCD. *Physics Letters*, B 139, 4, 288, 1984.

[20] S.L. Altmann and A.P Cracknell. Lattice harmonics, cubic groups. *Reviews of Modern Physcis*, 37, 19, 1965.

[21] N. Metropolis et al. Equation of state calculations by fast computing machines. *Chemical Physics*, 21, 1087 78, 1953.

[22] M. Creutz. Monte Carlo study of quantized SU(2) gauge theory. *Physics Review*, D 21, 2308 85, 1980.

[23] A.D. Kennedy and B.J. Pedleton. Improved heatbath method for Monte Carlo calculations in lattice gauge theories. *Physics Letters*, B 156, 393 87, 1985.

[24] N. Cabbibo and E. Marinari. A new method for updating SU(N) matrices in computer simulations of gauge theories. *Physics Letters*, B 119, 387 88, 1982.

[25] S.L. Adler. Over-relaxation method for Monte Carlo evaluation of the partition function for multiquadratic actions. *Physics Review*, D 23, 2901, 1981.

[26] F.R. Brown and T.J. Woch. Overrelaxed heat bath and Metropolis algorithms for accelerating pure gauge Monte Carlo calculations. *Physical Review Letters*, 58, 2394, 1987.

[27] P. de Forcrand and O. Jahn. Monte Carlo overrelaxation for SU(N) gauge theories. *QCD and Numerical Analysis*, III, 47, 2005.

[28] R. Gupta, A. Patel, C.F. Baillie, G.W. Kilcup, and S.R. Sharpe. Exploring glueball wave functions on the lattice. *Physical Review*, D 43, 7, 2301, 1991.

[29] G. Parisi, R. Petronzio, and F. Rapuano. A measurement of the string tension near the continuum limit. *Physics Letters*, B 128, 418, 1983.

[30] H. Meyer-Ortmanns and I. Montvay. Monte Carlo study of glueball masses in SU(2). *Physics Letters*, B 145, 251, 1984.

[31] R. Brower, P. Rossi, and C.I. Tan. The external field problem for QCD. *Nuclear Physics*, B 190, 699, 1981.

[32] P. de Forcrand and C. Roiesnel. Refined methods for measuring large-distance correlations. *Physics Letters*, B 151, 77, 1985.

[33] M. Lücher and P. Weisz. Locality and exponential error reduction in numerical gauge theory. *Journal of High Energy Physics*, Vol. 2001, JHEP09, 2001.

[34] P. Majumdar, N. Mathur, and S. Mondal. Light glueball masses using the multilevel algorithm. *The 32th International Symposium on Lattice Field Theory*, 2014.

[35] P. Majumdar, N. Mathur, and S. Mondal. Noise reduction algorithm for glueball correlators. *Physics Letters*, B 736, 415, 2014.

[36] M.J. Teper. Glueball masses and other physical properties of SU(N) gauge theories in D=3+1: a review of lattice results for theorists, 1998.

[37] P. Weisz. Continuum limit improved lattice action for pure Yang-Mills theory. *Nuclear Physics*, B 212, 1, 1983.

[38] B. Lucini, A. Rago, and E. Rinaldi. The glueball spectrum at large N. *The 28th International Symposium on Lattice Field Theory*, 2010.

[39] T Eguchi and H. Kawai. Reduction of dynamical degrees of freedom in the large-N gauge theory. *Physical Review Letters*, 48, 16, 1063, 1982.

[40] C. J. Morningstar and M. Peardon. The glueball spectrum from an anisotropic lattice study. *Physical Review*, D 60, 034509, 1999.

A User manual for the lattice implementation

In this appendix, we explain the basic structure of the code we have made for our study, so that one, with a bit of programming skills, can understand where to find certain parts to do computations and knows what in which files happens for any adjustments one would like to do. The code is written in Python 3.6 for Linux and Mac OS using some standard libraries. It could be that some of these libraries one needs to install, but this can be easily done, and Python tells you when you do not have these. Below, we show an overview of the files in ChromCo, and thereafter, we explain them. In the overview, we have only included parts used in the research.

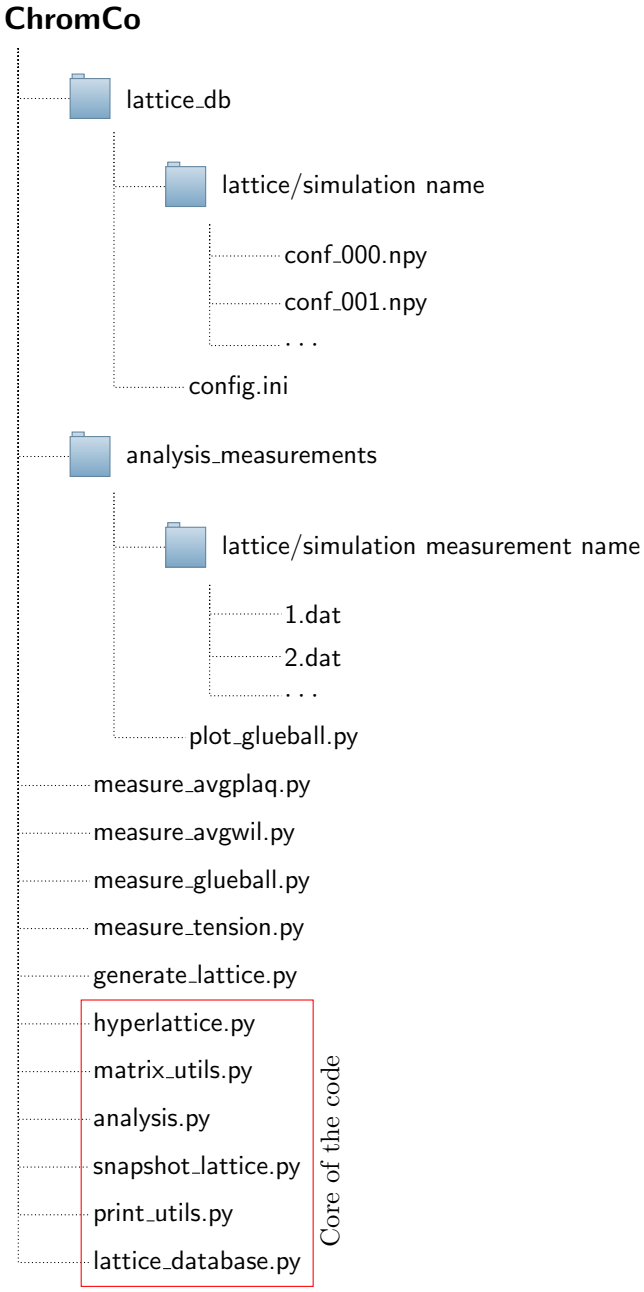

The core of the code:

hyperlattice.py This contains the update algorithms over all the links, i.e. Metropolis and heat bath with or without overrelaxation. It initializes the lattice according to a hot or cold start, calculates the staples, or larger objects for larger loops, in favour of the action, and uses this for the update algorithms. This file contains the 'walker' function, which walks over a set of links, multiplying them, to calculate, for example, the staples or observables of whatever shape and length. It also contains the multihit algorithm for practical purposes. This part of the code uses a parallel updating scheme for the lattice configurations, where each lattice is split optimally over the available cores.

matrix_utils.py Matrix operations are done in this file. It can generate matrices with a ϵ, purely random, or according to a distribution (as for the heat bath). Note that it does this in SU(2) and these matrices are multiplied in an appropriate way in hyperlattice.py to obtain a SU(N) matrix. It also extracts and inserts SU(2) subgroups for SU(N). Furthermore it contains the reunitarization procedure for SU(N) matrices.

analysis.py Here are all measurements performed on the generated configurations. It calculates the average plaquette, average Wilson loops of certain sizes, and the correlation function with or without multilevel and multihit. This part of the code is also parallelized where the lattice configurations are split over the available cores.

snapshot_lattice.py This file controls the lattice configuration files of a simulation.

print_utils.py Makes the print statements for the terminal when generating a lattice. It shows the estimated time of arrival and how long an update took.

lattice_database.py Here the lattice configurations are generated. Together with snapshot_lattice.py there a database of lattice configurations is made. Note that for this file N_{cf} and N_{cor} are of importance.

How to generate lattice configurations:

config.ini First, go to this file and set-up your simulation. An example is shown in fig. 8.1. Note that the dirname is automatically generated after a simulation has finished and is not by hand written here. For clarification, note that if multi = True we use parallel computing, if heatbath= False we use Metropolis, and if cold = False we use a hot start. Default settings can be changed by just redefine the variable for the specific simulation again (as done in the example for overrelaxation).

```
[DEFAULT]
multi = True
heatbath = True
cold = True
overrelax = False

[10x18_su(3)]
r = 10
t = 18
n = 3
beta = 5.5
n_cf = 1000
n_cor = 10
n_therm = 300
overrelax = True
dirname = 10x18_su(3)
```

Figure A.1: Example of config.ini file.

generate_lattice.py Set in this file your lattice name, as for the example:

```
lattice = database.loadFromConfig('10x18_su(3)', True)
```

If the latter statement is False and we uncomment the rest of the script, we can generate pretty straightforward N_{cf} more configurations with the same settings starting from a chosen configuration. This is, for eample, handy if a simulation has finished, and we are not content with the number of configurations. By running this script in the terminal the simulation starts. It will automatically make a map in lattice_db named after your simulation, and puts the lattice configurations (the .npy files) in there. This is shown in the schematic drawing of the code.

How to measure something using the lattice configurations (we are using the glueball correlator measurement as an example):

measure_glueball.py Go to this file and again set the lattice name of the file you want to measure on, similar to generating configurations. In this file, you need to set here the measure options, which are for the glueball correlator: where you want to start measuring (minN_cf) and where you want to end (maxN_cf), a True/False statement for Multihit and Multilevel, and we need to define the glueball observable. The 0^{++} state is there, which is measured using the walker function. If Multilevel is True, we need to set how big the sublattices are (thick_T), the number of updates on each sublattice (subn_cf), and if we want to measure the correlation function only over the sublattices (f.e. only_sub_lat = False). This file will use analysis.py to do the computation. Running this script will generate a map again, but now in analysis_measurements, with your simulation name plus _glueball, where is saves the measurements (the .dat files).

plot_glueball.py This file opens the measurements so that we can plot the glueball correlation function and fit it. For measure_avgplaq and avgwil this procedure is the same, but these plot directly too, since those measurements do not take as long as for the glueball correlator. One also can easily make a plot file to reopen the measurements to make figures to your own taste.